A High Repetition Rate XUV Seeding Source for FLASH2

Dissertation
zur Erlangung des akademischen Grades eines
Dr. rer. nat.

eingereicht beim
Institut für Experimentalphysik
Universität Hamburg

von
Herrn Dipl.-Phys. ARIK WILLNER

Hamburg
Dezember 2011

Erstgutachter: Prof. Dr. Jörg Rossbach
Zweitgutachter: Prof. Dr. Markus Drescher
Drittgutachter: Prof. Dr. Jens Biegert

Dedicated
to
My dear Hazel

Abstract

Improved performance of free-electron laser (FEL) light sources in terms of timing stability, pulse shape and spectral properties of the amplified FEL pulses is of interest in material science, the fields of ultrafast dynamics, biology, chemistry and even special branches in industry. A promising scheme for such an improvement is direct seeding with high harmonic generation (HHG) in a noble gas target. A free-electron laser seeded by an external extreme ultraviolet (XUV) source is planned for FLASH2 at DESY in Hamburg. The requirements for the XUV/soft X-ray source can be summarized as follows: A repetition rate of at least 100 kHz in a 10 Hz burst is needed at variable wavelengths from 10 to 40 nm and pulse energies of several nJ within a single laser harmonic.

This application requires a laser amplifier system with exceptional parameters, mJ-level pulse energy, 10-15 fs pulse duration at 100 kHz (1 MHz) burst repetition rate. A new optical parametric chirped-pulse amplification (OPCPA) system is under development in order to meet these requirements, and very promising results have been achieved in the last three years. In parallel to this development, a new HHG concept is necessary to sustain high average power of the driving laser system and to generate harmonics with high conversion efficiencies. Currently, the highest conversion efficiency with HHG has been demonstrated using gas-filled capillary targets. For our application, only a free-jet target can be used for HHG, in order to overcome damage threshold limitations of HHG target optics at a high repetition rate.

A novel dual-gas multijet gas target has been developed and first experiments show remarkable control of the degree of phase matching forming the basis for improved control of the harmonic photon flux and the XUV pulse characteristics. The basic idea behind the dual-gas concept is the insertion of matching zones in between multiple HHG sources. These matching sections are filled with hydrogen which shows no HHG for intensities $> 3 \cdot 10^{14}$ W/cm^2. The dispersion of the hydrogen plasma leads to a phase advance in the matching zone which can be used to significantly enhance the harmonic yield. An enhancement of up to a factor of 36 has been demonstrated with dual-gas HHG compared with a single jet of the same length. The achieved conversion efficiencies are already competitive with the best efficiency values so far reported. Additionally, efficient control of the two quantum path contributions has been demonstrated leading to a direct coherence control of the source.

This novel XUV source, consisting of a high repetition rate laser system and a dual-gas high harmonic generation target, should lead to sufficient energy and a high degree of coherence control within the seeding process at the FLASH2 FEL.

Zusammenfassung

Verbesserte Leistung der Freie-Elektronen Laser (FEL) Lichtquellen in Bezug auf zeitliche Stabilität, Pulsform und spektralen Eigenschaften des verstärkten FEL Pulses ist in vielen Bereichen der Wissenschaft von Interesse. Eine vielversprechende Methode zur Realisierung dieser Verbesserungen ist das direkte „Seeden“ mit in Edelgasen erzeugten höheren Harmonischen eines Laserstrahls. Ein durch eine externe XUV-Quelle „geseedeter“ Freie-Elektronen Laser ist für FLASH2 bei DESY in Hamburg geplant. Die Anforderungen an die XUV/soft X-ray-Quelle kann wie folgt zusammengefasst werden: Man benötigt eine Wiederholrate von mindestens 100 kHz im 10 Hz-Pulszug kombiniert mit variablen Wellenlängen von 10 bis 40 nm und Pulsenergien von mehreren nJ innerhalb einzelner Harmonischer.
Diese Anwendung erfordert ein Laser-Verstärker-System mit außergewöhnlichen Parametern, mJ-Level Pulsenergie, 10-15 fs Pulsdauer bei 100 kHz (1 MHz geplant) in 10 Hz Burst-Wiederholraten. Ein neues „optical parametric chirped-pulse amplification“ (OPCPA) System ist in der Entwicklung, um diese Anforderungen zu erfüllen, und herausragende Ergebnisse sind in den letzten drei Jahren erreicht worden. Parallel zu dieser Entwicklung ist eine neue „High Harmonic Generation“ Konzeption notwendig, um die hohe mittlere Leistung des antreibenden Lasers zu nutzen und um hohe Konversionseffizienzen und damit ausreichend „Seed“-Energie erhalten zu können. Adequate Effizienzen des „High Harmonic Generation“ Prozesses wurden bisher mit Gas gefüllten Kapillaren erreicht. Für unsere Anwendung ist jedoch nur ein Gastarget mit frei liegenden Jets anwendbar, um die durch die hohen Wiederholraten entstehende hohe Durchschnittsleistung ohne materielle Zerstörschwelle nutzen zu können. Zu diesem Zweck wurde eine neuartige dual-Gas Multijet Quelle entwickelt und erste Versuche zeigen eine bemerkenswerte Kontrolle des Grades der Phasenanpassung, was wiederum die Basis für die absolute Kontrolle über den harmonischen Photonenfluss und der XUV-Puls-Eigenschaften bildet. Den Kern des neuen HHG Konzeptes bilden passive Zonen zwischen mehreren Erzeugungsquellen. Diese Zonen sind mit Wasserstoff gefüllt, der ab Intensitäten von $> 3 \cdot 10^{14}\,\mathrm{W/cm^2}$ keine höheren Harmonischen mehr erzeugt. Der dispersive Effekt des entstehenden Wasserstoff Plasmas führt zu einem Phasenvorschub in den passiven Zonen. Damit kann man die harmonische Ausbeute beachtlich erhöhen. Eine Erhöhung des Signals um einen Faktor von maximal 36, im Vergleich zu einem Einzeljet von gleicher Länge, konnte gezeigt werden und die Konversionseffizienz is bereits vergleichbar zu den besten Werten, die bisher in der Literatur zu finden sind. Zusätzlich können die Beiträge der zwei beitragenden Trajektorien kontrolliert werden. Dies ermöglicht einen direkten Einfluss auf die Kohärenzeigenschaften der Quelle.
Diese neuartige XUV-Quelle, die aus einem hoch repetitiven Lasersystem und einer Dual-Gas Harmonischenquelle besteht, sollte zu genügend Energie und einem hohen Maß an Kohärenz-Kontrolle innerhalb des „Seed“-Prozesses bei FLASH2 führen.

Contents

The thesis is based on following publications:

Refereed Journals

A. Willner, F. Tavella, M. Yeung, T. Dzelzainis, C. Kamperidis, M. Bakarezos, D. Adams, M. Schulz, R. Riedel, M.C. Hoffmann, W. Hu, J. Rossbach, M. Drescher, N.A. Papadogiannis, M. Tatarakis, B. Dromey, and M. Zepf
Coherent control of high harmonic generation via dual-gas multijet arrays.
Phys. Rev. Lett. **107**, 175002 (2011).

A. Willner, F. Tavella, M. Yeung, T. Dzelzainis, C. Kamperidis, M. Bakarezos, D. Adams, M. Schulz, R. Riedel, M.C. Hoffmann, W. Hu, J. Rossbach, M. Drescher, V.S. Yakovlev, N.A. Papadogiannis, M. Tatarakis, B. Dromey and M. Zepf
Efficient Control of Quantum Paths via Dual-Gas High Harmonic Generation.
New J. Phys. **13**, 113001 (2011).

M. Schulz, R. Riedel, **A. Willner**, T. Mans, C. Schnitzler, P. Russbueldt, J. Dolkemeyer, E. Seise, T. Gottschall, S. Hädrich, S. Duesterer, H. Schlarb, J. Feldhaus, J. Limpert, B. Faatz, A. Tünnermann, J. Rossbach, M. Drescher, and F. Tavella
Yb:YAG Innoslab amplifier: efficient high repetition rate subpicosecond pumping system for optical parametric chirped pulse amplification.
Optics Letters **36**, 2456-2458 (2011).

F. Tavella, **A. Willner**, J. Rothhardt, S. Hädrich, E. Seise, S. Düsterer, T. Tschentscher, H. Schlarb, J. Feldhaus, J. Limpert, A. Tünnermann, and J. Rossbach
Fiber-amplifier pumped high average power few-cycle pulse non-collinear OPCPA.
Optics Express **18**, 4689-4694 (2010).

J. Rothhardt, S. Hädrich, E. Seise, M. Krebs, F. Tavella, **A. Willner**, S. Düsterer, H. Schlarb, J. Feldhaus, J. Limpert, J. Rossbach, and A. Tünnermann
High average and peak power few-cycle laser pulses delivered by fiber pumped OPCPA system.
Optics Express **18**, 12719-12726 (2010).

S. Hädrich, J. Rothhardt, M. Krebs, F. Tavella, **A. Willner**, J. Limpert, and A. Tünnermann
High harmonic generation by novel fiber amplifier based sources.
Optics Express **18**, 20242-20250 (2010).

B. Faatz, N. Baboi, V. Ayvazyan, V. Balandin, W. Decking, S. Duesterer, H.-J. Eckoldt, J. Feldhaus, N. Golubeva, K. Honkavaara, M. Koerfer, T. Laarmann, A. Leuschner, L. Lilje, T. Limberg, D. Noelle, F. Obier, A. Petrov, E. Ploenjes, K. Rehlich, H. Schlarb, B. Schmidt, M. Schmitz, S. Schreiber, H. Schulte-Schrepping, J. Spengler, M. Staack, F. Tavella, K. Tiedtke, M. Tischer, R. Treusch, M. Vogt, **A. Willner**, J. Bahrdt, R. Follath, M. Gensch, K. Holldack, A. Meseck, R. Mitzner, M. Drescher, V. Miltchev, J. Rönsch-Schulenburg and J. Rossbach
FLASH II: Perspectives and Challenges.
Nucl. Instr. Meth. Phys. Res. A **635**, S2-S5 (2010).

Conference proceedings

A. Willner, M. Yeung, T. Dzelzainis, C. Kamperidis, M. Bakarezos, D. Adams, V. Yakovlev, F. Tavella, B. Dromey, B. Faatz, N. Papadogiannis, M. Tatarakis, J. Rossbach and M. Zepf
Complete Control of High-Harmonic Generation for High Average Power Applications.
in *Proceedings of CLEO 2011*, Paper M0915, Baltimore (2011).

A. Willner, M. Schulz, R. Riedel, M. Yeung, T. Dzelzainis, C. Kamperidis, M. Bakarezos, D. Adams, V. Yakovlev, J. Rönsch-Schulenburg, B. Dromey, N. Papadogiannis, M. Tatarakis, S. Düsterer, S. Schreiber, B. Faatz, M. Drescher, J. Rossbach, M. Zepf and F. Tavella
A new XUV-source for seeding a FEL at high repetition rates.
in *Proceedings of SPIE Optics + Optoelectronics*, Paper 8075-20, Prague (2011).

A. Willner, F. Tavella, S. Düsterer, B. Faatz, J. Feldhaus, H. Schlarb, S. Schreiber, S. Hädrich, J. Limpert, J. Rothhardt, E. Seise, A. Tünnermann and J. Rossbach
High repetition rate seeding of a free-electron laser at DESY Hamburg.
in *Proceedings of iPAC 2010*, Paper TUPE007, Kyoto (2010).

F. Tavella, **A. Willner**, S. Hädrich, J. Rothhardt, E. Seise, J. Limpert, S. Düsterer, H. Schlarb, J. Feldhaus, J. Rossbach, and A. Tünnermann
96 kHz Fiber-Amplifier-Pumped Few-Cycle Pulse Optical Parametric Chirped Pulse Amplifier System.
in *Proceedings of International Conference on Ultrafast Phenomena*, Paper TuC2OSA (Optical Society of America, 2010).

E. Seise, J. Rothhardt, S. Hädrich, F. Tavella, **A. Willner**, S. Düsterer, T. Tschentscher, H. Schlarb, J. Feldhaus, J. Limpert, J. Rossbach, and A. Tünnermann
High Repetition Rate 5 GW Peak Power Fiber Laser Pumped Few-Cycle OPCPA with CEP Control.
in *Proceedings of CLEO 2010*, Paper CWA3 (Optical Society of America, 2010).

1 Introduction

The fundamental understanding of natural phenomena and its forces forms the ultimate goal of natural sciences. The invention of the first accelerators by Rolf Wideröe in 1928 [1] and E.O. Lawrence in 1931 [2], as well as the development of the first generation light sources using synchrotron light [3] can be seen as a major step towards this general ambition. The intense and brilliant light of accelerator based photon sources can reveal fundamental processes and even sub-atomic structures. With the advancement of accelerator-based light sources, accelerator facilities became a standard tool for investigations at atomic scales and beyond. With the development of free-electron lasers (FELs) in 1971 [4], the generated radiation at accelerator facilities shows almost laser-like characteristics.
A further improvement of the FEL radiation characteristics can be achieved with direct seeding of the FEL process [5]. In contrast to conventional self-amplified spontaneous emission (SASE) FELs the initialization of the process does not rely on spontaneous undulator radiation but on a laser-like external source. This external source imprints its characteristics on the FEL pulses in terms of pulse duration, spectral and spatial shape as well as energy and timing stability. This results in a laser-like character of the FEL radiation, which tremendously extends the range of applications at large-scale photon sources. The realization of such a seeding concept suffered mostly from the lack of an adequate external seed source at the desired wavelengths. In the case of the FEL FLASH in Hamburg, wavelengths of 5-120 nm can be delivered in the SASE operation mode. High power laser systems, however, usually generate pulses with a central wavelength of > 750 nm. Thus, in order to seed an FEL, for example FLASH in Hamburg, the wavelength needs to be converted into ultraviolet (UV)- and extreme ultraviolet (XUV) radiation.
High harmonic generation (HHG) is commonly considered to be the only way to convert infrared driver pulses into XUV. The process of HHG was discovered by A. McPherson et al. in 1987 [6] and first observation of multiple harmonics of a driver laser was reported by X. F. Li et al. in 1989 [7]. Since its discovery, the nonlinear process of HHG has emerged as a widely used concept for tabletop XUV sources for various experimental applications. These sources suffer from a wavelength-dependent low photon flux. FEL seeding using HHG opens the possibility to enhance the photon flux with the FEL as its amplifier. Thus, direct seeding of a FEL merges three main fields: FEL physics, laser development and nonlinear plasma physics.
For the new FEL FLASH2, high repetition rate seeding operating between 10 and 40 nm is planned. Challenging is both the development of a reliable laser amplifier system and the creation of a new HHG scheme. The source needs to adapt to the FEL repetition rate of max. 100 kHz within 10 Hz bursts. It needs to be well controllable in order to ensure a tunability between 10 and 40 nm. In addition, the source needs to deliver pulse energies per wavelength, which exceeds the spontaneous undulator radiation. The resulting demands on the seeding source and their consequences are the main subject of this thesis. It will be shown, that the newly developed laser amplifier scheme has the potential to meet the requirements as a HHG driver. Laser and HHG source performance show promising results which forms the basis for the first steps towards a directly seeded FLASH2 FEL.

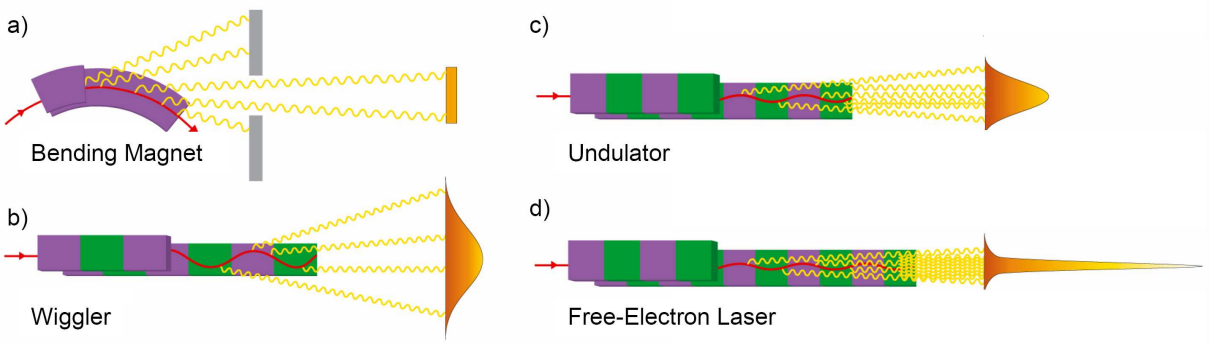

Figure 1: The four generations of accelerator-based light sources. a) The first generation light source is a simple bending magnet in a synchrotron followed by b) the second generation, where an array of bending magnets of alternating polarity (wiggler) is included into a storage ring. c) In the third generation, the wigglers are replaced by undulators, which have a smaller magnet structure period. d) The free-electron laser represents the fourth generation light source with all electrons radiating in phase. Note, that the charged particle beam needs to be relativistic.

1.1 Basic concept of FELs

A single charged particle accelerated by an external force can emit radiation[1]. This is the physical principle behind all accelerator-based light sources. Acceleration in this case means primarily the change of propagation direction, not the increase in the absolute velocity, as the accelerated particles are already at velocities close to the speed of light. Synchrotron radiation was discovered as a disturbing effect responsible for a tremendous energy loss in particle accelerators used as particle colliders for solid-state and particle physics [9]. F. R. Elder et al. discovered the synchrotron radiation with its outstanding characteristics in 1947 [3], which was used by various scientific communities. The radiation was named *synchrotron radiation*, because it was discovered at a synchrotron facility. This type of light source with only bending magnets used as radiators became the *first generation light source* (see Fig. 1a).
In the second generation, the storage ring contains alternating structures of many bending magnets - so-called *wigglers* (Fig. 1b) - which result in an increase of the conversion efficiency. The charged particle (e.g. the electron) follows a sinusoidal trajectory inside the wiggler and light is emitted at any point along the oscillation. This light source has still a large angle of emission. A further increase in intensity has been achieved with the third generation light source which is essentially a wiggler with a very small period of the alternating magnetic structure. This leads to a small angle of emission, enhancing the output of the *undulator* (see also Fig. 1c). The complete trajectory being in the field of view leads to a sinusoidal electric field resulting in a spectrum with only one Fourier component at the resonance wavelength

$$\lambda = \frac{\lambda_u}{2\gamma^2}\left(1+\frac{K^2}{2}+\gamma^2\Theta^2\right), \tag{1}$$

where λ_u is the undulator period, γ the electron energy, Θ the observation angle and

$$K = eB_0\lambda_u/(2\pi m_e c) = 0.934\cdot B_0[T]\cdot\lambda_u[cm]$$

[1]The overview on FEL theory in this paragraph follows basically the explanations given in [8].

the undulator parameter with the peak magnetic field B_0, the electron mass and charge m_e and e, respectively, and the speed of light c. The radiation opening angle is defined as $\Theta_o = K/\gamma$. K therefore defines the shape of the spectrum with a single peak at the wavelength defined by Eq. (1) for $K << 1$. Higher harmonics become visible for $K \approx 1$ due to the distortion of the clear sinusoidal shape of the electric field. Only odd harmonics are visible on the beam axis due to the symmetric trajectory of the electron. For $K >> 1$, the wiggler spectrum increasingly resembles a broad synchrotron radiation spectrum from a bending magnet. However, all of these possible sources, although successful on its own, fall short in terms of increasing the peak power beyond the output of an undulator.

The considerations discussed above are valid for the single-electron approximation. In reality, however, a cloud of up to 10^10 electrons, which is called the *electron bunch*, is introduced by an injector laser. The electrons are fully defined by a six-dimensional phase space distribution including the transversal positions x and y as well as the angles x' and y'. The longitudinal z-position and the energy deviation or *energy spread* $\Delta\gamma$ with respect to a reference particle, following a perfect trajectory through the system, form the last two dimensions. However, electrons within a bunch being relativistic particles do not affect each other to a first approximation. Thus, each electron follows its own trajectory leading to an incoherent superposition of the emitted intra-bunch light beams due to the lack of a defined phase relation. For a coherent emission, the electrons need to be correlated such that they can have a defined relation in phase. Compression of the electron bunch down to a size comparable to the resonance wavelength of the source is impossible, especially in a XUV wavelength regime, due to space charge effects.

The solution for coherent light emission within an undulator was found by John Madey in 1971 [4] with the free-electron laser concept (FEL, see Fig. 1d). A large number of electrons radiates in phase leading to a quadratic signal increase with the number of coherent emitters. The key to this dramatic enhancement is an effect called *micro-bunching*. A seed light wave with the same wavelength as the undulator resonance wavelength is coupled to the electron bunch instead of squeezing the bunch to a few nanometer dimensions. This *seed*-beam can be the spontaneous incoherent undulator radiation produced by the electrons themselves (see paragraph 1.2) or an externally generated beam (see paragraph 1.3). Micro-bunching occurs, because the electric field of the light wave has a much smaller period than the electron trajectory defined by the alternating magnetic structure. Electrons with its position coinciding with the peak of the seeding electric field at any point within the undulator experience an energy transfer to the light wave. Some electrons experiences energy gain overlapping with the tail of the seed field. Electrons loosing energy follow a longer trajectory through the undulator, whereas electrons gaining energy shorten their path. This leads to small-scale density modulations within the electron cloud smaller than the seed wavelength. Hence, coherent emission is possible and each slice of the micro-bunched electrons can be treated as a high charge single particle producing a very strong electro-magnetic field. The modulation depth increases with increasing undulator path. This leads to exponential growth of the radiation power within an undulator until the micro-bunching structure is completely formed. Saturation occurs with maximum electron density modulation and a further increase of the undulator length will not result in a growth of the radiation power (see Fig. 2a; note, that no power increase is expected in the gap between two undulators. With drift spaces of 0.6 m used in the simulation, this explains why the power growth stops for this 0.6 m in the plot before the exponential amplification continues).

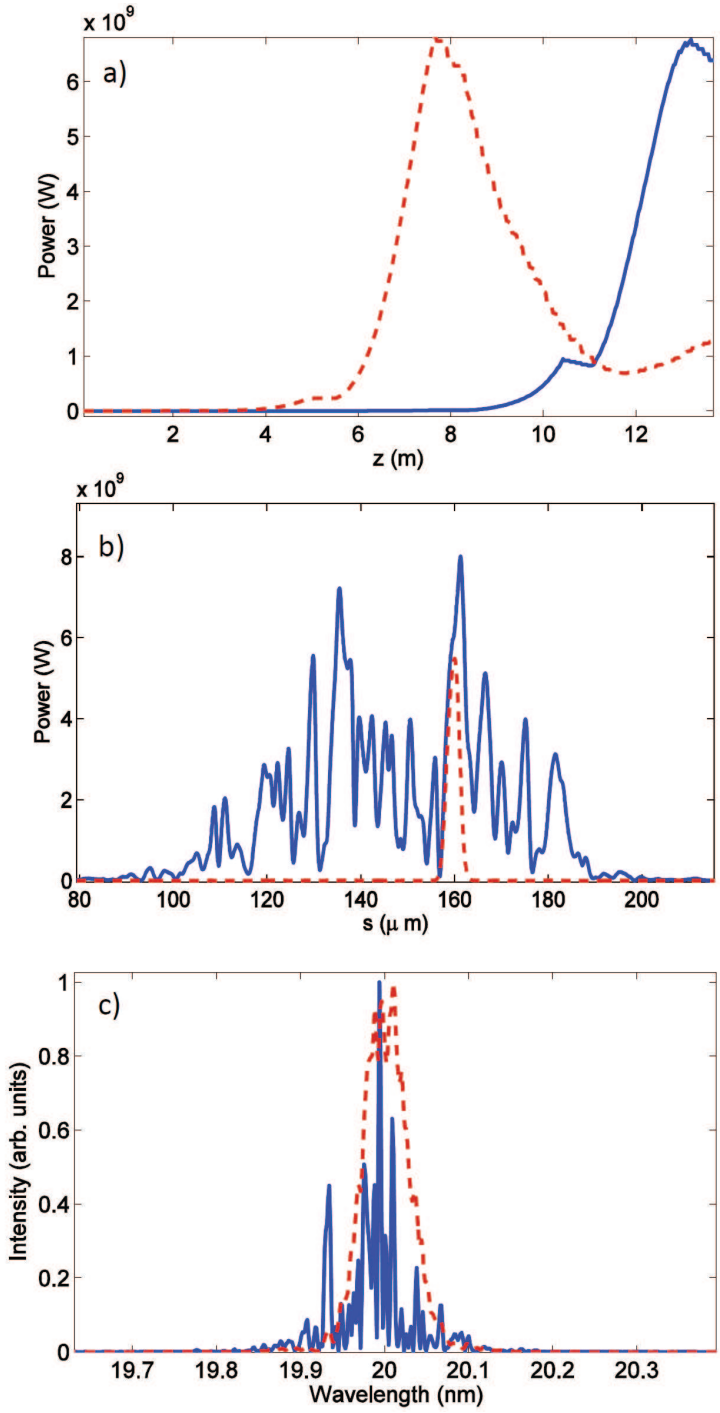

Figure 2: GENESIS simulations for a FEL wavelength of 20 nm. a) Power growth along the undulator section during SASE operation (blue solid) and seeded operation (red dashed) at 20 nm. The undulators have a length of 2 m with a 0.6 m long separating drift space. b) Longitudinal power distribution for SASE (shaded grey) and seeded FEL pulse (solid red). The power distribution is at saturation for either mode. c) FEL spectra for SASE (solid blue) and seeding (dashed red) at 20 nm. The intensity is normalized to the maximum. All simulations are performed assuming a Gaussian electron bunch and seed pulse distribution.

1.2 Self-Amplified Spontaneous Emission (SASE)

Spontaneous light is emitted when electrons pass the undulator. This light can be used for starting the FEL process resulting in the most straight-forward operation mode of a free-electron laser, the self-amplified spontaneous emission (SASE)-mode. The spontaneous radiation produced at the beginning of the undulator is only slightly faster than the relativistic electrons. In addition, the electrons have a reduced longitudinal velocity component due to the undulator oscillations whereas the emitted radiation follows a straight line. Hence, this radiation experiences a slippage relative to the electrons. This slippage increases with increasing number of undulator periods which came to pass by the electrons. In other words, each undulator period adds an additional period within the micro-bunch structure. This results in a smooth growth of FEL power along the undulator as can be seen in Fig. 2a, where a Gaussian-shaped electron bunch was used for a time-dependent GENESIS simulation [10]. For the SASE case, the electrons in the undulator section *seed* their own bunch.
Macroscopically, the energy of the electrons within a bunch is stochastically distributed. This leads to a wide range of electron trajectories in the undulator resulting in a broad, noisy spectrum with the spectral width

$$\frac{\Delta\omega}{\omega} = \frac{\lambda_u}{4\pi L_G\sqrt{3}} \cdot \sqrt{2\ln 2}, \tag{2}$$

where L_G is the power gain length and λ_u the undulator period. The power gain length L_G is the undulator length, in which the FEL power grows by a factor of e. It is the inverse of the exponential growth rate. The start-up of SASE from a stochastic process not only affects the spectral distribution it also results in shot-to-shot fluctuations of the produced radiation in terms of pulse energy and temporal characteristics [11]. The temporal structure of the amplified radiation consists of several uncorrelated modes (see Fig. 2b) and the spectral distribution of the SASE pulses is dominated by many sharp, narrow peaks within the bandwidth of the FEL (see Fig. 2c). The FEL pulses consist of up to several tens of these sub-peaks, depending on the operation conditions. This yields a substantial problem for well-defined investigations of ultrafast dynamics. Even though FEL pulses can in principle be very short (about 10 fs) which would allow to detect ultrafast events, the SASE-based fluctuations will lead to an amplitude and timing jitter. This limits the resolution of pump-probe experiments. However, SASE is well understood and controllable so that it is the basic driving principle of all modern FELs currently in operation.
From the six-dimensional phase space distribution two important parameters can be deduced. The *emittance* is basically the product of the electron beam size and the beam divergence. It defines the transverse phase space distribution[2]. For the longitudinal characterization, there is the energy spread $\Delta\gamma$ as the characteristic parameter, and, additionally, the *peak current* defines the charge per time and thus the number of electrons within a certain bunch section. In order to produce highly brilliant FEL pulses within a short gain length, the electron bunch needs to fulfill three main conditions in the SASE-mode. First, the peak current needs to be high (kA level) in order to achieve a high FEL radiation power within short gain lengths. Second, the energy spread needs to be limited such that the radiation bandwidth does not exceed the FEL bandwidth. Note, that the SASE bandwidth is not a constant along the undulator length. It becomes narrower with increasing number of micro-bunches cooperating in the FEL process.

[2] A more detailed discussion about the beam emittance can be found elsewhere [8] and its determination at FELs is for example discussed in Ref. [12].

Finally, the transverse emittance needs to be small in order to match the transverse phase space size of the generated photon beam along the undulator sections.
For short-wavelength FELs the start-up from spontaneous radiation requires a very long undulator section to reach saturation. For 20 nm, as demonstrated with the simulated example in Fig. 2, the saturation length is 13.2 m, whereas for a FEL in the x-ray regime the undulator section required is larger than 100 m for wavelengths down to 0.1 nm [13].

1.3 External Seeding of a FEL

The stochastically nature of FELs relying on SASE can be reduced by using an external light wave to start the FEL process. A seed beam set at the resonance wavelength of the FEL initiates the modulation instead of the shot noise from spontaneous undulator radiation. The challenge for externally seeded FELs is the lack of adequate laser-based sources delivering sufficient pulse energies in wavelength ranges interesting for FELs and at the optimum repetition rate. In addition, the seeding process suffers from low photon numbers produced by the common conversion process based on high harmonic generation [6].
Complete overlap in the six-dimensional phase space distribution of the photon pulse and the electron bunch needs to be ensured to guarantee maximum energy transfer. As a consequence of external seeding, the FEL undulator length can be reduced as the undulator periods designated to start-up the process with the spontaneous radiation are not needed. As shown in Fig. 2a, saturation already occurs at 7.7 m for a seeded FEL instead of 13.2 m for a SASE FEL. A Gaussian-shaped seed pulse with a pulse energy of 2 nJ and centered at 20 nm was used as input for GENESIS. All electron beam parameters stayed the same as for the SASE simulation. Note, that the final FEL power is not changed with an external seed pulse.
The longitudinal shape of the seed pulse is imprinted into the FEL radiation improving the temporal profile and coherence (see Fig. 2b). A further consequence is that the bandwidth of the resulting radiation is no longer equal to the FEL gain bandwidth (see Eq. (2)). It only depends on the bandwidth of the seed spectrum with the FEL gain bandwidth as its upper limit. Furthermore, in the case of a single-mode seeding spectrum, the FEL spectrum also consists of a single mode in contrast to the multipeak spectrum of SASE radiation. This is an improvement of FEL performance (compare Fig. 2c). The FEL pulses therefore adopt all the coherence properties of the seed light. Assuming a temporally and spatially Gaussian seed pulse in the undulator, the FEL pulse would also be Gaussian in transverse and longitudinal directions as well as in the spectrum.

1.4 Is a FEL a Laser?

A conventional quantum laser amplifier consists of an active medium, an energy pump and a seed beam. The pump radiation excites the active medium by raising the bound electrons within the medium to a higher quantum state or energy level. The electrons fall back into the ground state after relaxation emitting the energy gained by excitation. The emitted radiation overlaps with the seed beam which gets amplified due to the summation of the electric field components. In FELs, however, free electrons act as the active medium and are not bound to any atomic structure. Therefore, a quantum laser could be named *bound-electron laser* as opposed to the *free*-electron laser. The electrons also serve as pump energy within the lasing process transferring their energy to the seed beam. In SASE-FELs, the electrons are even responsible

for the seed radiation, so that the free electrons replace all three driving parts of a conventional quantum laser amplifier.
Due to external seeding, the FEL pulse characteristics are close to conventional laser pulses. Thus, a seeded FEL becomes highly attractive for science but needs an adequate seed source with high repetition rates of current-day FELs. In addition, the seeding source needs to deliver wavelengths down to the XUV regime with energies exceeding the spontaneous radiation which is always present in the undulator sections.

1.5 Thesis Outline

My personal contribution to the seeding project at FLASH2 can be divided into three main parts. The development of a preliminary concept for the seed source implementation at the FEL FLASH2 forms the first part. This includes the actual injection scheme as well as ideas for seeding diagnostics. In particular, a new XUV spectrometer was developed in order to have a direct diagnostic tool for the harmonic radiation. The implementation of the future seed source also requires preliminary simulations for the FEL performance.
The second part is the involvement in the laser amplifier development. In particular, I prepared and performed the proof-of-principle experiments of our fiber pump amplifier system and also contributed to final tests with this amplifier chain at DESY.
The development of a new HHG scheme forms the major part of the personal contribution to the project. Over the last three years, I developed a multijet gas target based on a novel dual-gas HHG scheme and performed three different experiments in order to demonstrate the feasibility of dual-gas HHG. The analysis also includes 3D simulations for theoretically supporting the results.
The thesis covers all three parts of my contribution. It is subdivided in six main chapters. Chapter 2 gives a theoretical overview, which serves as a motivation for all physical processes involved in the laser and HHG source development. In chapter 3, the preliminary concepts of the implementation of the future seed source are presented. In the next chapter, I discuss the development of an optical parametric chirped-pulse amplification (OPCPA) system as driver laser for the seed source. This includes the presentation of the experimental results achieved during preliminary experiments with the fiber pump amplifier. In chapter 5, the special source requirements, the general HHG concept and all experimental results of the three HHG experiments are presented. Finally, I discuss the next steps necessary to complete the seed source development concerning the laser amplifier and the HHG target (chapter 6).

2 Theoretical Background

The development of an external seed source for the FLASH2 FEL incorporates two main topics of physics: laser amplifier development based on the concept of optical parametric chirped-pulse amplification (OPCPA) and the nonlinear process of high harmonic generation (HHG). A theoretical overview of all important topics is given in this chapter starting with an overview on OPCPA and its fundamental theory. The chapter ends with a detailed section about the microscopic and macroscopic description of HHG.

2.1 Optical Parametric Chirped-Pulse Amplification (OPCPA)

Laser pulse amplification via optical parametric amplification (OPA) [14, 15] combined with the powerful tool of chirped-pulse amplification (CPA) [16] is so far the most common way to amplify sub-10 fs pulses at high average powers [17]. In contrast to conventional lasers, where the pump energy is stored before amplification, nonlinear optical amplification is an instantaneous effect. Being a second-order nonlinear process, OPA is a three wave mixing process. It takes place in a nonlinear optical crystal. This paragraph will give an overview on the nonlinear effect of OPA, CPA and combined OPCPA. In addition, a short introduction on mode-locked lasers is given due to the use of these laser systems as a seed source for OPCPA schemes.

2.1.1 The nonlinear Susceptibility

OPA is called *parametric* amplification because of one material-dependent parameter responsible for all nonlinear effects within nonlinear optical media. The basic connection between an electric field **E** and the polarization **P** of the medium is the intensity dependent *susceptibility* χ [18, 19]. With an electric field **E** the susceptibility can be expanded in a Taylor series

$$\chi(\mathbf{E}) = \chi^{(1)} + \chi^{(2)}\mathbf{E} + \chi^{(3)}\mathbf{E}\mathbf{E}..., \tag{3}$$

which leads to a polarization in the form

$$\mathbf{P} = \varepsilon_0 \left(\chi^{(1)}\mathbf{E} + \chi^{(2)}\mathbf{E}\mathbf{E} + \chi^{(3)}\mathbf{E}\mathbf{E}\mathbf{E}... \right), \tag{4}$$

where $\chi^{(1)}$ is called the linear susceptibility, which is the dominant contribution to the polarization at low intensities. With increasing E-field amplitude the parameters $\chi^{(2)}$ and $\chi^{(3)}$ begin to play a role which leads to quadratic and third-order effects, respectively. Nonlinear effects become pronounced at intensities $>10^9$ W/cm^2. Only pulsed lasers of high peak intensities can cause nonlinear optical effects.
Parametric amplification occurs due to the intrinsic effect of frequency mixing within the second-order nonlinear polarization. Let us assume two light waves enter the nonlinear medium with

different wavelengths. The intensities are high enough to observe a quadratic effect such that

$$\begin{aligned}\mathbf{P}^{(2)}(\mathbf{x},t) &= \varepsilon_0\chi^{(2)}\mathbf{E}_1(\mathbf{x},t)\mathbf{E}_2(\mathbf{x},t)\\ &= \varepsilon_0\chi^{(2)}\left(\frac{1}{2}\left(\tilde{\mathbf{E}}(\mathbf{x},\omega_1)e^{i\omega_1 t}+\tilde{\mathbf{E}}(\mathbf{x},\omega_2)e^{i\omega_2 t}+cc\right)\right)^2\\ &= \varepsilon_0\chi^{(2)}\frac{1}{4}(\tilde{\mathbf{E}}(\mathbf{x},\omega_1)^2e^{i2\omega_1 t}+\tilde{\mathbf{E}}(\mathbf{x},\omega_2)^2e^{i2\omega_2 t}\\ &+ 2\tilde{\mathbf{E}}(\mathbf{x},\omega_1)\tilde{\mathbf{E}}(\mathbf{x},\omega_2)e^{i(\omega_1+\omega_2)t}\\ &+ 2\tilde{\mathbf{E}}(\mathbf{x},\omega_1)\tilde{\mathbf{E}}*(\mathbf{x},\omega_2)e^{i(\omega_1-\omega_2)t}\\ &+ \left|\tilde{\mathbf{E}}(\mathbf{x},\omega_1)\right|^2+\left|\tilde{\mathbf{E}}(\mathbf{x},\omega_2)\right|^2+cc).\end{aligned} \tag{5}$$

From this equation it follows that the quadratic term of the nonlinear polarization has frequency components at the sum of both frequencies (sum-frequency generation or SFG)

$$\mathbf{P}^{(2)}(\mathbf{x},\omega_1+\omega_2) = \varepsilon_0\chi^{(2)}\frac{1}{2}\tilde{\mathbf{E}}(\mathbf{x},\omega_1)\tilde{\mathbf{E}}(\mathbf{x},\omega_2)e^{i(\omega_1+\omega_2)t}, \tag{6}$$

at the difference of both frequencies (difference-frequency generation or DFG)

$$\mathbf{P}^{(2)}(\mathbf{x},\omega_1-\omega_2) = \varepsilon_0\chi^{(2)}\frac{1}{2}\tilde{\mathbf{E}}(\mathbf{x},\omega_1)\tilde{\mathbf{E}}^*(\mathbf{x},\omega_2)e^{i(\omega_1-\omega_2)t}, \tag{7}$$

at double the frequency ω_j (with $\mathrm{j}=1,2$, second-harmonic generation or SHG)

$$\mathbf{P}^{(2)}(\mathbf{x},2\omega_j) = \varepsilon_0\chi^{(2)}\frac{1}{4}\tilde{\mathbf{E}}(\mathbf{x},\omega_j)\tilde{\mathbf{E}}(\mathbf{x},\omega_j)e^{i2\omega_j t}, \tag{8}$$

and at zero frequency

$$\mathbf{P}^{(2)}(\mathbf{x},0) = \varepsilon_0\chi^{(2)}\frac{1}{4}\left|\tilde{\mathbf{E}}(\mathbf{x},\omega_1)\right|^2+\left|\tilde{\mathbf{E}}(\mathbf{x},\omega_2)\right|^2. \tag{9}$$

In principle, all frequency components are generated whenever two light waves with the frequencies ω_1 and ω_2 passes through a nonlinear optical crystal. The process is instantaneous without any delay or energy storage in the medium. The generation efficiency is different for different input conditions determined by the degree of *phase matching* within the medium.

2.1.2 Phase Matching and Optical Parametric Amplification (OPA)

Phase matching is the key condition for a frequency preselection from Eq. (5). Parametric amplification is a special case of DFG. The difference to DFG is based on the input conditions [14, 19]. Thus, phase matching is further explained using the example of DFG, albeit similar assumptions are valid for all types of frequency mixing.
In general, the polarization can be seen as the source of any electromagnetic wave leaving the nonlinear medium. The incident electric fields induce a *polarization wave* which needs to couple efficiently to the electromagnetic wave for efficient frequency conversion. Let us assume a plane wave such that the polarization term for DFG from Eq. (7) can be written as

$$\mathbf{P}^{(2)}(\mathbf{x},\omega_3-\omega_1) = \frac{1}{2}\left(\varepsilon_0\chi^{(2)}\tilde{\mathbf{E}}(\omega_3)\tilde{\mathbf{E}}^*(\omega_1)e^{-i[(k_3-k_1)\mathbf{x}-(\omega_3-\omega_1)t]}+cc\right). \tag{10}$$

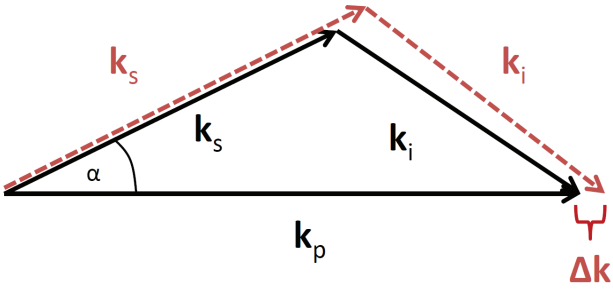

Figure 3: Principle of vector phase matching. $\mathbf{k}_p = \mathbf{k}_s + \mathbf{k}_i$ is valid for best phase matching achieved with a phase matching angle α. With a changed setup (red) and the resulting change in the signal k-vector, the phase matching condition is not fulfilled and thus $\Delta\mathbf{k} \neq 0$.

This is the source term for an electromagnetic wave

$$\mathbf{E}_{\omega_2}(\mathbf{x},t) = \frac{1}{2}\left(\tilde{\mathbf{E}}(\omega_2)e^{-i(\mathbf{k}_2\cdot\mathbf{x}-\omega_2 t)} + cc\right), \tag{11}$$

which obeys energy conservation with

$$\omega_2 = \omega_3 - \omega_1. \tag{12}$$

This condition is intrinsically fulfilled in DFG. A second condition is necessary for efficient generation of the difference frequency. The wave vectors of the generated electro-magnetic waves need to sum to the polarization wave for perfect phase matching. In this case the *momentum conservation condition* is

$$\mathbf{k}_2 \approx \mathbf{k}_3 - \mathbf{k}_1. \tag{13}$$

These two conditions ensure a constant phase relation between the polarization wave and the electromagnetic fields. For SFG, for instance, optimum phase matching is achieved if the *sum* of the two polarization wave vectors equals the electromagnetic wave vector. Note, that for best phase-matched DFG the residual mixing processes are still contributing. However, these frequency components are weak compared to the dominating DFG radiation.
As a special case of DFG, OPA needs a high intensity pump field with frequency ω_p and a weak seed or signal field with frequency $\omega_\mathrm{s} < \omega_\mathrm{p}$. A new field is generated via DFG, the idler field. Its energy relation is $\omega_i = \omega_p - \omega_s$ and the phase matching condition is $\Delta\mathbf{k} = \mathbf{k}_p - \mathbf{k}_s - \mathbf{k}_i$. The idler wave with its frequency $\omega_i < \omega_p$ mixes with the pump field and generates a field with $\omega_s = \omega_p - \omega_i$ which equals the signal frequency. The enhanced signal continues mixing with the pump field as well as the generated idler and this lead to an exponential build up of the signal and idler fields. The related phase $\Delta k \cdot z$ accumulates with increasing interaction length z. The energy flow is in the signal direction at $\Delta\mathbf{k} = 0$. However, when the phase mismatch approaches π this leads to a reversal of the flow of the electro-magnetic energy back to the pump wave. This takes place after a propagation length called the *coherence length*

$$L_c = \frac{\pi}{|\Delta\mathbf{k}|}. \tag{14}$$

Different methods can be applied to achieve phase matching; for example *quasi-phase matching* or *birefringent phase matching*. Quasi-phase matching requires a periodically poled crystal

(e.g. with alternating sign of the optical coefficient). The layer thickness with the same poling needs to be one coherence length to observe an exponential growth. Whenever the energy flow reverses back to the pump wave, the crystal poling will invert the flow direction so that the flow direction is kept the same. Birefringent phase matching, however, uses the effect of birefringent materials in which the refractive index depends on the polarization direction of the electric field. This type of phase matching is also called vector or angular phase matching, because pump and seed beam enter the crystal under a certain angle to achieve best phase matching (see Fig. 3). This phase matching method can be used to phasematch over a broad spectral range. The pump and seed wave polarization are orthogonal to each other and the angle between the geometrical and optical axes of the birefringent crystal serves as an additional degree of freedom.
It should be noted that, similar to the SASE FEL process starting from noise, the OPA can also be started by a spontaneous decay of the pump field into a signal and idler wave under the condition of energy conservation. This spontaneous decay is caused by quantum fluctuations within the gain medium and is called *optical parametric fluorescence (OPF)*. If the parametric amplification starts up from noise, the process is called *optical parametric generation (OPG)*. Likewise in a seeded FEL with spontaneous undulator radiation, the OPF is always present and a high enough seed energy is necessary to achieve a good contrast between the OPA signal and OPF. With an adequate seed energy a reduction of the OPF can be observed as soon as seed and pump pulses overlap in space and time [20].
The non-collinear optical parametric amplification technique is well suited for high average power, few-cycle pulse systems. The gain in an OPA stage can be very high and the thermal load is negligible in the crystal. The OPA process is instantaneous and therefore no energy storage takes place. In addition, as mentioned before, the gain bandwidth can be very large due to phase matching in the non-collinear setup. Hence, short pulses can be amplified with OPA.

2.1.3 Third-order Effects and Mode Locking

The series expansion of the susceptibility in Eq. (3) shows also a third-order component. The effective strength of third-order contributions depends on the material parameter $\chi^{(3)}$. The third-order susceptibility changes the total χ which has a direct impact on the phase velocity within the crystal. Given $n = \sqrt{1+\chi}$, the refractive index becomes intensity (I) dependent and $n(I)$ can be written as

$$n(I) = n_0 + n_2 I = n_0 + \frac{3Z_0}{4n_0^2} I\chi^{(3)}, \tag{15}$$

where Z_0 is the optical impedance and n_0 the linear refractive index. The intensity dependence of the refractive index is known as the *optical Kerr effect*. Most of the crystalline materials have positive n_2 so that the Kerr effect causes *self-focusing* in the transverse plane. The intensity in the beam center is much higher than at the edges when assuming a Gaussian beam. Therefore the refractive index is higher for the inner part than for the outlying area. This effect can be compared to a spherical lens with linear optics, where the beam experiences a larger propagation distance through the medium in the center compared to the outer part of the lens. Thus, for positive n_2 a net focusing effect is the result of the parametric nonlinearity.
Self-phase modulation is the corresponding nonlinear effect in the time domain. The change of instantaneous phase results in a variation of the pulse spectrum during the propagation. The phase shift varying with time causes an instantaneous frequency shift. Additional frequency components are generated.

The Kerr effect is particularly interesting for passive mode-locking laser systems like the titanium:sapphire oscillator. The sapphire not only serves as host medium for the dopant atoms it also serves as the Kerr medium, whereas titanium is responsible for the gain. Without mode locking, the phase relation between the pulses leaving the cavity is random. In this case, the longitudinal modes overlap and interfere such that a weak quasi-continuous beam can be measured as output. By increasing abruptly the peak intensity in the crystal, the Kerr effect causes self-focusing. This can be realized by shortening the cavity for a short moment, for example by reducing the distance of the cavity mirrors. The intensity within the crystal becomes very high due to superposition of several pulses within the medium. As a result of the Kerr effect, the high intensity pulses are favored in the cavity. This can be done by limiting the transverse pump beam size to a diameter equal to the high intensity area generated by the Kerr lens. This method is called *soft aperture Kerr lens mode-locking*.

2.1.4 The powerful Combination of OPA and CPA

The demands on laser systems are continuously increasing. Direct amplification of the laser pulses was still limited after the invention of mode-locked lasers. Pulses with durations in the femtosecond range and high peak powers cannot be directly amplified any further due to two main problems. First, in laser optical material high intensities can cause tremendous damage counteracting stable amplification. In any kind of amplifiers the peak intensity needs to be below the damage threshold. Second, in extreme cases nonlinear effects will modulate the pulse shape transversely (via self-focusing [21]) and the pulse length will be changed due to self-phase modulation [22]. These effects needs to be avoided because the modulations can again lead to severe damage.
The solution is the simple idea of chirped-pulse amplification (CPA, see Fig. 4) which was first used to overcome the power limitations of radars [23]. The technique was applied for the first time within an optical system in 1985 [16] and became a standard tool for current-day laser systems. Within CPA, the pulses are reversibly stretched in order to avoid high peak intensities exceeding the damage threshold of the laser gain medium. This is realized with a stretcher/compressor scheme, where temporal characteristics of the pulse are manipulated. Short pulses have intrinsically a broadband spectrum. By passing a dispersive element like a prism or a diffraction grating, the travel time of different wavelength components through the stretcher setup varies such that the time delay of different spectral parts leads to a long, chirped pulse with the same total energy but lower peak intensity. This manipulated pulse is then amplified in a laser amplifier before it gets compressed in a compressor (e.g. with dispersive elements of opposite sign in comparison with the stretcher). Usually, the pulse cannot be perfectly reconstructed after passing through the complete CPA system. Adaptive dispersion compensation needs to be applied for compensation of higher order dispersion.

The amplification process relies on quantum state excitations in conventional CPA systems. Taking advantage of both the OPA and CPA concepts, an OPA crystal replaces the conventional crystal as an amplification medium. This combined concept is known as *optical parametric chirped-pulse amplification (OPCPA)*. For the first time published in 1992 [24], OPCPA is presently the only known method to amplify short pulses of high peak intensities at high repetition rates. In the OPA process, a quasi-monochromatic powerful pump beam overlaps with the broadband seed pulses in a nonlinear optical crystal. This overlap needs to be ensured in the transverse and longitudinal dimension which requires similar pulse durations for seed and

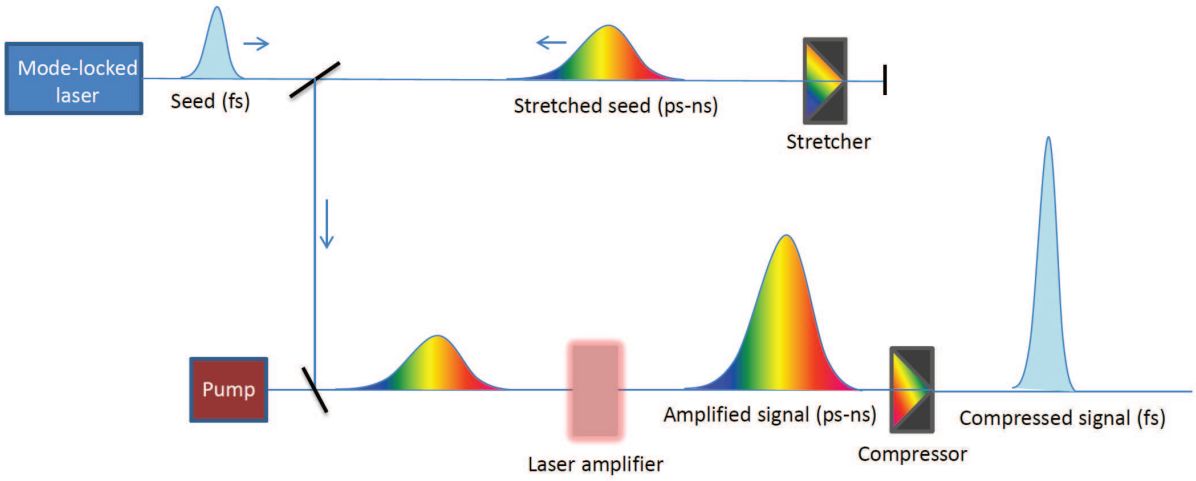

Figure 4: The principle of CPA. A short pulse is stretched so that low peak intensities are guaranteed during amplification. The amplified pulses are finally compressed to its initial length.

pump. Because powerful laser systems are still limited to pulse durations longer than a picosecond, the femtosecond seed pulses from a mode-locked laser need to be stretched in order to meet the temporal gain window of the pump. Due to the relatively short pump pulse duration a non-collinear setup is applied. The angle between pump and seed is an additional degree of freedom for achieving best phase matching for a broad spectrum. The shorter the pump pulse the less stretching is necessary for the seed. However, a shorter pump pulse duration complicates the realization of the time overlap.

2.2 High Harmonic Generation (HHG)

The microscopic process behind HHG can be explained by the three-step model first published by P. Corkum in the year 1993 [25]. This approach is commonly known as the semi-classical treatment of the nonlinear process of HHG [25, 26, 27]. The basic three steps are illustrated in Fig. 5: ionization, acceleration and recombination. When a strong laser field encounters a gas atom, it will bend the atomic Coulomb potential such that a valence electron is able to tunnel through the barrier (see paragraph 2.2.1). This electron with no initial velocity experiences acceleration by the laser field still present until the slope of the electric field changes sign causing the return of the electron to the parent ion. The electron recombines with the parent ion with a certain probability. The recombination yields a photon with an energy higher than the initial driver photon energy due to the accumulation of kinetic energy during the acceleration process. The final photon energy is a combination of the ionization potential I_p and the kinetic energy E_{kin}, which can be expressed in terms of the accumulated quiver- or *pondermotive energy* as the time-averaged kinetic energy of the electron. The pondermotive energy is defined as

$$U_p = \frac{e^2 E_0^2}{4 m_e \omega_c^2} = 9.33 \cdot 10^{-14} \cdot I \left[\frac{\mathrm{W}}{\mathrm{cm}^2}\right] \cdot (\lambda\,[\mu\mathrm{m}])^2\ \mathrm{eV}, \tag{16}$$

where the electron charge and mass are e and m_e, respectively. The laser field amplitude is E_0, the laser intensity I and the central laser frequency and wavelength ω_0 and λ, respectively. The

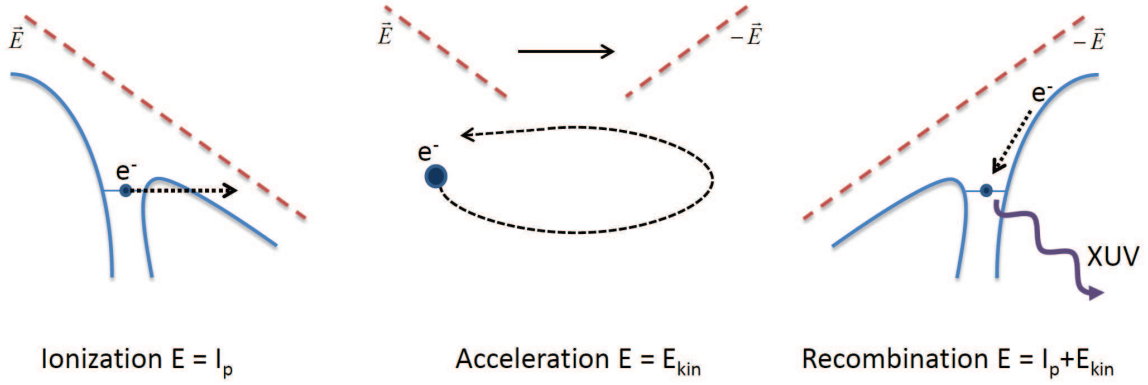

Figure 5: The single-atom response within the three-step model. The electron tunnels through the Coulomb barrier in the presence of a strong electric field. The field accelerates the electron and with the change of sign of the electric field, the electron is guided back to the parent ion. The recombination generates a photon with an energy increased by the kinetic energy gained during acceleration.

maximum photon energy in a single-atom spectrum, which can be achieved with HHG, is

$$\hbar\omega_{max} = I_p + 3.17U_p, \tag{17}$$

also referred to as the *cutoff energy*. This is valid within a semi-classical approximation. A first version of this cutoff law has been found by Krause et al. [28] by solving the time-dependent Schrödinger equation (TDSE) numerically. The prefactor in Eq. (17) can be derived by performing classical calculations (see paragraph 2.2.2) and by a purely quantum-mechanical treatment (see section 2.2.3). In general, a single-atom response spectrum reduces at very low harmonics (the pertubative regime) followed by a plateau of constant amplitude and a cutoff region at a wavelength defined by Eq. (17).
This simple formula describes well the characteristic behaviour of HHG. The first finding is: the higher the ionization potential or binding energy, the shorter the maximum observable wavelength. This implies that, for example, helium with its high ionization potential is well suited for generation of very high harmonics, even towards the water window [29, 30]. Note, that helium with its high ionization energy emits high energy harmonics also at very low ionization levels. However, only weak harmonic yield can be expected due to its small effective nonlinear susceptibility. Second, the cutoff energy grows monotonically with the driver pulse wavelength. Thus, pulses with longer wavelength can be used to extend the cutoff towards higher energies [31, 32]. The conversion efficiency, however, scales with $\propto \lambda^{-5.5}$. Shorter wavelengths lead to a higher harmonic yield compared to longer driver wavelengths. This can be understood, because the driving electric field defines the path of the electron through the continuum, as will be discussed in more detail in section 2.2.2. The longer the wavelength the longer the time for the electron to return to its parent ion. This leads to a spreading of the electron wave packet resulting in a lower recombination probability [33]. Finally, a high intensity is required to extend the cutoff even further. Increasing the intensity will not only lead to higher ionization rates, it will also increase the pondermotive energy. However, the intensity cannot be increased beyond certain values resulting in complete depletion of the ground state, because in that case no tunnel current remains. The tunnel current drives the HHG process.
The three fundamental steps of the HHG process are described in more detail in the following

paragraphs in order to correctly interpret the dependence of high harmonic generation on scaling parameters. After the microscopic treatment of the HHG process it is important to consider the macroscopic gas volume and its effect on the generation of higher harmonics.

2.2.1 Ionization

The first step of the three-step model starts with the superposition of an electric driver field with an atomic potential. The Coulomb potential becomes strongly deformed, if the field strength is comparable to the inner-atomic electric field. Heavily reshaped, the Coulomb barrier is reduced and the electron can tunnel through the potential wall. This ionization effect is called *tunnel ionization* and is a purely quantum-mechanical process. Another effect leading to below-threshold ionization relies on the summation of several photons to fill the gap between the ionization potential and single photon energy. The *multiphoton ionization* and the tunneling are no simultaneous effects. L. V. Keldysh derived a criterion in 1965 to describe the case in which one or the other effect is dominant [34]. He defined a dimensionless *Keldysh parameter*

$$\gamma = \sqrt{\frac{I_p}{2U_p}}. \tag{18}$$

For $\gamma >> 1$ ionization can be described pertubatively in the regime of multiphoton ionization, whereas for $\gamma << 1$ tunneling is dominant. Thus, tunnel and multiphoton ionization depends on the driver intensity. Tunneling becomes dominant for $\gamma \leq 1/2$ at intensities from $\mathrm{I} = 10^{14}\,\mathrm{W/cm^2}$ to $> 10^{15}\,\mathrm{W/cm^2}$ for neutral atoms and a near infrared spectral range of the driver [35]. These intensities correspond to the commonly used intensity range in HHG experiments so that tunnel ionization can be considered as the main ionization effect occurring in HHG.
The process of tunnel ionization can be described by a theory first derived for the case of hydrogen by A. M. Perelomov et al. [36] and later generalized to arbitrary atoms by Ammosov, Delone and Krainov [37] and hence named *ADK theory*.
Instantaneous ionization rates can be analytically calculated, averaging the rate in a constant field over one laser period. This approximation is called *quasi-static* or *low-frequency approximation*, because the oscillation of the electric field is much slower than the tunneling time. The expression for the probability of optical tunnel ionization per unit time from an atomic energy level E, with orbital quantum number l and magnetic spin m is given by [37]

$$W(t) = \left|C_{n^*,l^*}\right|^2 \cdot \left(\frac{3E_0}{\pi F}\right)^{1/2} \left(\frac{2F}{E_0}\right)^{2n^*} \left(\frac{E_0}{2F}\right)^{m+1} f(l,m) \cdot E \cdot \exp\left(-\frac{2F}{3E_0}\right), \tag{19}$$

where the binding energy is E, the field amplitude of the laser pulse E_0 and $F = (2E)^{3/2}$. The atom is considered to be hydrogen-like, with just a single outer electron surrounding an effective core, occupying effective quantum states $n^* = n - \delta_e$ and $l^* = l - \delta_e$. Note, that hydrogen would have integer numbers for n^* and l^*, but the inner electrons only partially shield the inner field so that a *quantum defect* δ_e needs to be accounted for the effective quantum states. The quantum state n is given by $n = Z(2E)^{-1/2}$, where Z is the charge of the resulting ion.

The coefficients $\left|C_{n^*,l^*}\right|^2$ and $f(l,m)$ are defined as

$$f(l,m) = \frac{(2l+1)(l+|m|)!}{2^{|m|}(|m|)!(l-|m|)!}, \tag{20}$$

$$\left|C_{n^*,l^*}\right|^2 = \frac{2^{2n}}{n^*\Gamma(n^*+l^*+1)\Gamma(n^*l^*)}. \tag{21}$$

Note, that $f(l,m)$ contains only integers so that $f(0,0) = 1$ and $f(1,0) = f(1,1) = 3$. The gamma function reduces to $\Gamma(n) = (n-1)!$ for hydrogen. In this case, the expression for $|C_{n^*l^*}|^2$ becomes

$$\left|C_{n,l}\right|^2 = \frac{2^{2n}}{n(n+l)!(n-l-1)!}. \tag{22}$$

The factor $(3E_0/\pi F)^{1/2}$ derives from averaging over one period of the driving electric field, whereas the factor $(2F/E_0)^{2n}$ describes the Coulomb interaction [38, 39]. The remaining factors represent the rate of a short-range potential [36].
The ADK theory is a single-electron theory. Only the outer valence electron in a hydrogen-like state is accounted for tunnel ionization. Thus, the tunnel ionization process described by ADK is a sequential effect. This implies core relaxation before the next ionization step. However, there is a strong dependence on the m quantum number. As the m-states are stochastically occupied, the total time-dependent ionization rate is given by

$$\bar{W}_{ADK} = \left(\sum_{i=0}^{m} W_i(t)\right) / (2l+1). \tag{23}$$

The free electron density can be calculated by solving the rate equation

$$n(t) = n_0 \cdot \left(1 - \exp\left(-\int_{-\infty}^{t} \bar{W}_{ADK}(t')dt'\right)\right), \tag{24}$$

where n_0 is the density of neutral atoms. The ionization fraction of neutral atoms and single ions calculated for a 15 fs pulse (FWHM) with an intensity of $5 \cdot 10^{14}$ W/cm^2 in argon is presented in Fig. 6. The tunnel ionization process causes a reduced number density of neutral atoms and an increase in the number of free electrons as soon as the driving electric field reaches a potential comparable to the Coulomb potential. The step-like increase of the plasma density is due to the internal cycles of the electric field.
ADK is widely used in the HHG community to determine the degree of ionization in the gas medium. The information on the expected level of ionization is crucial for the focusing geometry. It needs to be ensured that no depletion can stop the harmonic process. In addition, experiments for gas density determination with a plasma plume [40] take advantage of this theory for calculating the density of neutral atoms from the measured plasma density.
It should be noted that for decreasing laser pulse durations, approaching the few-cycle regime, a new form of ionization is present. The abrupt increase of the peak electric field leads to a complete suppression of the Coulomb barrier. The electron can pass the barrier without tunneling and ADK does not provide an adequate description anymore. Krainov extended the ADK theory to describe the barrier-suppression regime using the ADK formula (Eq. (19)) as the adiabatic limit for $\gamma << 1$. Interestingly, the Krainov predictions do not vary much from the ADK rates even for pulses as short as 5 fs and for intensities far above the intensity of barrier suppression.

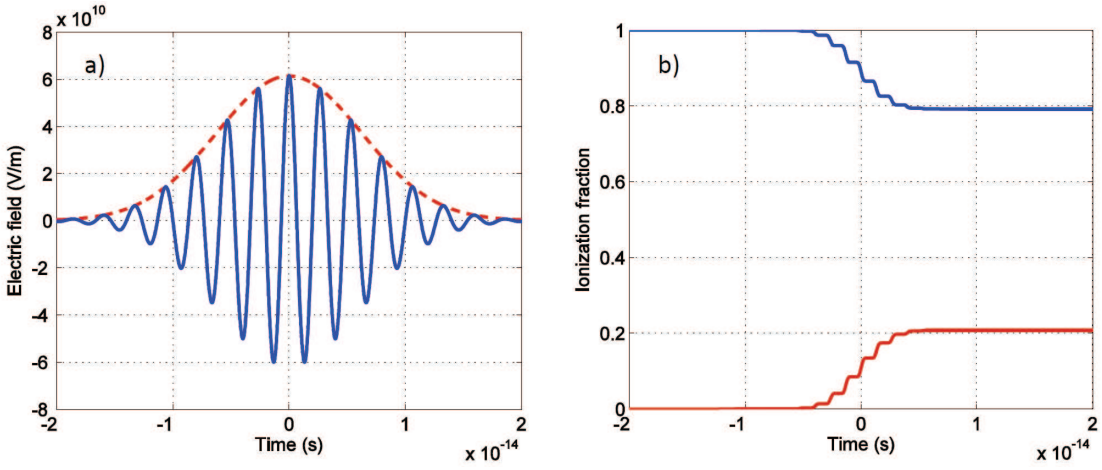

Figure 6: a) Electric field (blue, solid) with field envelope (red, dashed) for a 15 fs (FWHM) laser pulse with a peak intensity of $5 \cdot 10^{14}$ W/cm^2. b) Relative densities for the neutral atoms (blue curve) and free electrons (red curve) in argon.

Even the exact solutions of the time-dependent Schrödinger equation do not deviate more than a factor of 2 [35]. In addition, experimental results show an astonishing agreement between ADK calculations and real measured ionization fractions [41]. Note, that ADK slightly overestimates the ionization fraction for short pulses, so that one can expose the gas to higher intensities than predicted. Nevertheless, ADK is generally acknowledged to be an adequate tool to calculate ionization fractions for HHG and plasma generation in general.

2.2.2 Acceleration

The second step of the semi-classical model for HHG is the electron acceleration by the external light field in the continuum. For the acceleration process a purely classical treatment is sufficient. Therefore, the three step model or semi-classical model combines the quantum effect of tunnel ionization and recombination with the classical concept of acceleration of a charged particle. Let us assume the valence electron is freed via tunneling through the Coulomb barrier and enters the continuum with zero initial velocity. In addition to $v_0 = 0$ the initial position of the freed charge is defined to be also zero, e.g. $x_0 = 0$ [42]. The laser electric field $\mathbf{E}$, responsible for the deformation of the atomic potential, is still present and exerts a classical force on the electron defined as

$$\mathbf{F}(t) = m \cdot \mathbf{a}(t) = e \cdot \mathbf{E}, \tag{25}$$

where the electron mass and charge are m and e, respectively, and the time-dependent acceleration is $\mathbf{a}(t)$. The electric field for an arbitrarily polarized field is defined as

$$\mathbf{E}(t) = E_0 \cos(\omega t)\mathbf{e}_x + \alpha E_0 \sin(\omega t)\mathbf{e}_y, \tag{26}$$

where $0 \leq \alpha \leq 1$ is the parameter defining the degree of circular polarization. From Eq. (25) an expression for the acceleration in a strong field $\mathbf{E}(t)$ can be obtained:

$$\mathbf{a}(t) = \frac{e\mathbf{E}(t)}{m} = \frac{d\mathbf{v}(t)}{dt}. \tag{27}$$

From this expression and with Eq. (26) the velocity of the electron via integration from the ionization time t_i to a time $t > t_i$ can be derived. The resulting velocities are

$$v_x(t) = \int_{t_i}^{t} \frac{e\mathbf{E}(t)}{m} dt = \frac{eE_0}{\omega m} \left(\sin(\omega t) - \sin(\omega t_i)\right) \tag{28}$$

$$v_y(t) = -\alpha \frac{eE_0}{\omega m} \left(\cos(\omega t) - \cos(\omega t_i)\right), \text{where} \tag{29}$$

$$v_x(t_i) = v_y(t_i) = 0. \tag{30}$$

Using these expressions the electron trajectory can be derived. The path is defined as the time-dependent position of the electron. By integrating the velocities the position of the electron can be obtained. It is given by

$$x(t) = \frac{eE_0}{m\omega^2} \cdot \left(\omega(t - t_i)\sin(\omega t_i) - \cos(\omega t) + \cos(\omega t_i)\right) \tag{31}$$

$$y(t) = \alpha \frac{eE_0}{m\omega^2} \cdot \left(\omega(t - t_i)\cos(\omega t_i) - \sin(\omega t) + \sin(\omega t_i)\right). \tag{32}$$

As stated before, the starting position of the electron is $x(t_i) = y(t_i) = 0$ and, clearly, this condition is fulfilled for Eq. (31) and (32). The derived expressions for the electron velocity and spatial position can be used to deduce an expression for the kinetic energy gained by the electron during acceleration. The recombination time t_r can be calculated taking into account the condition that the electron needs to end up at the position of the parent ion to recombine. Thus, with $x(t_r) = 0$ the return time can be determined and therefore the return velocity $v_x(t_r)$ can be calculated with Eq. (28). The kinetic energy becomes

$$E_{kin,x} = \frac{1}{2} m v_x(t_r)^2 = \frac{1}{2} \frac{e^2 E_0^2}{m\omega^2} \left(\sin(\omega t_r) - \sin(\omega t_i)\right)^2 \tag{33}$$

A convenient expression for the kinetic energy in x-direction can be derived by using Eq. (16) for the pondermotive energy, and therefore

$$E_{kin,x} = 2\left(\sin(\omega t_r) - \sin(\omega t_i)\right)^2 \cdot U_p \tag{34}$$

These classical equations of motion can be used to derive first important results for the process of high harmonic generation. Fig. 7a shows trajectories calculated with Eq. (31) and (32). The time-dependent x- and y-position of the electron were plotted (in terms of the optical cycle). Since tunnel ionization is a continuous process, there are two types of quantum paths that any given electron can take during each laser cycle. These two paths are the so called long and short trajectories [26]. The names already reveal the main difference between the two contributions to the harmonic generation process. As can be seen in Fig. 7a, electrons released just past the peak of one cycle of the laser electric field (for example at $t_i = 0.01T$), experience a much longer path through the continuum (long trajectory) than electrons released at ionization times right before the first zero-crossing (short trajectory with for example $t_i = 0.13T$). T is the periodic time of the electric laser field referred to as the optical cycle. The short (long) trajectory travels for $\tau < 0.65\text{T}$ ($\tau > 0.65\text{T}$) in the continuum until returning to the parent ion [43]. At a release time of $t_i = 0.05T$, which corresponds to a driving phase of 18 °, the two trajectories degenerate and have a travel time of exactly $0.65T$, which gives the maximum accumulated kinetic energy possible: $E_{kin,max} \approx 3.17U_p$. Note, that a circular polarized laser field (e.g. $\alpha \neq 0$) cannot be

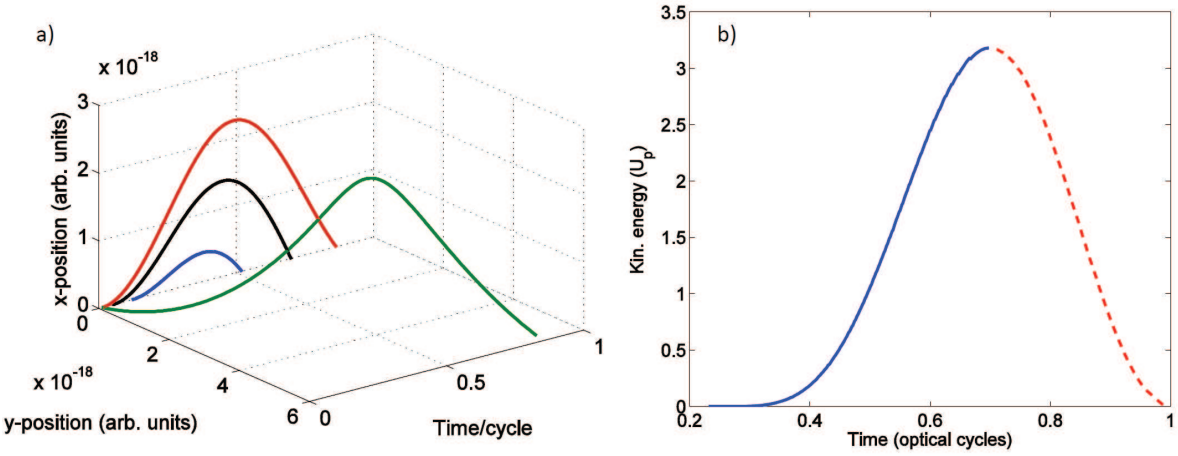

Figure 7: a) Several trajectories of electrons released at different birth times (in terms of the laser optical cycle). In a linear polarized electric field, the electrons can return to the parent ion within a long trajectory (red, solid), short trajectory (blue, solid) or by following the cutoff trajectory (black, solid). Circular polarized light will not result in a recollision (green, solid). b) Kinetic energy in terms of U_p gained by electrons in dependence on the return time t_r. The maximum energy can be gained with the cutoff trajectory at a return time of 0.7T. Short (blue, solid) and long (red, dashed) trajectories have the same energy range $0 \leq E_{kin} \leq 3.18U_p$.

used for HHG, because the trajectory caused by circular polarized light avoids recollision of the electron with the parent ion (Fig. 7a). The gained kinetic energy versus the return time t_r is presented in Fig. 7b. The maximum energy, which can be derived from classical calculations, is $3.18U_p$ with a return time $(t_i + \tau)$ of $0.7T$ corresponding to the cutoff trajectory. The result is similar to the cutoff law in Eq. (17). Short trajectories, the trajectories with a short return time, experience an increased energy gain with increasing return time. After the maximum kinetic energy, the long trajectories gain less energy with increasing return time. However, the energy range $0 \leq E_{kin} \leq 3.18U_p$, which can be gained by the electrons during acceleration, is equal for both long and short trajectory.
Note, that within this single atom picture an increase of the field amplitude does not have any influence on the travel time of the electrons. The reason can be found in Eq. (28) and (31), where both the velocity and the electron position have a linear dependence on the amplitude of the laser electric field.

2.2.3 Recombination

Electrons freed and accelerated by a linear polarized field can, with a certain probability, recombine with the parent ion. This recombination will lead to an atomic relaxation into the ground state causing the emission of a photon with an energy of $E_{harm.} = I_p + E_{kin}$. The maximum harmonic energy is defined by Eq. (17). As a consequence, the kinetic energy defines the degree of up-conversion of the laser frequency and from Fig. 7b it can also be deduced that the harmonic radiation emitted by electrons following either short or long trajectories do have an energy chirp of opposite sign. The short trajectory contributions have a positive whereas the pulses from the long trajectories have a negative chirp. This chirp, also referred to as *atto-chirp*, is a direct result of the pure classical description of the acceleration process and has also

been confirmed by numerical and experimental results [44, 45]. In principle, a chirped pulse can be compressed towards the Fourier limit. However, if one attempts to compress the resulting higher-order harmonics from HHG, only the short trajectory contributions with its positive chirp should be present, which can be achieved via macroscopic control mechanisms as will be discussed in much more detail as one of the main aspects of this thesis. The compression can be performed for example with multilayer XUV mirrors [46] or thin metal films [47]. However, the chirp is not easy to control and the compression scheme could lead to high power losses.
Note, that the contributions of long and short trajectory electrons are equally weighted in the single-atom response. Long trajectory electrons are released just beyond the peak, where ionization rates are very high, so that more electrons are freed via ionization. The short trajectory electrons do have a shorter traveling time through the continuum, which reduces the probability that electrons experiences disturbing forces influencing the path. This therefore increases the recombination probability. In the picture of quantum mechanics, the electron wave packet is more dense for the long trajectory electrons at the birth time, whereas the spread of the electron wave packet of the short electron trajectories are reduced due to a short return time. This results in almost equally weighted contribution.
The classical treatment does not include important quantum effects like diffusion of wave packets which defines the probability of recombination or quantum interference. A purely quantum-mechanical approach has been formulated by Lewenstein et al. [26, 48], also referred to as the *Lewenstein model*. The derived single-atom response within this approach forms the basis for the simulation code used in chapter 5. Lewenstein made four basic assumptions for the derivation of a single-atom dipole moment response:

- The atoms are treated within the *single-active electron (SAE)* or *frozen-core approximation*, which considers atoms to be hydrogen-like.
- The strong-field approximation (SFA) applies and thus $\gamma << 1$.
- The depletion of the ground state can be neglected if the energy is below saturation.
- The electron can be treated as a free charged particle in the continuum subject to an external electric field. The influence of the atomic potential can be neglected.

All equations are in atomic units. The energies are stated in terms of the photon energy. If an atom within the SAE approximation is influenced by an external linear polarized field (arbitrary polarization does not have to be considered, because it is already known that only linear polarization will allow recombination and therefore HHG), the Schrödinger equation can be written as

$$i\frac{\partial}{\partial t}\Psi(\mathbf{x},t) = \left(-\frac{1}{2}\nabla^2 + V(\mathbf{x}) - xE_0\cos(t)\right). \tag{35}$$

The time-dependent wave function can be expanded with the assumptions formulated above:

$$\Psi(\mathbf{x},t) = \exp(iI_p t)\cdot\left(a(t)\,|0\rangle + \int d^3\mathbf{v}\, b(\mathbf{v},t)\,|\mathbf{v}\rangle\right). \tag{36}$$

The ground state amplitude $a(t)$ is about 1 and if the depletion of the ground state is ignored, the amplitudes of the corresponding continuum states $b(\mathbf{v},t)$ is given by

$$\frac{\partial}{\partial t}b(\mathbf{v},t) = -i\left(\frac{\mathbf{v}^2}{2} + I_p\right)b(\mathbf{v},t) - E_0\cos(t)\frac{\partial b(\mathbf{v},t)}{\partial v_x} + iE_0\cos(t)d_x(\mathbf{v}), \tag{37}$$

which is the Schrödinger equation for $b(\mathbf{v},t)$ with the previously made assumptions. The term $d_x(\mathbf{v}) = \langle v|x|0\rangle$ is the single-atom dipole matrix for photoionization along the polarization axis x. $D_x(t) = \langle \Psi(t)|x|\Psi(t)\rangle$ needs to be evaluated in order to calculate the exact expression for the time-dependent dipole moment parallel to the x-axis. With Eq. (36) and the exact solution of Eq. (37), the dipole moment is derived as

$$D_x(t) = \int d^3\mathbf{v} d_x^*(\mathbf{v}) b(\mathbf{v},t) + cc. \tag{38}$$

Note, that the continuum-continuum transitions are neglected in Eq. (38), which implies that only the transitions back to the ground state have been considered. The final expression of the time-dependent dipole moment can be written as

$$\begin{aligned} D_x(t) = i\int_0^t dt' \int d^3\mathbf{p} \\ \cdot E_0 \cos(t') d_x(\mathbf{p}-\mathbf{A}(t')) \times d_x^*(\mathbf{p}-\mathbf{A}(t)) \cdot \exp\left[-iS(\mathbf{p},t,t')\right] + cc, \end{aligned} \tag{39}$$

where a new variable, the canonical momentum $\mathbf{p} = \mathbf{v} + \mathbf{A}(t)$ is introduced with the vector potential $\mathbf{A}(t) = -\int \mathbf{E}(t)dt$. This dipole moment now describes the complete process of HHG in the single-atom picture. From Eq. (39) the three basic steps of the semi-classical picture can be deduced. The first term of Eq. (39) $E_0 \cos(t') d_x(\mathbf{p}-\mathbf{A}(t'))$ is the amplitude of the ionization probability denoted as the transition from the ground state into the continuum at the time t' and with the canonical momentum $\mathbf{p}$. The second term represents the transition back into the ground state (e.g. recombination) at a time t. Between ionization and recombination the wave function is propagated from t' to t, with $\tau_r = t - t'$ being the return time of the electron. During this propagation the wave function acquires a phase factor equal to $\exp[-iS(\mathbf{p},t,t')]$, with the *quasiclassical action*

$$S(\mathbf{p},t,t') = \int_{t'}^t dt'' \left(\frac{1}{2}\left[\mathbf{p} - \mathbf{A}(t'')\right]^2 + I_p \right). \tag{40}$$

Under the assumption that the influence of the atomic potential is small, $S(\mathbf{p},t,t')$ represents the real motion of the electron propagating freely through the continuum exposed to an external laser field with a constant momentum $\mathbf{p}$ ($\mathbf{p}_{t'} = \mathbf{p}_t$ due to momentum conservation). The phase term in Eq. (39) is a unique result of the pure quantum-mechanical approach which cannot be derived from the classical picture.

Eq. (39) needs to be solved in order to derive the exact cutoff of HHG. Solving the four-dimensional integral can be avoided by applying a simplification. The quasiclassical action (see Eq. (40)) varies a lot faster than the other components of the dipole moment $D_x(t)$. This allows the evaluation of the integral over $\mathbf{p}$ only at stationary points and therefore

$$\nabla_{\mathbf{p}} S(\mathbf{p},t,t') = \mathbf{x}(t) - \mathbf{x}(t') = 0. \tag{41}$$

This is a saddle-point equation and thus the method used to evaluate the integral is called the *saddle-point analysis*. Eq. (41) shows, that $\nabla_{\mathbf{p}} S(\mathbf{p},t,t')$ is indeed the difference between the position of the free electron at the time t and at the time t'. Thus, the only trajectories relevant for HHG are the ones leaving the nucleus at a time t' and return at a time t. The time-integral can be solved with the same analysis method. Therefore, with the harmonic number q the

saddle-point equations additionally to Eq. (41) can be obtained:

$$\frac{\partial S(\mathbf{p},t,t')}{\partial t'} = \frac{(\mathbf{p}-\mathbf{A}(t'))^2}{2} + I_p = 0 \tag{42}$$

$$\frac{\partial S(\mathbf{p},t,t')}{\partial t} = \frac{(\mathbf{p}-\mathbf{A}(t))^2}{2} - \frac{(\mathbf{p}-\mathbf{A}(t'))^2}{2} = 2q+1. \tag{43}$$

The second term in Eq. (43) can be substituted with Eq. (42). The last saddle-point equation is just the energy conservation law which gives the final energy of the recombining electron, generating the (2q+1)$^{\text{th}}$harmonic with

$$\frac{\partial S(\mathbf{p},t,t')}{\partial t} = \frac{(\mathbf{p}-\mathbf{A}(t))^2}{2} + I_p = E_{kin} + I_p = 2q+1 \tag{44}$$

The cutoff law is now derived by using Eq. (41) and (42) to express **p** and t in terms of the travel time $\tau_r = t - t'$. These results are then inserted in Eq. (43). Finally, the computation of the energy in dependence of the return time leads to the maximum energy gained by the electron. The cutoff law derived with a quantum-mechanical approach is found to be

$$(2q+1)_{max} = \hbar\omega_{max} = F\left(I_p/U_p\right)\cdot I_p + 3.17U_p \tag{45}$$

In comparison to the classical, phenomenological cutoff law (see Eq. (17)) the prefactor for the kinetic energy is the same. However, the ionization potential is not a stand-alone parameter anymore. For $U_p >> I_p$, $F\left(I_p/U_p\right) = 1.32$ can be obtained, whereas for increasing I_p the prefactor approaches 1. Hence, the quantum-mechanical result differs slightly by being more accurate. The reason for this difference is the natural atomic radius. The electron tunneling through the barrier cannot appear at the origin defined as the center of the atom. Thus, when the electron returns to the ion, it can gain an extra amount of kinetic energy by recombination. This small amount of energy is taken into account by the prefactor. For increasing ionization potentials the additional gain of kinetic energy is reduced due to quantum diffusion.

It is now possible to discuss one limitation of the cutoff extensions in more detail using the quantum-mechanical approach. Eq. (16) and (17) imply that a longer wavelength should be chosen to extend the cutoff to higher energies. However, the electron wave packet experiences spreading during the propagation through the continuum, reducing the recombination probability. The spreading effect increases with longer wavelengths and Schiessl et al. [49] found a λ^{-5} dependence of the conversion efficiency of the process by applying the pure quantum-mechanical approach. Especially for applications like seeding, where the conversion efficiency is one of the main concerns, this is a major limitation.

The phase of the dipole moment in Eq. (39), which is called the *intrinsic* or *atomic phase*, depends on the classical action and therefore on the length of the trajectory or quantum path. For the plateau region two main trajectories play a dominant role [48], as already seen in the classical treatment. In addition, the atomic phase shows a linear dependence on the driver laser intensity [50]. The observable spectrum highly depends on the contribution of the atomic phase which will be discussed in section 2.2.5.

The predicted dipole response and also the cutoff of the harmonic emission are the result of a single-atom treatment. Real experimental observations are always affected by macroscopic effects defining the observable macroscopic conversion efficiency and spectral shape. Due to macroscopic effects, the cutoff can be lower than theoretically predicted so that the single-atom cutoff is always an upper limit in experiments.

2.2.4 Phase Matching

All expressions and formalisms derived in the last sections were related to a single atom and its dipole response which is well described with the three-step model. However, macroscopic effects play a major role in an ensemble of gas particles. Thus, one needs to consider both the single-atom response and the propagation effects of the generation medium for a complete description of the HHG process. For the discussion, a gas jet with an interaction length z between laser beam and generation medium is assumed. The single-atom HHG process can take place every half-cycle of the driving laser field. From Fig. 6a it can be seen that the half-cycles vary in sign but show symmetry in shape. Thus even harmonics vanish in the observed spectrum for isotropic media. This can be explained by considering the components of the nonlinear polarization of the media in the presence of a strong field (compare Eq. (4)). If the electric field changes sign, the polarization can only follow this change if even harmonics disappear. Hence, in an conventional HHG spectrum only odd harmonics are visible.
Harmonic radiation emitted at the beginning of the gas jet experiences a non-vacuum propagation length equal to the medium length L_z. From section 2.2.3 it is known, that the XUV phase at the time of emission is directly defined by the driving laser at the time of recombination. During propagation the photon accumulates other phase components which lead to a derivation from the intrinsic laser phase imprinted as initial phase. If a XUV photon is emitted at a position $0 < z \leq L_z$, its initial phase is also coupled to the laser field. If a phase difference occurs between the XUV radiation started at $z = 0$ and the laser phase at z the two photons will interfere either constructively or destructively. The wave vector for an optical electromagnetic wave passing through a gaseous medium is given by [51]

$$|\mathbf{k}| \approx \frac{2\pi}{\lambda} + \frac{2\pi N_a n(\lambda)}{\lambda} - N_e r_e \lambda - k_g. \tag{46}$$

The first term is the *vacuum term* due to pure propagation through vacuum. The dispersion due to neutral atoms is expressed in the second term (N_a is the density of neutral atoms, $n(\lambda)$ depends on the refractive index of the atoms and λ is the central wavelength of the driver amplifier) and the third term represents the dispersion due to the free electrons (N_e is the plasma density and $r_e = e^2/(4\pi\varepsilon_0 mc^2)$ the classical electron radius). The term k_g depends on the geometry of the system. For geometries where the laser is freely focused into the jet, the Gouy phase shift determines k_g using

$$k_g = \frac{d}{dz} \arctan\left(\frac{z}{z_R}\right) \approx \frac{1}{z_r}, \tag{47}$$

where z_r is the Rayleigh length of the laser beam. It was the appealingly simple idea of Balcou et al. [52] to treat the Gouy phase shift as another contribution to the total k-vector.
Likewise in a nonlinear laser crystal, best phase matching is achieved if the k-vectors of the laser photons and the harmonic photons are identical, which implies for the q$^{\text{th}}$harmonic

$$\Delta k_q = q k_{laser} - k_{XUV} = 0. \tag{48}$$

The total expression for Δk_q using Eq. (46) and (47) is given by

$$\Delta k_q = \frac{2\pi}{\lambda} q(1-\eta)\, p\Delta n - p\eta N r_e \lambda \left(\frac{q^2-1}{q}\right) - \frac{q-1}{z_R}, \tag{49}$$

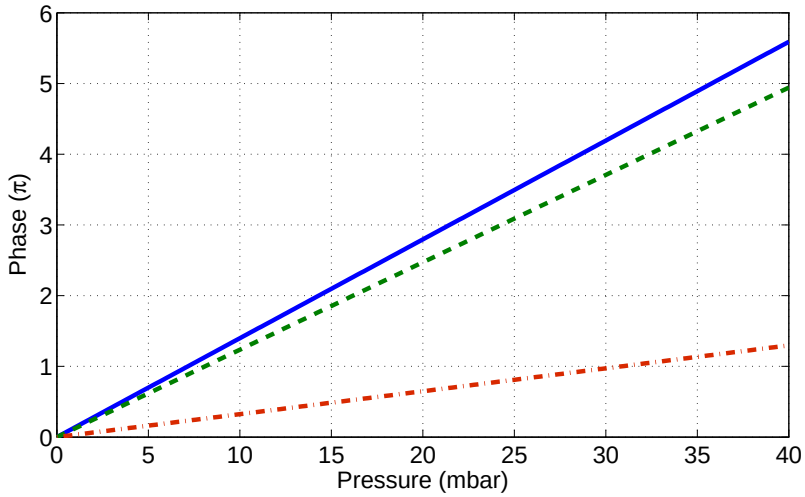

Figure 8: Different phase shifts vs. argon pressure in a 250 μm long jet and an intensity of $1.5 \cdot 10^{15}\,\mathrm{W/cm^2}$ (blue, solid), $7.5 \cdot 10^{14}\,\mathrm{W/cm^2}$ (green, dashed) and $3.5 \cdot 10^{14}\,\mathrm{W/cm^2}$ (red, dotted dashed).

where the gas pressure is p in bar and the ionization fraction η can be calculated with Eq. (24). N is the number density of the gas atoms at atmospheric pressure. The difference between the refractive index corresponding to the driver and the index related to the XUV is given by $\Delta n = n_L - n_{XUV}$. With the difference of the k-vectors defined in Eq. (49), the coherence length $L_c = \pi/|\Delta k|$ can be determined, which is the propagation distance in which the signal monotonically grows. After one coherence length the harmonic yield decreases until a further phase shift of π is accumulated.

With Eq. (49) the different methods for achieving best phase matching can be discussed. At first, the pressure, equivalent to the atomic density, plays a major role for the degree of phase matching [51]. Fig. 8 shows the calculated phase shift with increasing atomic density. The jet length is defined to be 250 μm long and the phase is calculated for different intensities. As can be seen, for high intensities (e.g. $1.5 \cdot 10^{15}\,\mathrm{W/cm^2}$) a phase shift of π is quickly reached within 7.2 mbar, whereas for low intensities (e.g. $3.5 \cdot 10^{14}\,\mathrm{W/cm^2}$) a phase shift of π can be observed only at 31 mbar, which is a factor of 4.3 higher. The corresponding pressures 7.2 or 31 mbar are the atomic densities where the signal stops to grow monotonically. It corresponds to exactly one coherence length.

Whether it is possible to reach densities corresponding to one coherence length depends on the XUV wavelength of interest and on the gas type used for HHG. The harmonic wavelength and gas type define the absorption length as the second limiting parameter besides the coherence length. The absorption length L_{abs} is the propagation distance in which the harmonic energy is reduced by a factor of 1/e. Fig. 9 shows absorption curves for argon and neon at 10.7 mbar pressure and an interaction length of 2 mm. Especially argon shows a tremendous absorption effect at 38 nm, a wavelength so far used for the seeding experiment sFLASH [53]. Generally, the HHG process can be characterized into phase- and absorption-limited HHG. In absorption-limited HHG, the harmonic signal decreases before the medium length corresponds to one coherence length. The origin of the signal reduction is wavelength-dependent absorption of the harmonic radiation in the medium. In this case, an optimal conversion efficiency in a long

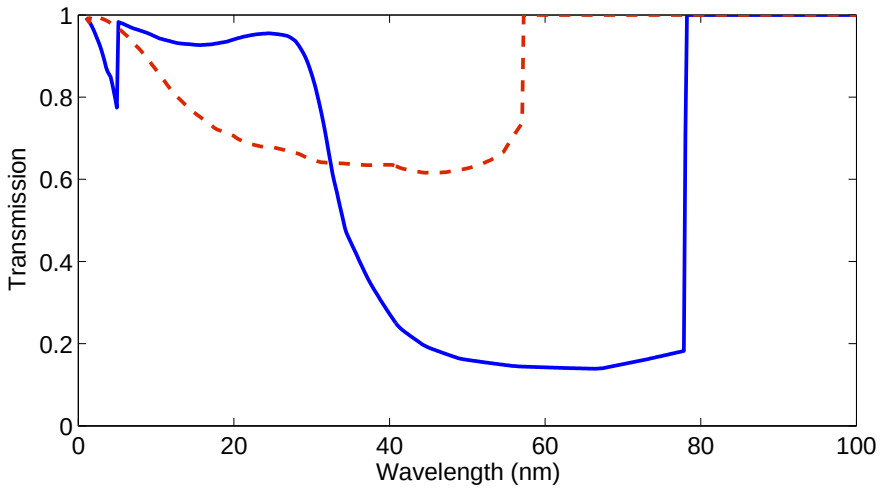

Figure 9: Transmission curves for argon (solid blue) and neon (dashed red) at 10.7 mbar pressure and with 2 mm interaction length.

uniform medium is obtained when $L_{coh} > 5L_{abs}$ [54]. Absorption-limited HHG can usually only be observed for lower harmonics [55], for sub-10 fs driver pulses in neon gas, it can be observed even down to wavelengths of 10 nm [56]. In phase-limited HHG, however, the coherence length is much shorter than the absorption length. Therefore, the origin of the signal reduction is the phase mismatch between different emitters. Whether phase- or absorption-limited HHG can be observed depends on the gas type and driver intensity.
The intensity of the focused beam is the second general tuning parameter of the HHG process, which needs to be discussed. The laser intensity will change the phase matching condition, because the ionization rates are directly coupled to the electric field (note, that not only the phase matching conditions changes with intensity but also the cutoff of the generation process.). For example, the gas medium can be positioned after the laser focus in order to reduce the effect of the Gouy phase shift to the total phase mismatch [57]. In such a case, the gas jet is in the divergent part of the beam, which implies a decreasing intensity. This leads to a variation of the phase matching condition due to a reduced ionization rate which is of opposite sign compared to the phase mismatch induced by the Gouy phase shift.
Finally, there is a third limitation for the HHG process, the effect of plasma defocussing [58, 59]. The ionization rate is not constant over the transverse profile of the pulse due to the transverse laser intensity distribution. Usually an enhanced electron density (e.g. a reduced refractive index) can be observed towards the intensity peak in the center which results in a defocussing effect. This influences the phase matching and the laser intensity of the HHG system. Plasma defocusing is especially important at high generation densities and high driver intensities.
All these limitation needs to be taken into account for optimizing the harmonic output and the harmonic coherence. Mastering these limitations is the key to intense attosecond pulse production and external seeding of FELs.

2.2.5 Quantum Paths and Coherence

One major result of the quantum-mechanical treatment of the single-atom HHG process discussed in section 2.2.3 is the derivation of an intrinsic phase, directly related to the time depen-

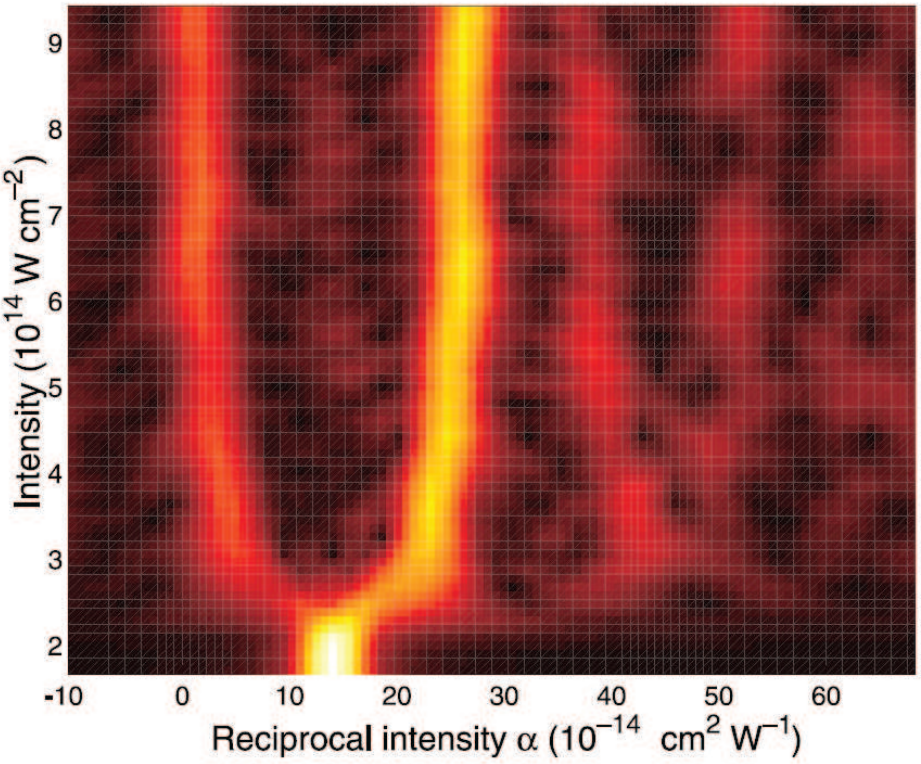

Figure 10: Pseudo-colour plot of the behaviour of the reciprocal intensity vs. intensity of the 45thharmonic. The colour scale gives the magnitude of successive Fourier transforms of the harmonic intrinsic phase as a function of intensity. This plot has been published by P. Balcou et al. in Ref. [60].

dent dipole moment. From Eq. (39) it is known that the dipole moment depends exponentially on the semi-classical action $S(\mathbf{p},t,t')$ accumulated by the electron during propagation through the continuum. The quasiclassical action $S(\mathbf{p},t,t')$ is approximately equal to the product of the electron average energy, gained by the electron, and the electronic travel or return time to its parent ion. As discussed earlier, the electron average energy is the ponderomotive energy. Defined already in Eq. (16), U_p is proportional to the intensity I and to the wavelength as λ^2. This leads to an intensity dependence of the quasiclassical action and its phase. Thus, the intrinsic phase can be written as [61, 62]

$$\phi_{QP}^{j} \approx U_p \cdot \tau_q^j \approx -\alpha_q^j I(r,t). \tag{50}$$

Under the assumption that the atomic potential is insignificant in comparison with the strong electric field of the driver laser, $S(\mathbf{p},t,t')$ represents the free electron motion in the continuum and hence its trajectory. The electron trajectories are solutions of Newton's equations for a classical electron in the presence of a laser field (compare section 2.2.2), and the initial condition is determined by the three saddle-point equations (41) - (43). The third saddle-point equation (Eq. (43)), which ensures the energy conservation, does rather not have any solutions for real tunnel times t'. Therefore, all solutions of the saddle-point equations are complex *quantum paths*. The classical trajectory can be treated as the real part of the quantum path. However, in the following, expressions such as trajectory and quantum path are used equivalently.
The trajectory character is imprinted in the travel time τ_q^j in the first relation of Eq. (50) (where j indicates the specific quantum path and q the harmonic order). The second relation includes the linear dependence on the intensity. The characteristic for the trajectory is expressed with the constant α_q^j, which is approximately proportional to the travel time τ_q^j for the q^{th} order. It implies that α_q^s is always smaller for the short trajectories than α_q^l for the long quantum paths. It can be determined by a method corresponding to a time-frequency analysis. This is possible due to the similarity between the exponential dependence of the dipole moment on the intensity and the time dependence of a multicomponent exponentially decaying signal [60]. Therefore it becomes possible to apply a window function cutting out a range of intensities and to perform a Fourier analysis. This is why α_q^j is also called the *reciprocal intensity*. Fig. 10 shows a colour map of the reciprocal intensity in dependence of the intensity, calculated and published by P. Balcou et al. [60]. The determination of the Fourier components has been done for the 45^{th}harmonic. An appealing result of Balcou's plot is the explicit dominance of two branches merging into one column at low intensities. This confirms quantum-mechanically that the concept of two major trajectories as potential paths within one half-cycle of the laser electric field in the plateau region of the spectrum is correct. The 45^{th}harmonic is shifted towards the cutoff with decreasing intensities until the two branches merge into the cutoff trajectory with a travel time of $0.65T$. From these calculations one can deduce the approximate numbers for the reciprocal intensity for harmonics in the deep-plateau region, given by $\alpha_q^s \approx 1 \cdot 10^{-14}\,\mathrm{rad\,cm^2/W}$ and $\alpha_q^l \approx 24 \cdot 10^{-14}\,\mathrm{rad\,cm^2/W}$ [60, 63, 64]. In the cutoff region, as stated before, these two trajectories merge into a single trajectory, characterized by $\alpha_q^{cutoff} \approx 13.7 \cdot 10^{-14}\,\mathrm{rad\,cm^2/W}$.
In conclusion, the competing quantum paths contribute with different phase to a single-atom dipole moment. Hence, by being approximately equal in strength, they are not phase-matched at the same conditions [65, 66]. As a consequence, the general expression of the phase mismatch Δk given by Eq. (49) is not complete if the concept of different electron trajectories is not taken into account [50]. The phase mismatch which needs to be minimizes for true phase matching

with the inclusion of the intrinsic phase is given by

$$\delta\Phi_q = \int \Delta k_q(z',t)dz' + q\arctan(z/z_R) - \alpha_q^{(j)} I(r,t), \tag{51}$$

where the first term is the phase difference due to dispersion of neutral atoms and free electrons with opposite sign. The second term is the dispersion term for the geometry of interaction and the final term is the intrinsic phase with its dependence on the trajectories. The total phase mismatch is therefore given by the sum of the atomic phase for each quantum path and the phase mismatch due to propagation in the medium ($\Delta k = \Delta k_{QP}^{j} + \Delta k_{prop}$), whereby the propagation phase is typically dominated by the plasma dispersion due to free electrons in the limit of strong ionization.

By controlling focusing, medium density and laser energy it is possible to approximately compensate for the phase mismatch of the desired quantum path. This results in a significantly different coherence lengths for the two trajectories, which allows a high degree of quantum path control [67, 68]. Such a control is desirable, because the spatial, spectral and temporal properties of the harmonic radiation rely intrinsically on the relative weight of the path-dependent contributions. In particular, the atomic phase has a strong influence on the temporal, spectral and spatial coherence properties of the generated XUV pulses [62, 69], which is imprinted in the observable spatially resolved harmonic spectrum [67, 70, 71].

In order to afford a more detailed description of the trajectory effect on the different coherence properties, the term *coherence* for higher order harmonics needs to be defined. The degree of coherence of a beam is based on the correlation between the temporal variations of the electromagnetic fields inside this beam [72]. The complex degree of coherence for two points inside the beam corresponding to the complex field amplitudes E_1 and E_2 is given by

$$\delta_{12}(\tau) = \frac{\langle E_1(t+\tau)E_2^*(t)\rangle}{\sqrt{\left\langle |E_1|^2 \right\rangle \left\langle |E_2|^2 \right\rangle}}. \tag{52}$$

The angular brackets stand for a time average over the harmonic pulse. The modulus of this equation is commonly known as the *degree of coherence*. Temporal (and therefore spectral) coherence can be deduced by applying Eq. (52) for $\delta_{11}(\tau)$, whereas spatial coherence can be described by $\delta_{12}(0)$.

Spatially there is another aspect besides the degree of coherence which is also very important for FEL seeding - the quality of the beam's wavefront. The wavefront quality is not identical to the degree of spatial coherence. Coherence is always related to the correlation *in time* of two fields emitted at two points at the time t. However, the spatial beam quality dependends on the wavefront quality and therefore on the *radial* variation of the driving laser intensity $I(r,t)$. A Gaussian or any other kind of radial distribution will lead to a changing intrinsic phase according to Eq. (50), which results in a curvature in the phase front. Clearly, the larger the reciprocal intensity the bigger the effect on the curvature. This makes a harmonic beam with a large contribution from long trajectories highly divergent. Hence, the phase front curvature of the short-trajectory contribution is smaller than that for the long-trajectory contribution resulting in a reduced divergence and therefore a dominant long-trajectory contribution in the outer region. The relative difference between the divergence of short- and long-trajectory radiation can be estimated using the geometrical approximation. This leads to a relation of $\Theta_l/\Theta_s = \alpha_l/\alpha_s \approx 24/1$. In real experimental conditions this difference is a bit smaller due to the fact that for the short

trajectory, the main driver for the angular spread is the diffraction limit[3]. The small distortions in the intensity profile, always present under real conditions, are basically irrelevant for short trajectories but are important for long trajectories, which are dominant in the outer region of the XUV beam. As a result, the M^2 parameter for the full harmonic beam will be always greater than one, sometimes even in the order of 30 [73, 68]. In this case, only if the center of the harmonic beam is filtered out, $M^2 \approx 1$ is achievable. This effect is enhanced at high intensity and high pressure setups. In these cases, the dense plasma causes heavy distortions of the radial intensity profile and therefore to a fast varying intrinsic phase for long trajectories.
In terms of spatial *coherence*, the plasma-induced phase shift due to the plasma dispersion is in the focus of the discussion. Two points in space need to be chosen for calculating the degree of spatial coherence with Eq. (52) (for example comparing the center and a point in the outer part of the harmonic beam). For high pressures the plasma-induced effects on the degree of coherence is not negligible anymore with the plasma density being a function of the radial intensity distribution. In the case of a Gaussian laser pulse, the ionization induced phase shift is higher in the center and lower in the outer region of the spatial profile. This leads to a decorellation between the center field and the fields in the outer region and hence to a reduced degree of coherence.
From Eq. (51) it follows that the dynamically induced intrinsic phase results in a dynamic phase matching dependent on the intensity profile. The *temporal* profile of the intensity $I(r,t)$ is therefore considered for the temporal coherence. Generally, for the time-dependent amplitude of the harmonic radiation (e.g. the temporal profile) the phase matching conditions are very important. For conditions where the peak of the time-dependent intensity leads to best phase matching for either the short or the long trajectory, the temporal coherence and profile of the harmonic beam are excellent, because no large intensity changes are present at the tip. As soon as best phase matching is achieved at an intensity below the peak, the temporal profile and the coherence can be highly distorted due to the influence of the intrinsic phase corresponding to the slope of the intensity change [72].
However, for the determination of the temporal and spectral coherence of the harmonic radiation, the harmonic *chirp* comes into the focus of interest, because the effective spectral broadening due to the intrinsic phase cannot be explained completely by the temporally varying harmonic intensity profile. Moreover, it is the varying temporal phase, that is responsible for perturbation effects in the spectrum. Note, that this harmonic chirp is not identical with the atto-chirp, which is an intrinsic chirp deduced from the single-atom response (see section 2.2.2). The harmonic chirp is a macroscopic effect of phase matching. The time variation of the driver intensity induces a change in the instantaneous frequency (e.g. a chirp) which is given as

$$\Delta\omega_j(t) = -\frac{\partial\Phi_j(t)}{\partial t}. \tag{53}$$

As a consequence, spectral broadening can be observed for large variations of the dipole phase with intensity. This is equivalent to a reduction of the degree of temporal coherence. To estimate the difference of broadening between short and long trajectories, the chirp can be calculated with the values for reciprocal intensity given above:

$$\frac{\Delta\omega_l(t)}{\Delta\omega_s(t)} = \frac{\alpha_l \cdot (\partial I(r,t)/\partial t)}{\alpha_s \cdot (\partial I(r,t)/\partial t)} = \frac{\alpha_l}{\alpha_s} \approx 24. \tag{54}$$

[3] A beam is *diffraction limited* when the product of the spot size at the focus and the divergence is of the order of the wavelength.

The spectral broadening seems to be a factor 24 higher for the long-trajectory radiation (which corresponds to a factor 24 reduction of the coherence length). However, similar to the discussion on spatial coherence, the short trajectory contribution is not dominated by the dipole phase but by the spectral bandwidth corresponding to the Fourier limit. Thus, the difference in spectral broadening is more in a range from 10 to 20 depending on the laser pulse conditions [62]. As a consequence, the presence of long trajectories can be directly seen in a spectrum where spectral broadening and interference only occur if the excellent coherence of the short-trajectory radiation is perturbed.
For experiments relying on a high degree of coherence and Gaussian-like spatio-temporal profiles, an ability to control the weight of the two competing quantum paths is very advantageous. Intensity variations from cycle to cycle can be expected in most of the current-day HHG experiments. The highest coherence of the harmonic beam is best achieved by the selection of the short quantum path. One possible method to achieve a high degree of coherence is to select only harmonics near the harmonic cutoff corresponding to a trajectory length of 0.65T, where the two quantum paths become degenerate. The significantly reduced efficiency at high harmonic orders near the cutoff makes this approach undesirable from a perspective of efficient harmonic generation, although it provides a convenient route for generating isolated attosecond pulses [74]. In the spectral plateau region, spatial filtering of the harmonic beam could improve the M^2 value by filtering the outer part dominated by the long trajectory. However, it needs to ensured that only the short trajectory is phase matched on axis. This can be done by applying moderate densities and intensities. Note, that by controlling the tajectory contributions on axis with the laser intensity or gas pressure, the harmonic efficiency changes with the intensity by $E_h \propto I^{5-7}$ (due to the tunneling rate without depletion), whereas the dependence on the particle density is given by N^2 in the phase matching regime, where N is the number of particles.

2.2.6 Quasi-Phase Matching

In the case of phase-limited HHG (e.g. absorption plays a minor role), the phase shift within the interaction length exceeds π or even higher orders of the coherence length. This leads to oscillations of the harmonic yield with a period of $\Delta\Phi = 2\pi$ as shown in Fig. 11a. The brightness of the generated XUV pulses can not exceed the value achieved at a density corresponding to one coherence length (N_{max}). The normalized density $N_n = N_a/N_{max}$ corresponds to the number of coherence lengths L_c with the atomic density N_a. For efficient HHG it is desirable to enhance the brightness of such pulses resulting in a harmonic intensity higher than that at N_{max}. In this sense, achieving absolute and independent phase control between multiple harmonic generation zones represents a major advance for HHG sources. It will allow the coherent superposition of multiple sources created by the same laser - an approach commonly known as *quasi-phase matching* (QPM) [75]. Unlike true phase matching, where the phase velocity of the driving field and the harmonic field must be equal, quasi-phase matching allows the coherent build-up of harmonic radiation, especially if true phase matching cannot be achieved. This is particularly important for the optimization of other critical HHG parameters, for example the cutoff photon energy given by Eq. (17). Thus, shortest wavelengths in the cutoff require high intensities leading to a high ionization fraction. However, for high ionization fractions the dispersion is dominated by the free electron dispersion and true phase matching can no longer be achieved over the complete interaction length. Under such conditions QPM is generally accepted to

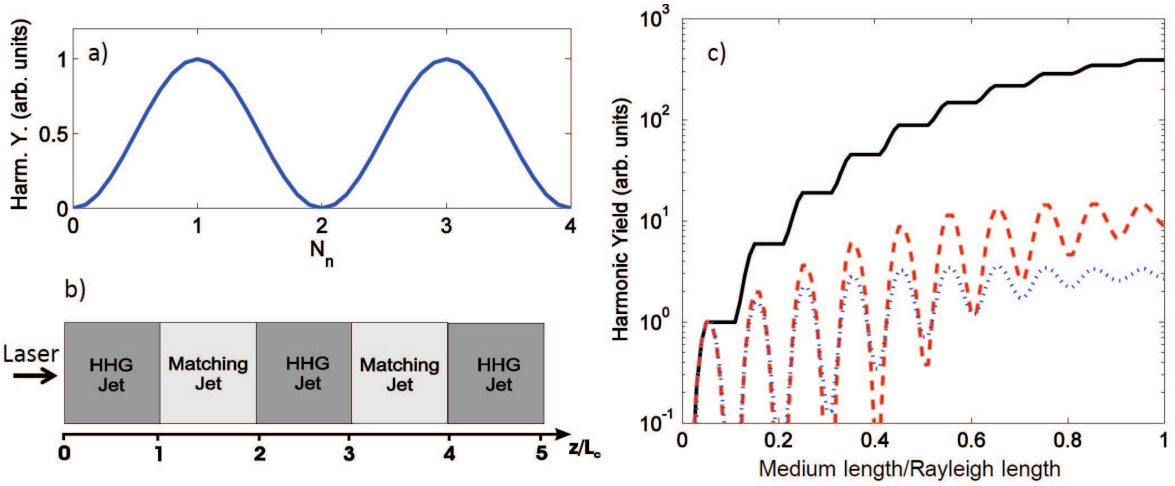

Figure 11: a) Harmonic yield oscillating due the phase mismatch in dependence of the normalized density $N_n = N_a/N_{max}$. b) Schematic of the QPM concept with alternating generation and matching zones. c) Harmonic yield with $N_{QPM} = 10$ in the focus of a Gaussian beam. Phase matching is assumed to be ideal for all cases and the medium extends over one Rayleigh range centered at the focus. Ideal QPM (no absorption and full modulation depth, black line) results in rapid signal growth. For comparison QPM with a sinusoidal intensity modulation of 4% is shown without absorption (dashed red line) and with absorption assuming a medium with two absorption lengths (dashed blue line).

be the only option to achieve coherent signal growth along the medium and hence to achieve high brightness and high conversion efficiencies. In the case of HHG, QPM is typically implemented by allowing the signal to build up over one coherence length $L_c = \pi/|\Delta k|$ (the HHG half period) and subsequently suppressing HHG for another coherence length (the matching half period), until the driving field and harmonic field are again in phase (see Fig. 11b). Since the harmonic intensity of N atoms emitting radiation coherently increases as N^2, the superposition of N_{QPM} identical HHG sources will increase the intensity of the q$^{\text{th}}$harmonic as $I_q \propto (N_{QPM})^2$ under ideal conditions (N_{QPM} is the number of QPM periods consisting of a generating and a matching half period).

QPM can be achieved by any means that allow modulation of the source term strength. Fig. 11c shows such a modulation for 10 QPM periods positioned in the focus of a Gaussian beam. The generating medium has a length equal to the laser Rayleigh range. A permanent increase of the harmonic yield with constant signal during the matching half period can be observed for perfect phase matching (e.g. between the generation zones a phase shift of π is assumed) and a sharp modulation of 100%. For a sinusoidal modulation with a modulation depth of only 4% there is still an increase in the signal but folded with phase oscillations showing a peak for odd numbers of the coherence length. This nonideal signal growth is even reduced when the effect of absorption is included. Hence, the reduction in the signal growth due to nonideal modulation depth and also due to absorption can be very substantial.

The modulation of the source term can be achieved with different methods, modulating either the driving field or the generating medium. By modulating the driving field, the intensity should be below the threshold intensity for HHG in the matching zones, whereas highest intensities should be reached in the generating zones. This was shown experimentally with modulated

capillary diameters [75, 76] or multi-mode beating in a capillary [77, 78], by using counter-propagating pulses [79] and by polarization gating [80]. Alternatively, the atomic density of the generation medium can be modulated [68, 81] either using multiple jets [82, 83] or by a capillary discharge [84]. These approaches have been highly effective for the validation of the QPM principle for HHG. Nevertheless, there is still room for improvement in terms of applications beyond short term measurements and in terms of achieving signal growth close to the ideal $(N_{QPM})^2$ scaling.
The trajectory dependence of the phase mismatch due to the intrinsic phase contribution leads to effective control of the relative weight of the two quantum paths. By varying the phase in the matching zones, tuning to best on-axis phase matching for the short trajectories becomes possible. This results in a spatially and temporally coherent harmonic beam well suitable for FEL seeding. This ability of quantum path control with QPM has been experimentally shown for the scheme of counterpropagating pulses [85] and theoretically predicted for a modulated density using a multijet array [81].

2.2.7 Attosecond Pulse Generation and HHG

With the growing number of groups involved in the HHG research, more and more features of the harmonic radiation could be revealed. One fascinating finding was the fact that harmonic radiation in the time domain can be understood as trains of attosecond pulses [86, 87]. Just as sub-picosecond or femtosecond pulses have led to the resolving of different processes on molecular scale, attosecond pulses will enable new experiments to resolve electronic dynamics. The microscopic HHG response, however, does not generate usable attosecond pulses [88], which is surprising due to the fact that the optical half-cycles of the driving field, responsible for harmonic emission, can be considered to be on a natural time scale close to the attosecond regime. However, from the previous discussions it is known that for any energy below the cutoff there are two main quantum paths corresponding to different ionization and return time pairs but leading to the same return energy. Hence, the radiation consists of at least two overlapping bursts of attosecond pulses per optical half-cycle so that no clear periodicity can be extracted. Usable attosecond bursts are therefore only achievable at the cutoff, where only one burst per half-cycle is present, or by taking advantage of macroscopic effects which are intrinsically present in real experiments. At the detector, the harmonic radiation is the coherent sum of all radiating atoms including phase matching effects. It becomes clear, by including the macroscopic effects attosecond pulses are not intrinsically generated within the process of HHG, but rather within a *tuning* process. The ultimate goal of an optimized attosecond source is the detection of isolated pulses (for very short driver pulses with just a few optical cycles) [89] or trains of distinct attosecond pulses (for longer driver pulses) [87].
For a single attosecond pulse production the harmonic radiation needs to be gated or filtered in space, time and frequency. This is actually not surprising, because the previous sections already discussed the influence of the competing trajectories on the coherence properties. These properties are directly related to the periodicity of attosecond pulse trains. This periodicity, which leads to distinct pulses, can be achieved by the selection of the short trajectory harmonics by coherently control the phase between successive sources. In addition, spatial filtering can be done in the far field to block the highly divergent part of the long trajectory. Spectral filtering is also necessary, because only a broad band section of the spectrum can lead to short intense pulses. Note, that with this knowledge the harmonic spectrum can be considered as pure interference

of attosecond pulses within a pulse train which forms the harmonic radiation. Isolated attosecond pulses achievable with very short laser pulses ($\leq 5\,\mathrm{fs}$) can only be produced if the carrier envelope phase (CEP) of the driver field is stabilized. The result is a continuous spectrum for high harmonics due to constant phase relations between generated bursts [90]. As soon as the phase is random, interference will again lead to a distinct spectrum with only odd harmonics.

3 Seed Source Implementation at FLASH2

In this chapter the FLASH facility at DESY Hamburg and the proof-of-principle experiment for XUV seeding at FLASH is presented in the first sections. This is followed by an introduction to the new FEL FLASH2 which is currently under construction. The last sections incorporate personal contributions concerning the source implementation and seeding diagnostics. It includes first concepts for the injection scheme as well as a concept for the seeding diagnostics. A major concern within this work was the development of a new XUV spectrometer as a source diagnostic tool. In the last section, seed requirements are derived from simple GENESIS simulations [10].

3.1 The Free-Electron Laser FLASH

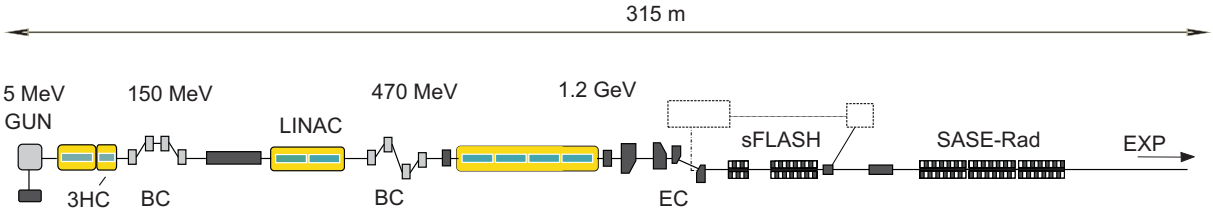

Figure 12: A schematic of the current design of the FLASH FEL. An electron bunch is formed by photoemission of a Cs_2Te photocathode with a 262 nm laser pulse (injector laser). The third harmonic cavities (3HC) are used to linearize the phase space distribution leading to a quasi-Gaussian temporal bunch profile. The linear accelerator (LINAC) consists of 7 acceleration modules and two bunch compressors (BC). An energy collimator (EC) is used to limit the energy spread before the electrons enter the undulator section (SASE-Rad). The FEL pulses are finally transported to the experimental hall (EXP).

Free-electron lasers, such as the free-electron laser in Hamburg at DESY (FLASH, see Fig. 12), deliver intense coherent radiation within a wavelength range down to soft X-rays. With the start of user operation in 2005 [91], FLASH became a powerful tool for various experiments in material science [92], ultrafast dynamics [93] or biological research [94]. The 315 m long FEL consists of 7 superconducting acceleration modules which accelerate the electron bunches to a maximum energy of 1.25 GeV, allowing SASE-lasing from 4.45 to 60 nm in the fundamental [95]. Recently, a fundamental wavelength of even 4.1 nm has been demonstrated [96]. The acceleration takes place in the resonator cavities, in which an electric field oscillates as a standing wave. The frequency of this standing wave is 1.3 GHz which determines the timing of the entire FEL. Considering the electric field as a sine wave, the electrons need to be injected such that they coincide with the part of the field where an efficient energy transfer from the field to the electrons is possible. The electron experience thereby acceleration.
The peak current of the electron bunch needs to be in the range of kiloamperes for the FEL operation, which makes bunch compression at relativistic energies necessary. If the center of the relativistic electron bunch coincides with the rising slope of the accelerating electric field and not with the peak, electrons at the head of the bunch are less energetic than the ones at the tail, after passing an accelerator module. Consequently, in a subsequent magnetic chicane the less energetic particles follow a longer trajectory than the electrons with higher energy leading

to a net compression of the electron cloud[4]. As a comparison, bunches accelerated at the peak of the sine-like field experience no compression due to the balancing character of the energy chirp distribution. In this case, one half coincides with the rising and the other half with the falling slope of the accelerating electric field. Thus, the two halfs of the longitudinal charge distribution has energy chirps of opposite sign.
FLASH can operate in two different modes allowing XUV pulse durations from 10 to 200 fs (RMS). The short pulse operation mode takes advantage of the nonlinearity in the longitudinal phase space caused by the sine-like electric field in the accelerator cavities. As discussed before, bunches accelerated at the rising edge of the accelerating electric field leave the cavities with an intrinsic energy chirp. The energy chirp can be expected to be nonlinear because of the nonlinear (sine-like) shape of the field. Thus, the bunch compressors produce a non-uniform charge distribution with a high peak ahead of the electron bunch followed by a long low charged tail. The high current peak is the only part of the bunch involved in the FEL lasing process and can lead to FEL pulse lengths down to 10 fs (RMS). A disadvantage of this operation mode is the asymmetry in the longitudinal bunch profile which makes predictions of beam dynamics and FEL properties complicated and requires sensitive beam diagnostics. However, this drawback does not affect the overall performance of FLASH. This mode of operation is very well established if short FEL pulses are required. The long pulse mode relies on a linear energy chirp within the electron bunch, which can be achieved with third harmonic cavities operated at a frequency of 3.9 GHz. These cavities are implemented after the first acceleration module behind the electron gun in order to linearize the phase space distribution. Together with the magnetic chicanes this produces a quasi-Gaussian longitudinal electron beam profile generating FEL pulses with a duration of up to 200 fs (RMS) [98].
The energy spread accumulated during the acceleration and compression needs to be limited, before the electron bunches are used to produce high intensity radiation. This is done by an energy collimator: a dispersive section with dipole magnets as deflecting elements. Likewise a bunch compressor is a chicane, it transfers an energy chirp into a spatial chirp. Electrons with the largest energy deviation from the reference energy are now located within the outer part of the dispersed bunch and by simply inserting copper blocks a reduction of the energy spread can be achieved. The deviating electrons are simply removed by absorption. However, the expected energy spread of $\pm 1\%$ from the accelerator [99] is smaller than the $\pm 3\%$ acceptance of the collimator [100] so that no manipulation is necessary under standard operation conditions.
The FEL radiation is produced in a 30 m long fixed gap undulator with permanent magnets. The standard operation of the FEL relies currently on the SASE process (see section 1.2). Characteristically, the SASE amplification starts with spontaneous light emission (shot noise) of the electrons passing through the alternating magnets of the undulators. As discussed in section 1.2, the spontaneous radiation, experiencing a slippage to the electron packets, imprints a modulation in electron bunches, which leads to the formation of a micro-bunch structure in the nanometer regime. This small-scale density modulation is responsible for the coherent lasing process within the FEL. The start-up of SASE from a stochastic process leads to shot-to-shot fluctuations of the produced radiation in terms of pulse energy, temporal and spectral distributions [101]. In addition to the stochastic effects on the amplified radiation, another undesired effect is the large arrival time jitter of the XUV radiation at the FEL experimental hall. This effect occurs mainly due to an uncertainty in the arrival time of the electron bunches. This reduces the temporal resolution for pump-probe experiments to > 100 fs (RMS), thus limiting the

[4] A detailed description of the compression process can be found in Ref. [97]

precision of these measurements. A better resolution of tens of fs can be achieved with timing electro-optic sampling methods to measure the pulse arrival time [102, 103] or adopting precise synchronization schemes [104].
A promising method to improve both the longitudinal and spectral coherence and the timing performance of the FEL is direct seeding via high harmonic generation (HHG) driven by an infrared laser in a noble gas [5]. In this case, the FEL process does not start from noise but from a defined external seed source which transfers its properties to the FEL pulse. The precision of pump probe experiments will be dramatically increased, because accurate synchronization between a separate pump-probe laser system and the driving seed laser amplifier is already possible with a precision of < 10 fs [104, 105]. Seeding will make the FLASH pulses more comparable to a table-top laser pulse, in particular in terms of its temporal stability and coherence. Given the soft x-ray wavelength regime in connection with high repetition rates (up to 1 MHz) and high pulse energies (μJ-level), this will open up a new field of applicabilities for this FEL. A feasibility study for FEL seeding at FLASH is currently ongoing with the experiment sFLASH [53, 106]. The sFLASH driving seed laser amplifier itself is used as pump-probe laser system leading to intrinsic synchronization between pump and probe beam as described in more detail below.
A new undulator beam line, FLASH2, is planned to incorporate new developments for FELs. It shares the common linear accelerator (Linac) with FLASH and consists of a new undulator section and an experimental hall [107]. This FEL will be a user facility with SASE and seeded-FEL operation mode. FLASH2 will be described in the third section within this chapter.

3.2 Seeding at FLASH - The sFLASH Experiment

The seeding principle was first experimentally demonstrated at SCSS in Japan [5]. More seeding experiments are currently set-up, for instance at SPARC in Frascati at 401 nm [108], at SCSS at 61.5 nm [109] and a proof-of-principle seeding experiment is also installed at FLASH (sFLASH) [53]. The aim of the sFLASH experiment is to measure seeded FEL pulses in the XUV regime below 40 nm for the first time, which is theoretically predicted to be possible within the parameter set of the FLASH Linac. To approach the short wavelength regime, seeded operation will be first shown at 38 nm (21^{st} harmonic of the 800 nm driver). If successful seeding can be demonstrated in this configuration, it will be followed by a test at 13.1 nm (61^{st} harmonic). In Fig. 13 a schematic of the experimental layout of sFLASH is presented, consisting of a harmonic source, driven by a 10 Hz, 50 mJ, 35 fs CPA laser system, a 10 m long variable gap undulator section and an experimental station. The HHG source consists of a 20 mm long gas jet. The target position can be varied with respect to the focal position of the driver laser. Argon is used as HHG medium for efficient wavelength conversion to 38 nm, whereas neon is more adequate for 13.1 nm. The beam line system was constructed to only transport the 21^{st} (or 61^{st}) harmonic to the undulator, which can be tuned to the required resonance wavelength. The undulators are variable gap undulators to be more independent of the Linac parameters (e.g. electron beam energy).
Currently, the experiments at 38 nm seed wavelength are ongoing. The XUV beam is injected into the beam line with a transmission efficiency of about 5% due to numerous mirrors required because of geometrical constraints in the FLASH tunnel [110]. The HHG process delivers a maximum of 2 nJ harmonic energy within the 21^{st} order, which results in a seed energy in the

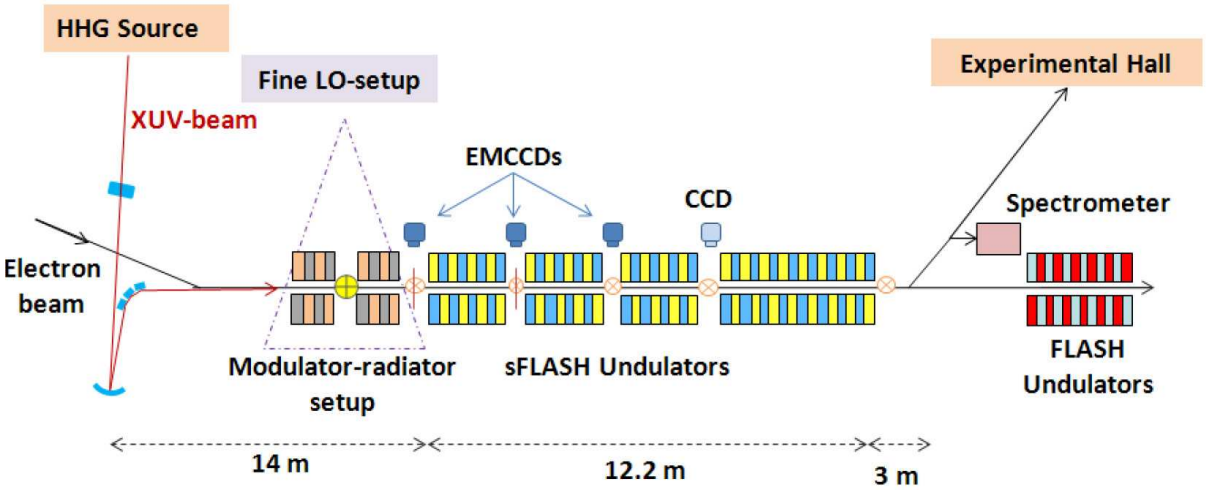

Figure 13: Schematic of the seeding experiment sFLASH (courtesy of R. Tarkeshian). The XUV seed beam generated by HHG in a noble gas is injected into the FEL by several mirrors reducing the harmonic energy to about 5% of its original value. Amongst others, a modulator/radiator setup is used to find the longitudinal overlap (LO) and several screen stations equipped with CCDs provide control of the transverse position of electron and XUV beam. The 12.2 m long undulator section is followed by a mirror chamber used to guide the seeded FEL radiation into an experimental hutch. The FEL beam can be deflected into a XUV spectrometer at the extraction beam line for spectral diagnostics.

FEL of at least one order of magnitude below the initial energy. As discussed in section 1.3, a key challenge of the seeding operation is the successful overlap between the electron bunch and the XUV seed beam in the six-dimensional phase space. At sFLASH the transverse overlap is achieved with several diagnostic tools distributed along the sFLASH section to control the absolute position, propagation angle and divergence of the two beams. The electron beam position and dimension are measured with beam position monitors (BPM) [111] and optical transition radiation screens (OTR) [112]. Furthermore, Cerium-doped YAG crystals are used for the XUV beam position and size measurement.
In addition to the transverse overlap, the longitudinal position (or timing) of the seed beam and the electrons needs to be matched within a certain precision. This precision depends on the duration of the electron bunch, because the XUV beam is rather short (about 15 fs FWHM). To relax this requirement, sFLASH will only operate with the third harmonic cavities to ensure a minimum bunch length of 100 fs (RMS). The timing overlap is achieved in three steps [113]. Firstly, a photomultiplier or photodiode is used to determine the overlap within a precision of 1 ns. This technique is well known and frequently used in laser systems. Secondly, a streak camera is positioned near the FEL beam line detecting the relative longitudinal position of the infrared pulses of the HHG driving laser and the synchrotron light emitted by the electrons passing a short undulator (the modulator, see Fig. 13) right after the injection mirror chamber. The precision of this measurement is about 1 ps. Finally, for femtosecond precision, a second small undulator (radiator), which follows the modulator, uses the same concept as the optical replica experiment, which is described in Ref. [114]. If coherent light emission at 800 nm is detected from the radiator, the overlap of seed and electron beam is achieved within a few fs precision.
Presently, no signal enhancement of the FEL radiation due to seeded operation could be ob-

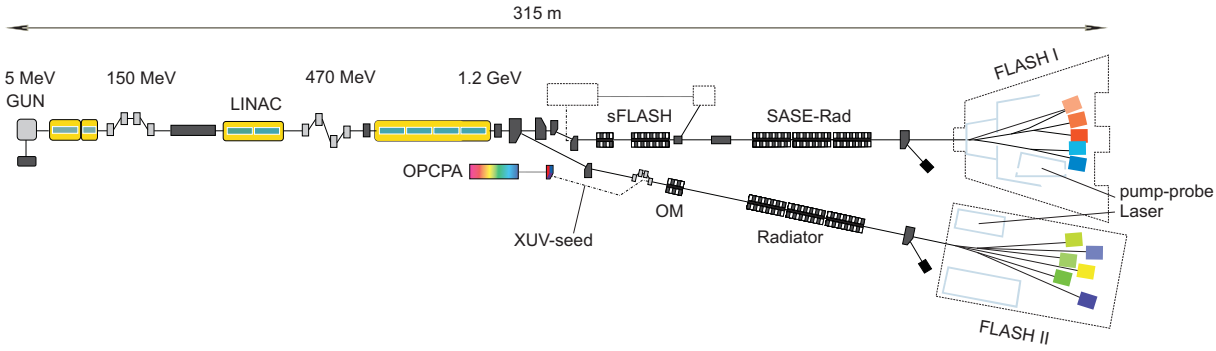

Figure 14: Layout of the future FLASH facility. The FLASH2 FEL beam line shares the same Linac as FLASH1. FLASH2 is planned to operate at wavelengths between 4-80 nm in SASE mode or 10-40 nm in direct seeding mode. An extension to shorter seeded wavelengths is planned. (OPCPA: optical parametric chirped-pulse amplification, XUV: extreme ultraviolet, OM: optical monitor)

served [53]. All diagnostic tools are well tested and commissioned. Problems are caused by the low transmission efficiency of the seeding beam line but also by the inflexible focusing optics offering only three distinct focal lengths. The resulting seed energy losses due to poor coupling to the electron beam could be minimized with an adaptive optical system. Such a focusing mechanism is planned for the next upgrade. With complete transverse overlap, the total energy of the harmonic beam present in the undulator section would be coupled to the electron beam so that 5% (0.1 nJ) of the source energy contributes to the seeding process. However, harmonic energies below 1 nJ will lead to a high shot noise pedestal in the signal and thus a poor contrast between seeded and un-seeded FEL radiation [115]. The energy coupled to the electrons was estimated to be 10 pJ at sFLASH which results in a contrast ratio of about 1.3:1 between seeded and spontaneous FEL radiation [113]. This is almost impossible to detect. To improve the contrast between the seeding pulse energy and the shot noise of the FEL, higher seed energies are additionally required. However, this brings conventional one-jet, absorption-limited HHG sources to its intrinsic limit.

3.3 The new FEL Beam Line FLASH2

A new undulator beam line will be implemented in the FLASH facility to extend the usability of the FLASH FEL. This is necessary due to higher demands on the beam characteristics and a permanently increasing number of user beam time requests, which cannot be covered by the FLASH FEL in its current design. Because the FLASH tunnel does not allow an easy extension, a new tunnel is necessary and the construction has already been started in summer 2011. An overview about the most important features of FLASH2 is followed by a deeper understanding of the implementation of a HHG seed source. The implementation concepts were developed as part of this PhD. The last section deals with the requirements for seeding FLASH2, which has been gained by simple GENESIS simulations [10].

3.3.1 General Information

A schematic of the new FLASH facility is shown in Fig. 14. A FEL with SASE and seeding operation mode is proposed depending on the user's request. FLASH2 will share the same acceleration structure as FLASH (will be named FLASH1 in the following) and will thus be operated with the same electron beam energy. The separation takes place right before the energy collimator with a fast dipole kicker. Two kicker schemes are considered. The first operation mode would deflect every second bunch train into the FLASH2 beam line, leading to a reduced burst repetition rate of 5 Hz by maintaining the bunch repetition rate within the train. A second operation mode would divide the bunch train into two parts which conserves the burst repetition rate of 10 Hz. The new beam line tunnel has a thick wall separating FLASH1 and FLASH2. This allows separate maintenance of the FEL lines and flexible operation.
The bisection between the two tunnel sections is followed by matching diagnostics and a chicane for the HHG seeding injection mirror chamber. After the magnetic chicane, a small undulator will be installed to control the longitudinal overlap between the XUV seed pulse and the electron bunch. FLASH2 will have variable gap FEL undulators with an undulator period of 31.4 mm. The FEL wavelength of FLASH2 can thus be chosen quasi-independently of the electron beam energy used to tune the FEL wavelength at FLASH1. The undulators are configured for SASE operation from 4 to 80 nm. Helical undulators, implemented as an add-on in the beam line, will offer the possibility to change the polarization of the XUV pulses.
The direct seeding via HHG, however, will cover a wavelength range of 10-40 nm. The restriction to this regime is due to the HHG conversion efficiency and tunability of an XUV source. So far, adequate efficiencies ($> 10^{-6}$) and stable conditions can be expected for wavelengths only above 10 nm with the source concepts under development (see section 5). The wavelength regime can be extended to shorter wavelengths as soon as better results concerning the conversion efficiency can be achieved. Direct seeding will impose strict requirements on the whole system concerning beam transport, diagnostics and beam manipulation. The quality of the seeding process relies almost exclusively on the XUV source driven by the IR laser system. Therefore, the development of an amplifier system and a HHG source, meeting all requirements of a seeded FEL such as FLASH2, is the major concern of this seeding project.
As a second option, besides direct seeding with a HHG source, high-gain harmonic generation (HGHG) stages can be implemented in the beam line [116]. For this scheme a 200 nm laser beam modulates the electron bunch in a first undulator (modulator). In a dispersive chicane the energy modulation is transferred into a density modulation which results in FEL radiation within the next undulator (radiator). A higher harmonic of this FEL radiation can then be used to seed a second HGHG cascade. Additionally, echo-enabled harmonic generation (EEHG) could be a third option to improve the characteristics of the FEL radiation [117]. This scheme would also require further undulator cascades with magnetic chicanes. The advantage in comparison to HGHG is the lower field amplitude needed for bunch modulation. The EEHG scheme is still in the development phase. However, a proof-of-principle experiment was already performed demonstrating successfully the physical effects of EEHG [118]. This seeding scheme could be implemented at FLASH2 at a later stage.

3.3.2 Injection Scheme for direct HHG Seeding

A flexible configuration of the XUV seed injection scheme is necessary to ensure adequate overlap within the six-dimensional phase space. The seed pulse will be coupled into the FEL

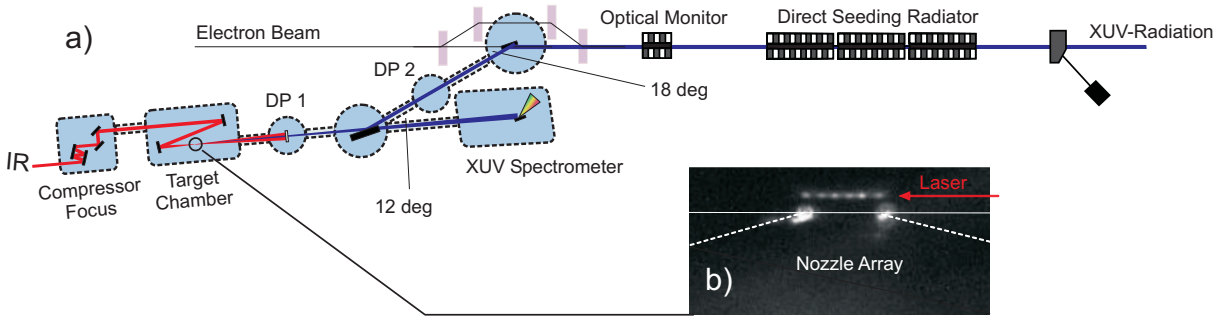

Figure 15: Injection scheme for the HHG seed radiation. a) The optical laser pulses (800 nm) are transported from a laser laboratory located next to the FEL tunnel. The focusing takes place in the first HHG setup chamber. The focused beam produces XUV radiation in a HHG gas target which is then imaged into the FEL passing a focal and a planar mirror. The focal mirror can be removed for spectral diagnostics. b) Plasma side image of a quasi-phase matching multijet array seeding target with 6 Argon jets (see section 5).

at a position approximately 9 m from the first SASE undulator entrance using a dispersive chicane (see Fig. 15). The magnetic chicane deflects the electrons and a mirror can be inserted in the beam path without disturbing the electron beam. The bending magnets are modified electro-magnetic CV15 dipoles from the old accelerator ring HERA (at DESY). The pole plate is 300 mm long and the coils each have 1332 windings. The dipole yoke was rebuilt such that an electron deflection of 12 mm can be achieved within 1 m path length without saturation.
For direct seeding the saturation length of the FEL will be shorter than for SASE. In addition, so far, seeding is not planned for wavelengths < 10 nm. Therefore, in seeding-mode the first FEL undulator gaps will be fully open, not contributing to the lasing process. The increased distance to the first radiator allows moderate focusing of the seed into the FEL undulators with an adequate overlap within one or two gain lengths. The power gain length of the FLASH2 FEL is 1.0-0.5 m for the wavelength range from 10-40 nm.
The seeding setup is a complex installation with a driving laser system, a gaseous HHG target and infrastructure for beam transport and insertion into the FEL. The HHG seed driver amplifier will be located in a laser laboratory directly connected to the new FLASH2 tunnel. Right after the last OPA stage, the laser pulses are transmitted into a vacuum chamber. In this chamber final compression will ensure the pulse length of 10-15 fs required for efficient HHG and FEL seeding. The compressed optical pulses will be transported to the HHG chamber via a vacuum pipe crossing the controlled area of the FLASH1/2 junction. The laser pulses enter the HHG chamber with p-polarization which is necessary for the FEL seeding process, because of the horizontal oscillation plane of the electrons in the undulators. The first chamber in the FLASH2 tunnel will contain an off-axis parabolic mirror optimized for an angle of 90°. The mirror is mounted on a motorized x-y-z-stage to remotely control the alignment. The laser is focused into a noble gas target located in the following interaction chamber equipped with an efficient pumping system and a dual-gas XUV source for high-order harmonic generation.
The HHG radiation propagates at an inclination angle of 6° to the electron beam pipe for about 2.5 m to a mirror chamber containing a movable focusing mirror. The focusing element will be coated with a dense carbon coating [119] providing a total reflectivity of $\approx 85\%$ for p-polarized light at 6° deflection angle and for 10 nm and higher (see Fig. 16).

With the mirror inserted, the XUV radiation passes the mirror with a reflection angle of 6° and is reflected by a planar mirror into the FEL. The reflection angle at the electron beam line is 9° resulting in a lower reflectivity as can be seen in Fig. 16. The total reflectivity of the system is the product of the two mirror reflectivities and is between 59.6 and 67% for the wavelength regime of interest.

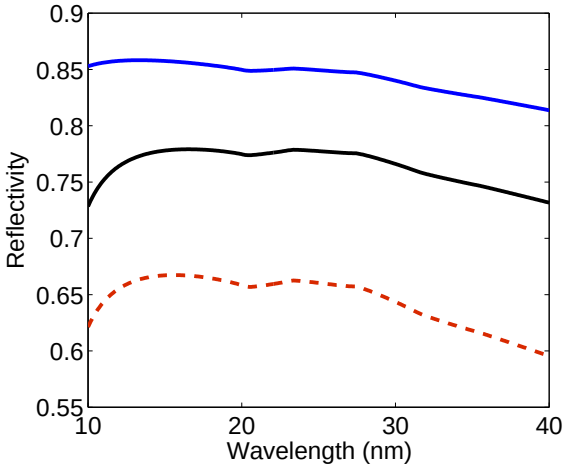

Figure 16: Reflectivity of the carbon coated mirrors. The focusing mirror (solid blue) has a reflectivity of 85.8 to 81.4% within 10 to 40 nm, and the planar injection mirror (solid black) between 73.2 and 77.9%. The total reflectivity is the multiplication of both reflectivities (dashed red).

The focusing mirror needs to be an adaptive system to meet the requirements of a tunable seeded FEL. The source has to be imaged to a size approximately equal to the electron beam size (65 μm (RMS) at the design energy of 1.2 GeV) in the undulator section to ensure an adequate overlap between the XUV seed and the electron beam in the FEL. Additionally, the overlap has to be ensured for at least two power gain lengths of the FEL (1-2 m) to override the shot noise power. This leads to a sharply defined Rayleigh length which limits the choice of focal lengths for the focusing mirror. In addition, an adaptive focusing mirror is also planned for the driver laser to control the source size of the XUV beam. However, for adequate intensities within the gas jet, a laser focus of 60 to 150 μm (FWHM) is needed and a XUV source size of 0.2-0.4 times the focal spot is expected. This limits the flexibility of the source size and restricts the required freedom of the XUV focusing mirror. With an adequate adaptive focusing system the HHG source can be imaged into the undulator with a magnification factor of 2-13. This keeps the image size constant to a diameter comparable to the electron beam.

At least two differential pumping stages will be located within the 4 m between the HHG gas cell and the electron beam pipe. This ensures that the accelerator vacuum is not affected by the poor HHG chamber vacuum caused by the pulsed gas jets. The differential pumping stages have to decrease the pressure from 10^{-3}-10^{-4} mbar to about 10^{-8} mbar in order to meet the high demands of the FLASH vacuum system. Thus, using two pumping stages, every stage has to provide a pressure reduction of 2 orders of magnitude assuming a pressure of $\approx 10^{-4}$ mbar in the target chamber. In front of each pumping stage of 2 m length an aperture of 20 mm has to be set in between to get the full decrease, with an effective pumping power of 200 l/s. The apertures are set to be variable in order to have the possibility to correct for changes in the parameter space.

3.3.3 Diagnostics

Several beam diagnostics are needed to remotely operate the HHG source and to characterize the seed pulses. Beam-steering, transverse position and waist position of the optical laser must be remotely monitored and controlled. The focusing mirror in the chamber behind the target will be movable in order to let the XUV beam enter a diagnostic chamber for spectral analysis

(see also Fig. 15). A XUV spectrometer has been developed to detect the HHG radiation from 1 to 62 nm (see next paragraph for more details). Further diagnostic tools are required to ensure an optimum alignment of the imaging mirror and the reproducibility of the HHG beam positioning inside the undulators. The mirror chambers will be mounted on movable axes to align the system within at least 4° of freedom. The motors need to have a precision of micrometers for translation and mircoradians for rotation to ensure an adequate overlap within the undulators, 15 to 30 m away from the focusing element.
A compact diagnostics chamber incorporating imaging screens and an electron beam position monitor will be installed at several positions between the magnetic chicane and the last undulator exit for the transverse overlap diagnostic in the FEL. These types of diagnostics are currently tested at sFLASH. The screen arrangement consists of a fluorescent Ce:YAG plate to monitor the HHG beam position and its spatial profile, and an optical transition radiation screen for electron beam positioning and profiling. These diagnostics will be essential to determine the spatial overlap of the seed and the electron beam with very high precision ($< 10\,\mu$m). A streak camera (Hamamatsu FESCA-200) will be used for the temporal overlap between the electron bunch and the HHG seed pulse with > 500 fs precision using synchrotron radiation from the last bending magnet and a small fraction of the IR seed beam. As a permanent monitor for the temporal overlap after the commissioning phase of FLASH2, an optical monitor will be installed which is simply a very small undulator tuned to the resonance wavelength of the IR driver laser showing enhanced signal when temporal overlap is achieved. The optimal temporal overlap (< 10 fs) is adjusted by scanning the timing of the seed laser in small steps until optimal radiation output power is observed. Valuable experience with these techniques and concepts has been gained with the sFLASH setup and very successful tests have been done during the last experimental periods [53].
A new and convenient tool will be implemented for spectral diagnostic of the FEL radiation. In contrast to FLASH1, FLASH2 will be equipped with an online spectrometer to control the SASE and seeded operation without disturbing user operation.

3.3.4 The XUV Spectrometer

To characterize and control the source parameters, an XUV spectrometer with a wavelength range from 1 to 62 nm has been developed. Although a few companies provide compact spectrometers operating in the XUV, the specific requirements of FLASH2 made a new development necessary. The demands on such a diagnostic tool to be implemented in the FLASH2 tunnel are as follows:

- A wavelength range of 1-60 nm needs to be covered.
- The spectrometer is positioned about 3 m from the source which makes a slit necessary. This requires different gratings for highest grating efficiencies at specific wavelengths.
- Filters and gratings need to be changed remotely due to limited access to the tunnel.
- The information on the absolute values of harmonic energy needs to be extracted from the spectrum.
- Direct beam profile and divergence measurements need to be possible.

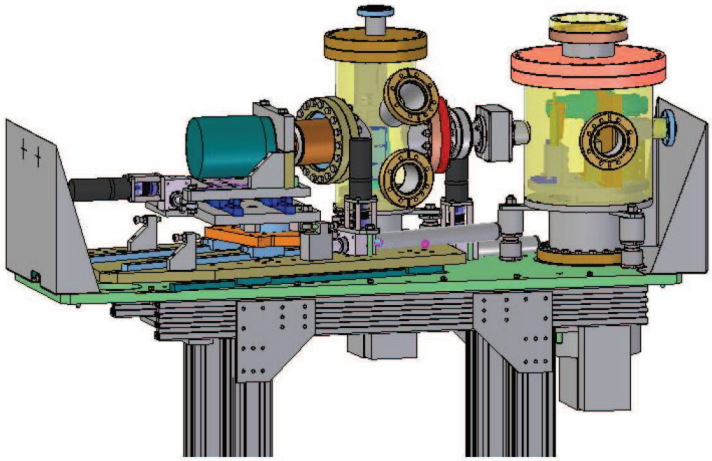

Figure 17: The new XUV spectrometer specially designed to meet all requirements for an installation in the FLASH2 tunnel. Two filter wheels equipped with thin metal foils block the infrared light. After the filters a XUV diode can be moved into the beam for direct intensity measurements. Three different gratings are used for spectral analysis. The harmonic radiation is detected by a movable XUV CCD.

No such spectrometer exists as a commercial product. Therefore, a new development was essential and the current design can be seen in Fig. 17. The wavelength range is chosen to be 1-62 nm in order to include possible upgrades of the XUV source such as an extension of the wavelength range down to the water window. The spectrometer consists of a filter chamber equipped with two motorized filter wheels each of them configured with a maximum of five filters. The fundamental is usually filtered by thin aluminum or zirconium filters. Additional filters can be interesting for wavelength calibration or background measurements. Behind the filter wheels, a calibrated XUV diode (IRD inc.) can be moved into the beam for energy calibration. This can be done with a filter combination of 400 nm Zr and Al (see Fig. 18) so that only wavelengths between 17.06 and 18.14 nm can be observed which includes parts of the 43^{rd}, the $45^{th}$and the 47^{th}harmonic for a 800 nm driver laser amplifier. First, a spectrum with these filters is taken, followed by the measurement of the absolute intensity with the diode behind the filters. With the spectral picture, the harmonics included in the filter window can be weighted and therefore the measured intensity can be allocated to the harmonics. This offers the possibility to absolutely calibrate the spectrometer. The count numbers of the CCD can be converted to absolute intensities.
The filter chamber is subsequently followed by an entrance slit defining the point source of the XUV radiation. The slit is a high precision monochromator slit (ADC USA Inc.) and all four blades can be controlled separately. The source point defined by the slit is imaged and spectrally dispersed by one out of three different grazing incidence flat-field gratings (Hitachi High Technologies America, Inc.) [120, 121]. The distinctive feature of these gratings is its concave shape and the varying line spacing. The latter feature leads to a flat focal plane instead of fol-

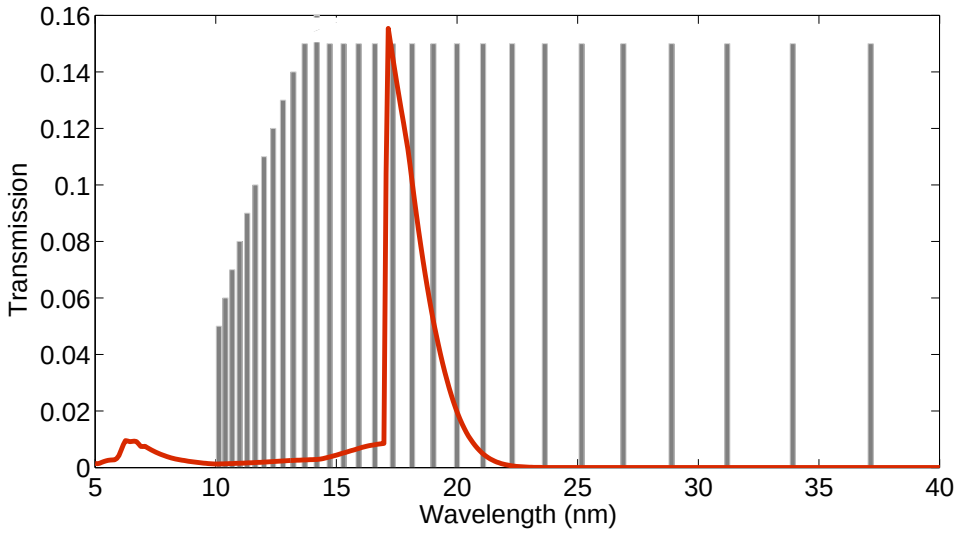

Figure 18: Transmission curve of a combined 400 nm Zr and 400 nm Al foil. The background shows a schematic of a HHG spectrum with a 800 nm driver.

	Grating 1	Grating 2	Grating 3
Grooves per mm	2400	1200	1200
Radius (mm)	15920	5649	5649
Blaze WL (nm)	1.5	10	16
Blaze angle (deg)	1.9	3.2	3.7
Angle of inc. (deg)	88.7	87	85.3
WL range (nm)	1-5	5-20	11-62
SL-grating (mm)	237	237	350
Grating-FP (mm)	235.3	235.3	469
Material	Pyrex	Pyrex	Pyrex

Table 1: Gratings used in the XUV spectrometer setup (WL: wavelength, SL: slit, FP: focal plane). Data from Hitachi High Technologies America (Inc.).

lowing a Rowland circle[5]. The curved shape of the grating enables focusing in the dispersive plane. Three different gratings are necessary in order to cover the complete wavelength range. The parameters of the gratings are listed in Table 1. The grating holder is motorized so that it can be switched between the gratings without the need to access the tunnel. The motors are remotely controlled. To meet the different distances required between the slit and the grating, the grating chamber sits on rails so that the position of the grating can be changed with respect to the entrance slit. As mentioned before, the concave Hitachi gratings only focus the spectral plane, whereas the spatial plane remains unfocused.
The dispersed radiation is focused on a XUV CCD (Princeton Instruments PIXIS-XO with 1024x1024 pixels and 13x13 μm pixel size), which needs to be exactly at the position of the focal plane of the specific grating. Because this distance is different for varying gratings, the CCD can be remotely moved by maintaining the angle of the camera device. In addition to this longitudinal movement, a transverse translation is also possible to scan over the complete wavelength range of a distinct grating.
In addition to the spectral analysis of the seed beam, the spectrometer can help to determine the source size and divergence of the XUV radiation. In our design it is possible to move the CCD into the HHG beam so that the spacial profile can be directly measured. A knife edge measurement can be performed with help of a high precision slit. For this purpose the slit movement is calibrated so that absolute numbers can be extracted from the encoders. This forms the first beam size measurement, whereas the second one, necessary for the determination of the divergence, is simply the size measured on the CCD with known pixel sizes.

3.4 Seed Requirements at FLASH2

Direct seeding within 10-40 nm puts high demands on the seed source and on the injection scheme. The general aim is to achieve a good contrast between the seed radiation and the spontaneously emitted background from the FEL, which is called the *shot noise*. Highest HHG conversion efficiencies and best coupling between electrons and seed have to be ensured in order to achieve a high contrast. The injection scheme is discussed in section 3.3.2, therefore this section concentrates on the requirements on the XUV source and its driver laser system.
There are two important FEL parameters defining the required input characteristics of the seed: the shot noise power and the FEL bandwidth. The shot noise power determines the required seed power and therefore the laser pulse energy. The SASE FEL bandwidth, however, gives an upper limit for the bandwidth of the seeding radiation resulting in a lower limit for the pulse duration.
Both parameters can be assessed by performing a simple GENESIS simulation [10] for SASE operation. The GENESIS FEL lattice was based on an undulator section consisting of 2 m long undulators with an undulator period of $\lambda_u = 31.4\,mm$ with small quadrupoles in drift spaces of 0.6 m in between them to refocus the electron beam. A Gaussian bunch was used as input electron beam for the simulation. Obviously, this is a simplification, because even with the third harmonic cavities, the bunch will never be perfectly Gaussian. However, the approximation is sufficient for a preliminary estimation of the FEL parameters. The electron beam energy was 1 GeV, the emittance amounted to 1.5 mm mrad and the bunch peak current was 2.5 kA. All

[5]The *Rowland circle* is a circle, which is drawn tangent to the face of concave diffraction gratings at its center. The circle has a diameter equal to the radius of curvature of the grating surface. The detector should be set up on this circle.

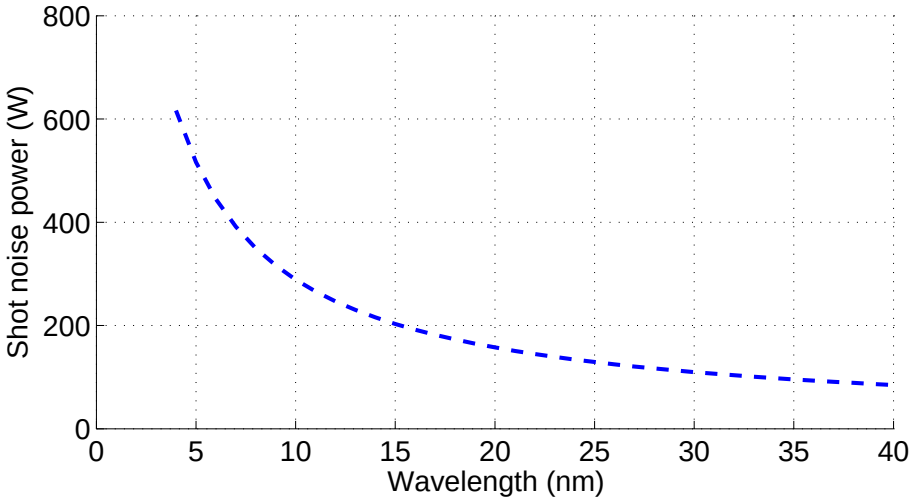

Figure 19: Predicted shot noise power within the start-up of the FLASH2 radiator. The analytical calculation is calibrated with numerical Genesis simulations.

these parameters were chosen to be as close as possible to the expected FLASH2 values [107]. Note, that a start-to-end simulation needs to be carried out for a complete and correct parameter determination. This is beyond the scope of this thesis.

The SASE simulation was carried out at 10.9 and 43.6 nm to have approximately the limits of our wavelength range. The shot noise power could be deduced from the very first periods within the first undulator. This is the actual power competing with the seed power in terms of modulating the electron bunch. The shot noise power for 10.9 and 43.6 nm, which could be extracted from the simulations, served as a calibration of the analytically calculated shot noise power curve in dependency of the wavelength [122, 123]. This is an effective way to predict the shot noise, because the analytical calculation leads to a realistic trend whereas the absolute numbers are set by simulations. The result for a preliminary assessment of the FLASH2 shot noise power is given in Fig. 19. Characteristically, an increasing shot noise level can be observed at shorter wavelengths scaling with $P_{shot} \propto 1/(N_\lambda)^{3/2} \propto 1/(\lambda^{3/2})$ (where N_λ is the number of electrons at a given wavelength). This shot noise is present within the first undulator periods so that the seed radiation needs to exceed this shot noise by at least two orders of magnitude to achieve an adequate energy modulation and therefore a good signal-to-noise ratio. The resulting energy for seed source and driver laser system depends on their pulse durations.

The second important parameter is the FEL bandwidth in order to define a limit for the laser pulse duration. The SASE bandwidth defines the upper limit of the harmonic bandwidth required for the seeding process. Anything higher than that leads to a reduced energy fraction contributing to the bunch modulation. The spectral wings are basically cut away when the harmonic bandwidth exceeds the FEL limit. The FEL SASE bandwidth (RMS) in dependence on the propagation distance through the undulator system for the two simulated wavelengths is given in Fig. 20. The dashed lines indicate the saturation length with 12 m for 43.6 nm and 18.8 m for 10.9 nm. At this distance the FEL bandwidth is 0.5% (0.4%) RMS for 43.6 nm (10.9 nm). As one can see, the bandwidth at the beginning of the FEL is large compared to the value at saturation. It decreases continuously with increasing length. The reason is that the number of charge modulation periods within the bunch increases with growing number of undulator periods passed by the bunch. Increasing number of periods results in an increasing bunch

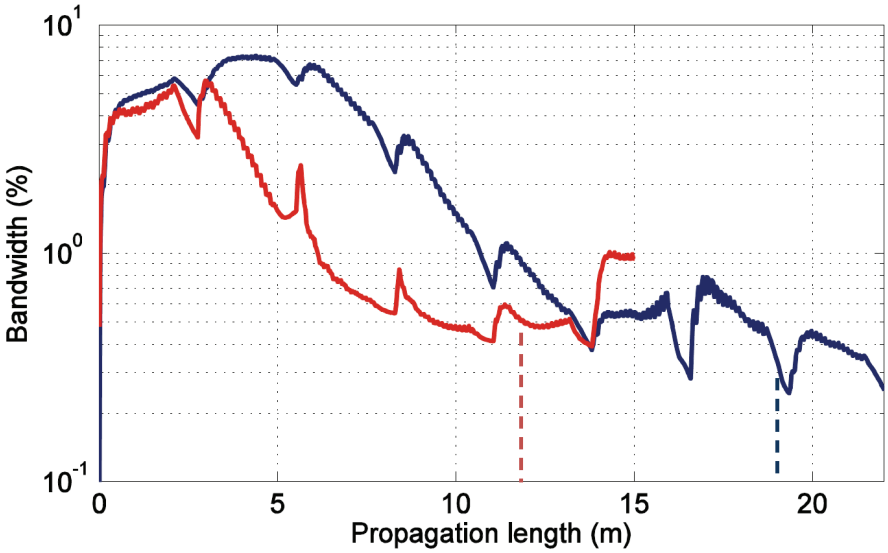

Figure 20: The FEL bandwidth (RMS) in dependence on the propagation distance. The GENESIS simulation has been performed at 43.6 nm (red curve) and 10.9 nm (blue curve). The dashed lines indicate the saturation lengths for these two wavelengths. The dips in the curves are due to drift spaces in between the undulators.

length contributing to the lasing process. Thus, the longer the propagation length the longer the contributing part of the bunch. Characteristically for SASE, the bandwidth stays constant for a certain section at the beginning of the undulator line. Within this section the spontaneous radiation, responsible for the modulation, is produced. In Fig. 20, the modulation becomes significant after 3 m (6 m) for 43.6 nm (10.9 nm). These numbers will decrease for seeding due to immediate presence of the modulating electric field at the entrance of the FEL.
The dips in the plotted curves are at the positions of the drift spaces in between the undulators, equipped with quadrupoles for beam focusing. Only within the undulator sections the FEL radiation can be generated.

4 The new Laser System

The seeding source for FLASH2 has two main components. A driver laser system serves as a front-end of the source. It predefines the pulse length, energy and wavelength range and the shot-to-shot stability. In addition, the repetition rate of the HHG source is equal to the laser repetition rate. The second component is a HHG gas cell, which is used to generate XUV radiation as higher harmonics of the driver laser. The latter component is discussed in detail in the next chapter. The laser system, planned for FLASH2, is described in this section. First experimental results are presented.

4.1 The OPCPA Design for FLASH2

A unique laser system needs to be developed for seeding FLASH2. The required XUV energy, necessary to exceed the FEL shot noise power, results in a lower limit for the laser pulse energy of 2 mJ (a detailed discussion about the demands on the seed source can be found in chapter 5). At the same time, in contrast to proof-of-principle seeding experiments like sFLASH in Hamburg, the laser repetition rate should meet the FEL repetition rate. FLASH2 can be run with 1 MHz burst frequency with 10 Hz bursts. Therefore, the final OPCPA design will incorporate this repetition rate. However, in a first step a 100 kHz intra-burst repetition frequency is chosen for seeding FLASH2. This leads to the possibility to seed a maximum of 80 bunches within a bunch train.
The pulse length required for seeding can be estimated from the FEL bandwidth expected for FLASH2. Hence, the lower limit for the required pulse length for 10.9 nm and 43.6 nm can be determined from Fig. 20. The corresponding FWHM bandwidth values are 0.9% (1.2%) for 10.9 nm (43.6 nm). Assuming a Gaussian pulse shape and Fourier-limited pulses, the lower limit for the seed pulse length can be determined with the time frequency product. Thus, the minimum harmonic pulse durations at FWHM are 1.7 fs (5.4 fs) for 10.9 nm (43.6 nm). The seed pulse length is about half the driver pulse length. Therefore, the laser pulse duration needs to be at least about 4 fs (11 fs) to not exceed the FEL bandwidth. However, the final decision concerning the laser pulse duration depends also on the efficiency of the HHG process. The intensity in the focal spot of the driver needs to be adequate for generating efficient harmonics from 10 to 40 nm. In order to ensure harmonics not exceeding the FEL bandwidth in addition to an adequate focal intensity a pulse length of about 10-15 fs is determined to be the optimum for the driver laser system.
The laser amplifier system is required providing exceptional parameters: mJ-level pulse energy, 10-15 fs pulse duration at 100 kHz (1 MHz) burst repetition rate. A detailed schematic of the planned amplifier system is shown in Fig. 21. A broadband few-cycle Ti:Sapphire oscillator (Rainbow, FEMTOLASERS GmBH) is used to seed both the optical parametric amplifier and the fiber chirped pulse amplification (FCPA) system as front-end of the pump amplification system. The oscillator delivers 2.3 nJ pulses with a 10 dB bandwidth of about 300 nm at a 108 MHz repetition rate. The repetition rate is chosen to be a sub-harmonic of the master clock repetition rate (1.3 GHz) of the FLASH free-electron laser to serve for synchronization to the FEL. This is essential for both the seeding operation and pump-probe experiments. Part of the oscillator output (60%) is used to optically seed an ytterbium-doped fiber amplifier system developed at the University of Jena. The central wavelength of 760 nm is converted to the required 1030 nm by solitonic self-frequency shifting within a photonic crystal fiber (PCF, NL-

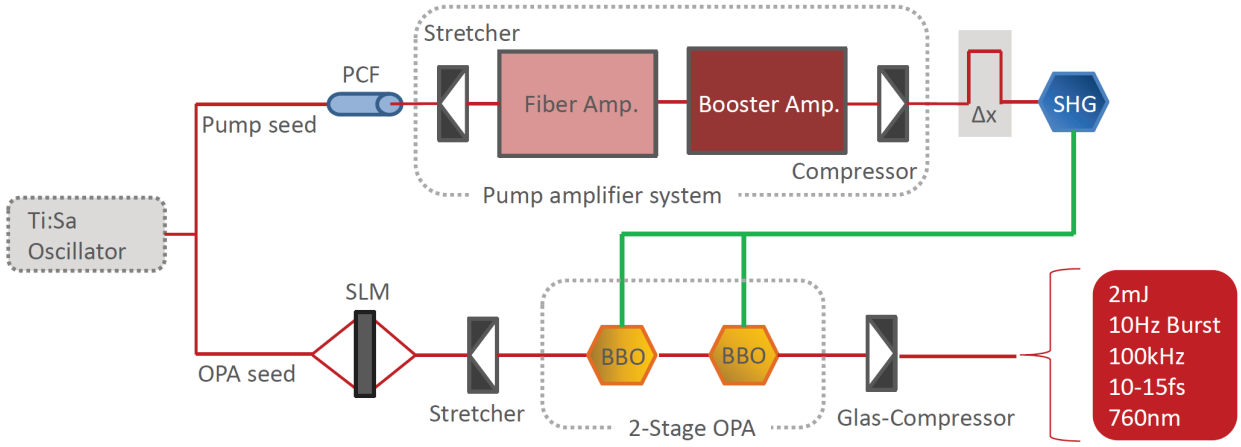

Figure 21: Schematic of the OPCPA setup. A broadband Ti:Sapphire oscillator seeds the OPA pump amplifier and the OPA stage at the same time. For the pump seed a photonic crystal fiber (PCF) shifts the central wavelength from 760 nm to 1030 nm through solitonic self-frequency shifting. Further amplification with a fiber-based amplifier and a booster amplifier generates 20 mJ, 1 ps long pump pulses. After second-harmonic generation (SHG) the pump pulses of about 10 mJ are split into two beams and serve as pump for the two OPA stages. Intrinsic timing drifts within the pump amplifier are corrected by a motorized delay stage. The short OPA seed pulses are stretched to fit to the long pump pulses. A spatial-light modulator is used to control the dispersion. The second OPA stage will produce 2 mJ, 10-15 fs long pulses with a repetition rate of 100 kHz in 10 Hz bursts. The central wavelength is 760 nm.

PM750 Crystal Fiber) [124]. A soliton at 1030 nm with an energy content of about 5 pJ is generated within the 5 nm bandwidth of an interference filter behind the 20 cm long, highly nonlinear photonic crystal fiber. The PCF is followed by a fiber-based CPA system. This generation of amplifier systems is well suited as an OPCPA pump laser [125, 126]. The PCF radiation is first coupled into a 100 m long fiber stretcher and subsequently amplified in the first Yb-doped fiber pre-amplifier up to 250 mW average power at 108 MHz. A repetition rate of 2 MHz is picked by an acousto-optic modulator (AOM). The AOM uses the acousto-optical effect in a transparent crystal. A piezoelectric transducer attached to the crystal generates a sound wave coupled into the crystal. The sound wave changes the refractive index periodically with the period of the sound wave. This generates a grating of varying refractive index causing Bragg diffraction. Thus, the laser pulse has a slightly different central wavelength and direction of propagation after the passage. Switching on and off, this effect can therefore select the desired pulses to be deflected, whereas the unwanted pulses are transmitted. After the AOM, the pulses are further stretched in a grating stretcher to about 2 ns. The resulting train of pulses is coupled into a second Yb-doped fiber preamplifier followed by another AOM, designed to select the lower repetition rate of 100 kHz. The output power after the AOM is ≈ 4 mW. The 100 kHz pulse train is then fed into a Yb-doped photonic crystal fiber amplifier which is described in detail elsewhere [127]. Main reason for choosing this laser gain material is the availability of high power and high brightness diode lasers with a wavelength of 941 nm for pumping [128]. In front of the second PCF amplifier stage one last AOM selects the 10 Hz burst with a 800 μs burst length. The design goal at the exit of the fiber CPA system is a pulse energy of $>$500 mJ.

The stretched pulses are further amplified by a booster amplifier to achieve pulse energies of $\geq 20\,\mathrm{mJ}$. The pulses are thereafter compressed to below 1 ps duration. The booster amplifier can be either an Innoslab [129, 130] or a thin-disk amplifier [131, 132, 133]. For this purpose, a novel $> 1.5\,\mathrm{kW}$ Innoslab system is under development (AMPHOS GmbH), in parallel to the investigations of the thin-disk amplification technology. Thus, both configurations are subject to detailed studies currently performed at DESY and no final decision has yet been made. The 20 mJ infrared pulses are frequency-doubled. The second harmonic at 515 nm is used to pump the OPCPA system. Assuming a conversion efficiency of 50%, 10 mJ pulses can be expected to pump the OPA. By splitting the pump beam, two OPA stages can be pumped in parallel (see Fig. 21).
The other 40% of the Ti:Sapphire pulses are used to seed the non-collinear optical parametric amplifier stages. To prepare the seed for the amplification process, pulse stretching is required in order to match the temporal pump pulse gain window. The stretching is carried out by chirped mirrors. These mirrors have a wavelength-dependent penetration depth and reflection leads to either compression or stretching of the pulse. The remaining dispersion is compensated by a spatial light modulator (SLM) in 4-f geometry. It is used for adaptive control of the spectral phase [134]. The characteristics of the chirped mirrors are chosen to obtain a net negative dispersion of second and third order, to be used in combination with a simple alignment-free glass compressor for final compression. Two OPA amplification stages are implemented in the design setup instead of a single one to achieve high gain, good pump to signal conversion efficiency and high beam quality at the same time [135]. A high stability can be expected at saturation. By optimizing the OPA conversion efficiency the seed beam can become narrower than the pump diameter. In this case, distortions of the beam profile can be observed. The origin of this effect is due to non-uniform signal conversion. In the center, backconversion to the pump can start, whereas the side wings are still converted to the signal and idler. This behaviour reduces the beam quality. To avoid these effects the pump beam needs to be narrow. To not be limited in peak power due to the high intensities as a result of the narrow pump beam diameter, two OPA stages are used in the setup. The first stage is pumped with only 1 mJ out of the 10 mJ expected from the present pump amplifier. The second stage, however, is seeded with the OPA light from the first stage and pumped with 9 mJ pulses. After compression with a fused silica glass compressor, pulses of $\approx$2 mJ pulse energy, 10-15 fs duration and 100 kHz repetition rate at a burst rate of 10 Hz can be applied to drive the HHG seeding source.
High demands on the stability need to be fulfilled, in order to use the OPCPA system for seeding FLASH2. The slow temporal drift between the OPA pump and seed beam can be measured and controlled with a balanced cross correlator connected to a motorized delay stage [136]. A small fraction of the Ti:Sapphire output is correlated with the pulses from the CPA pump system. This opto-electronic technique can detect slightest timing drifts and the compensation is done by a delay stage manipulating the timing relation to the OPA seed pulses. The spatial stability, however, can be ensured by implementing automatized pointing corrections. This can be done with motorized mirror holders. Instabilities in the pulse energy of the OPCPA system is mainly introduced by the PCF used to convert the oscillator wavelength to the pump regime of 1030 nm. To avoid these instabilities direct seeding of the pump amplifier with a separate oscillator is currently under discussion. However, a totally stabilized system is not achievable due to fluctuations caused by the lack of saturation in some parts of the amplifier chain.

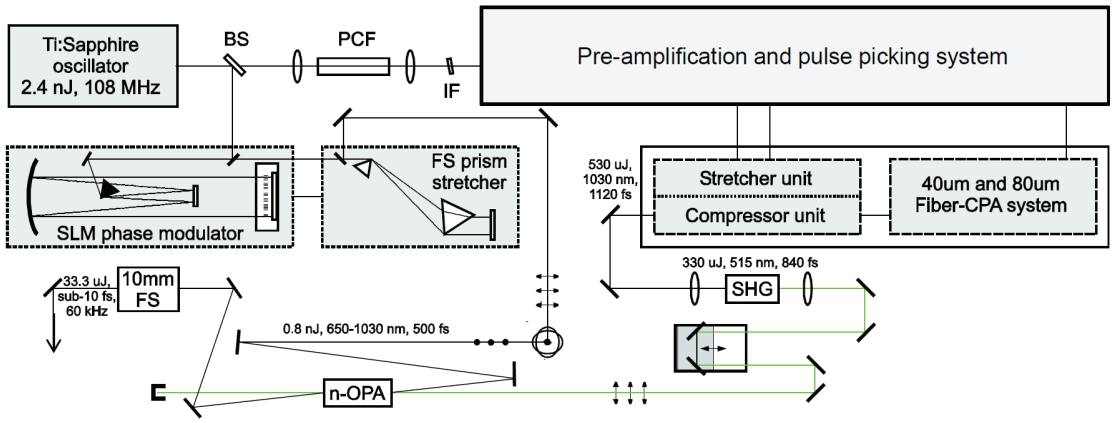

Figure 22: Schematic experimental setup of the prototype OPCPA system including Ti:Sapphire oscillator, fiber preamplifiers, high power fiber CPA system, pulse shaper, prism stretcher, optical parametric amplifier and fused silica bulk compressor. (SHG - second harmonic generation, OPA - optical parametric amplifier, PCF - photonic crystal fiber, FS - fused silica, BS - beam splitter, IF - interference filter, SLM - spatial light modulator)

4.2 Results and Discussion

The OPCPA system proposed for FLASH2 is already in an advanced state of development. In the last three years, first experiments were performed to demonstrate the feasibility of the system for either seeding or pump-probe configurations. In this section, the results obtained with a prototype of the fiber-based CPA pump system are presented. In addition, the present state is described with recently achieved design parameters. The ongoing investigations of possible booster amplifier schemes will not be explained in detail, because the development of a booster pump amplifier is beyond the scope of this thesis.

4.2.1 The Prototype OPCPA Experiment

The prototype setup is shown in Fig. 22. Compared to the design setup of the OPCPA system (compare Fig. 21) the most obvious difference is the lack of a booster amplifier connected to the fiber CPA. The goal of this experiment was to perform first characterizations with the prototype pump amplifier developed at the Institute of Applied Physics in Jena. The booster was not developed at this stage. The Ti:Sapphire oscillator seeded both the fiber-pump amplifier and the OPA stage. The 1030 nm from the PCF was coupled into the fiber stretcher, before a pockels cell selected the repetition rate from 108 MHz to 1 MHz. A pockels cell is an instrument similar to an AOM. However, instead of periodically changing the refractive index the Pockels cell changes the electric field polarization direction. By applying a high voltage to the Pockels cell, the polarization can be rotated. Inserting a polarizer in front and behind the Pockels cell, rotated by 90° with respect to each other, only the pulses with 90° changed polarization direction can pass. Within the prototype setup a Pockels cell was used as first pulse picker instead of an AOM, because of the fast switching time. In a later stage of development the Pockels cell was not necessary anymore due to a changed pulse picking scheme.

The first experiment was performed with a repetition rate of 60 kHz in quasi-cw mode (e.g. no burst was implemented). The design goal of $>500\,\mu$J compressed pump pulse energy (530 μJ)

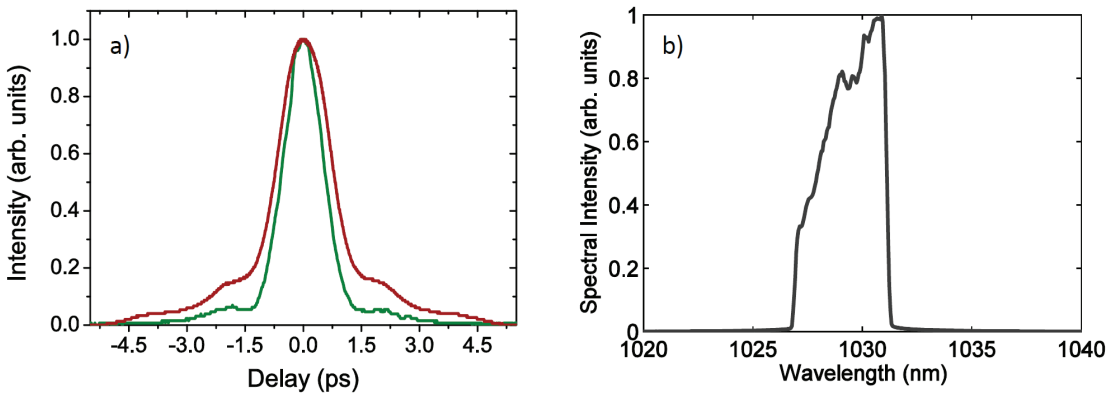

Figure 23: a) Pulse duration of the amplified fundamental pump amplifier pulses (red) and pulse length measurement of the second harmonic (green) measured with an autocorrelator. b) Spectrum of the pump radiation measured at the exit of the compressor. The central wavelength of 1029.5 nm is within the gain regime of the Yb-based amplifier.

was reached at the 60 kHz repetition rate attaining 32 W of average power. In addition, the required pulse length of 1 ps could be achieved with a measured duration of 1.1 ps (FWHM). The pulse spectrum and the measured output pulse duration are shown in Fig. 23a and b. The spectrum is centered at 1029.5 nm. The pump radiation was then frequency doubled in a 1 mm type I BBO crystal with an efficiency of 62%. This output was used to pump the OPA stage. The pulse duration of the second harmonic was 840 fs (FWHM, Fig. 23a). The resulting pump pulses had a central wavelength of 515 nm and a pulse energy of 330 μJ resulting in an average power of 20 W.

The OPA seed was prepared for the amplification process within a prism stretcher. A SLM setup was used in combination with the prism stretcher to maximize the transmission through the shaping and stretcher setup ($\eta_{stretcher+SLM} \approx 50\%$). The prism separation was configured in order to obtain a net negative dispersion of second, third and fourth order, so that a glass compressor could be used for final compression. The seed pulses were stretched to 520 fs (FWHM) to match the temporal pump pulse gain window. In addition, it was already set up in a way to compensate for the compression in the 4 mm BBO crystal (OPA stage) down to 300 fs (FWHM). The compression is an effect of the positive dispersion in the BBO on the negatively chirped pulses. The remaining dispersion was compensated in a 10 mm simple fused silica high throughput compressor ($\eta_{compressor} = 95\%$) and by the SLM up to the sixth dispersion order.

The OPA BBO crystal was set up with a phase matching angle of 23.8°. The non-collinear angle between pump and seed was 2.2° within the crystal. These values were determined to amplify a large bandwidth within the 4 mm thick type I BBO crystal. The pump beam size was reduced down to a diameter of 0.9 mm resulting in a pump intensity of $\approx 100\,\mathrm{GW/cm^2}$. The seed was imaged to a spot size of 0.75 mm. The expected OPA gain was on the order of $> 10^4$.

The amplified OPCPA signal was carefully characterized in order to demonstrate the feasibility of such a system. The measured spectral shape can be seen in Fig. 24a. For a comparison, the spectrum of the Ti:Sapphire oscillator is also shown in the figure. The complete broadband oscillator spectrum was preserved and amplified within the matching angle of the BBO. This opened the possibility to compress the pulses to sub-10 fs pulse duration. The stretched 0.5 nJ seed pulse energy was amplified by the OPA stage to 35 μJ, which corresponds to 2.3 W average

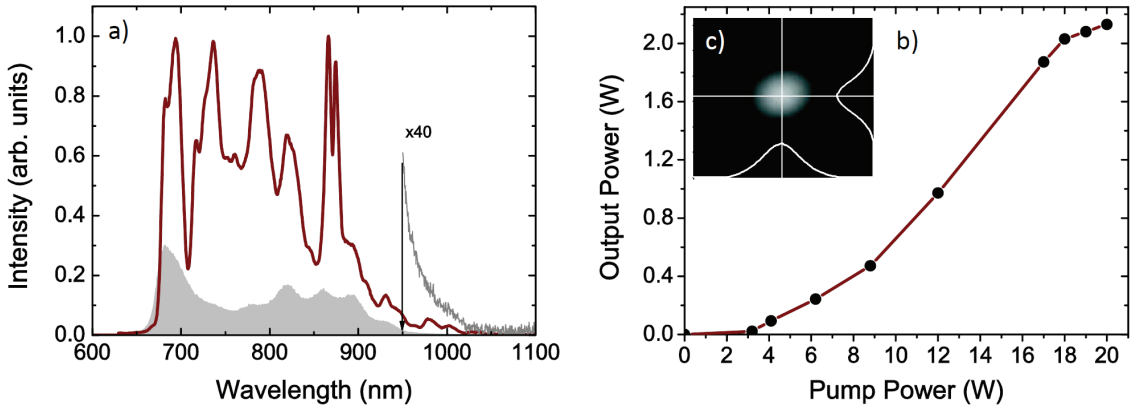

Figure 24: a) Spectrum of the amplified OPA radiation (solid line) compared to the original oscillator spectrum (shaded grey and enlarged solid line - x40 for 950-1100nm). The oscillator spectrum is shown for comparison of the two bandwidths. b) Output power of the OPA stage in dependence on the pump power. c) Beam profile of the amplified OPA signal.

power. The experimental gain was therefore about 10^4, which was well within expectations.
The degree of amplification depends on the pump intensity in the BBO. The amplified signal power versus the pump power is presented in Fig. 24b. It shows the characteristical exponential behaviour of the parametric process. The maximum average power extraction was reached at the saturation point of the OPA stage. Within this saturation regime, an improved signal stability can be expected [137]. However, the general energy stability still depends on the energy fluctuations of the pump pulses.
The level of amplified optical parametric fluorescence (OPF) as spontaneous radiation was 30 mW. This contribution was measured by blocking the seed beam and measuring the OPF content behind a 3 mm aperture. The aperture was positioned at 1 m distance from the OPA stage. However, the effective OPF, which was present in an area which equals the diameter (FWHM) of the seed beam, was smaller by more than one order of magnitude. When the seed beam was present, the contrast between spontaneous and amplified signal was even further improved. On the one hand, the OPF and the signal beam have a different divergence. On the other hand, an OPF quenching effect is expected if the signal beam is present and amplified. The latter effect can be easily observed. As soon as temporal and spatial overlap between pump and seed is achieved, the fluorescence signal almost disappears and only the amplified signal spot can be observed. The OPF reduction could be estimated by numerical simulations [20]. The numerical calculation was performed by F. Tavella, he predicted a quenching factor of 3. Hence, with the reduction to the seed diameter and with the quenching factor, the measured OPF of 30 mW reduced to a value of smaller than 1 mW in presence of the seed beam.
At the saturation level of the OPA stage, conversion to the second harmonic of the seed was also observed. Measurements showed that 10% of the signal output was converted, leaving a total amplified signal average output power of 2.07 W or $\approx 35\,\mu$J pulse energy. The beam profile of the amplified signal is shown in the inset of Fig. 24b.
So far, pulses of 35 μJ pulse energy, 60 kHz repetition rate and a central wavelength of 760 nm were measured as OPA output. The last important parameter to be optimized was the pulse length or compressibility. The pulse duration measurement in this regime of amplification turned out to be challenging due to the large amount of second harmonic light present in the

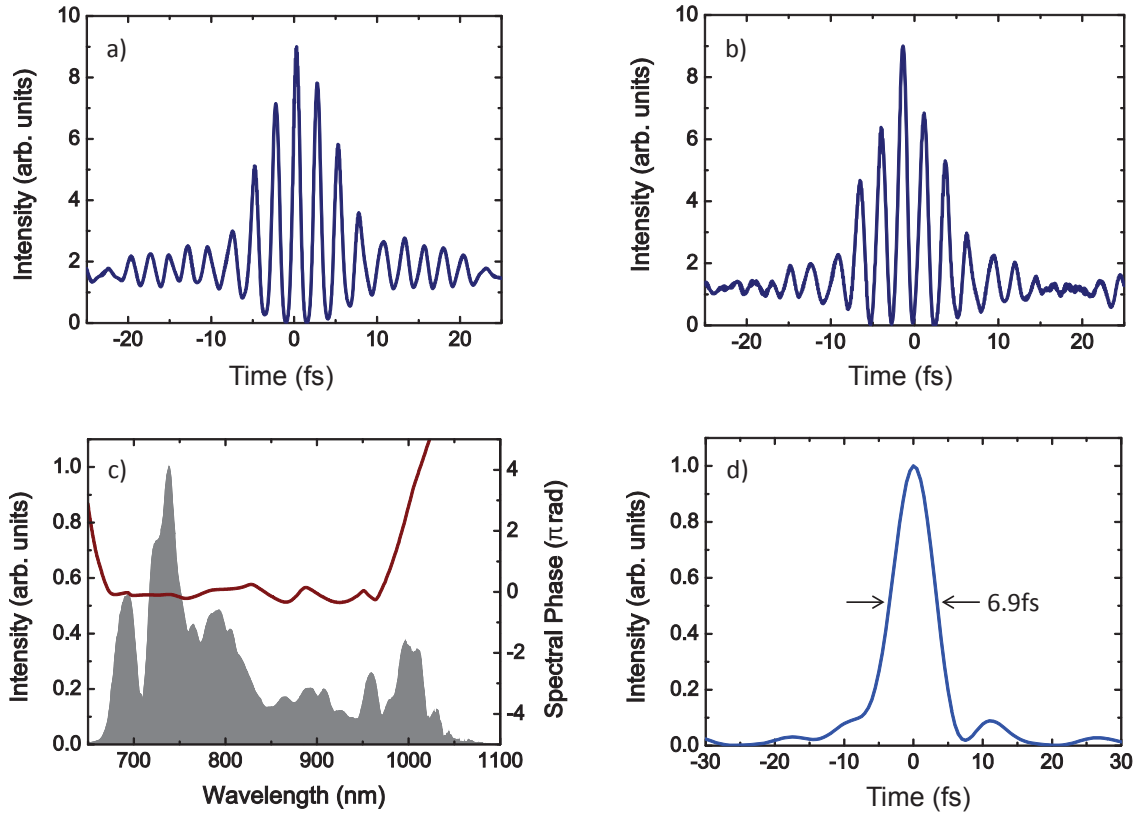

Figure 25: a) Interferometric autocorrelation trace of the 35 μJ pulse. The corresponding pulse length is 7.8 fs (FWHM). b) Interferometric autocorrelation (IAC) for the 20 μJ pulse (black line). The pulse duration is 7 fs (FWHM). c) Spectral phase derived from SPIDER measurement with the amplified spectrum for the 20 μJ pulse. d) The reconstructed temporal profile shows a pulse duration of 6.9 fs (FWHM).

signal. A second order autocorrelation measurement was performed with a commercial autocorrelator (Femtometer, FEMTOLASERS GmbH). The measurement was done at the end of the amplifier chain after final compression. The interferometric correlation trace showed a compressed pulse duration of 7.8 fs at FWHM attaining a pulse peak power of 3.4 GW by estimating the energy content within the FWHM duration. The corresponding interferometric measurement is shown in Fig. 25a. For a second measurement, the gain was reduced by a factor of about 2 to partly avoid generation of the second harmonic of the signal beam. This resulted in an output power of 1.2 W and therefore an energy of 20 μJ. The reduction enabled a more accurate pulse duration measurements to be performed. The compressed pulse duration for these parameters was measured again by autocorrelation and was 7 fs (FWHM, see Fig. 25b). To confirm the measurement done with autocorrelation, a SPIDER (SPectral Interferometry for Direct E-field Reconstruction) measurement was performed. The SPIDER measurement demonstrated a pulse duration of 6.9 fs (FWHM), which agreed well with the autocorrelation value. It was possible to extract the actual spectral phase of the measured pulses using SPIDER [138, 139] (Fig. 25c). The measurement showed a basically flat phase for the complete amplified spec-

trum. The reconstructed temporal profile retrieved from the spectral phase of the OPA pulse is shown in Fig. 25d and the duration at full width and half maximum is 6.9 fs.
The measured 6.9 fs left still some room for improvements. The Fourier limited pulse duration estimated from the measured spectrum amounted to ≈ 6 fs. The key to approach the Fourier limit is the dispersion management in the system. The interplay between SLM, prism stretcher and glass compressor needed to be carefully adjusted.
For 20 μJ signal energy the amount of amplified optical parametric fluorescence was substantially lower than for 35 μJ and thus the average power stability of the OPCPA was 1.3% RMS. The pulse stability was measured in unit of power with an acquisition rate of 4 kHz.
A second experiment with the prototype system was performed. Within this test, a second OPA stage was implemented and the repetition rate was increased to 96 kHz. The objective was to demonstrate the two-stage OPA scheme with a repetition rate close to the design intra-burst frequency. With the changes in the setup a final pulse energy of 70 μJ could be achieved resulting in an average power of 6.7 W. The pulse duration was as short as 8 fs (FWHM) leading to a pulse peak power of 6 GW. At the time of publication, these achievements represented the upper limit in power for few-cycle lasers. S. Hädrich et al. [140] recently demonstrated even 4.8 fs pulses with a similar system. The pulse-to-pulse fluctuations of the amplified pulses were only 5% (peak to peak). These achievements are of high interest, because it increases the applicability of such an OPCPA system. For pump-probe experiments, for example, short pulse lengths are required.

4.2.2 Present State of the OPCPA System

Since the first measurements with the prototype of the OPCPA system (Fig. 21), further developments are continuing. An upgraded version of the fiber CPA pump amplifier has been installed at DESY. The current design of the fiber system is identical to what was planned for the final setup of the OPCPA (see Fig. 26). The Pockels cell was replaced by an AOM and the fiber rods of the main PCF amplifier are water-cooled, leading to a higher stability and output power. The amplification chain was optimized for operation at 100 kHz within 10 Hz bursts. The specifications of the final fiber CPA setup are well within the design parameters. The first fiber pre-amplifier delivers an average power of 1.9 mW. The following AOM reduces the initial 108 MHz to 2 MHz leading to a pulse energy of 0.95 nJ. The pulses are then stretched to 2.3 ns. The stretched pulses are further amplified in a fiber pre-amplifier to an average power of 4.7 mW. The following AOM reduces the pulse repetition rate to 100 kHz so that the pulse energy is 47 nJ. The next element in the chain is the first main amplifier consisting of the PCF with a large-mode area (LMA) diameter of 40 μm. The output power of the first main amplifier is 2 W. With the 100 kHz repetition rate this lead to a pulse energy of 20 μJ. Before the pulses are coupled into the second main amplifier with a LMA diameter of 80 μm, a third AOM selects the 10 Hz bursts from the quasi-cw 100 kHz pulse train. For 50 W output power, the final pulse energy is 500 μJ with a repetition rate of 100 kHz within 10 Hz bursts. The fiber output can be compressed to a pulse duration of 850 fs (FWHM). A typical 100 kHz burst, consisting of 80 pulses measured after the amplifier chain of the pump system, is presented in Fig. 27. The pulses are equally strong within the burst so that stable seeding becomes possible within a bunch train of the FEL.

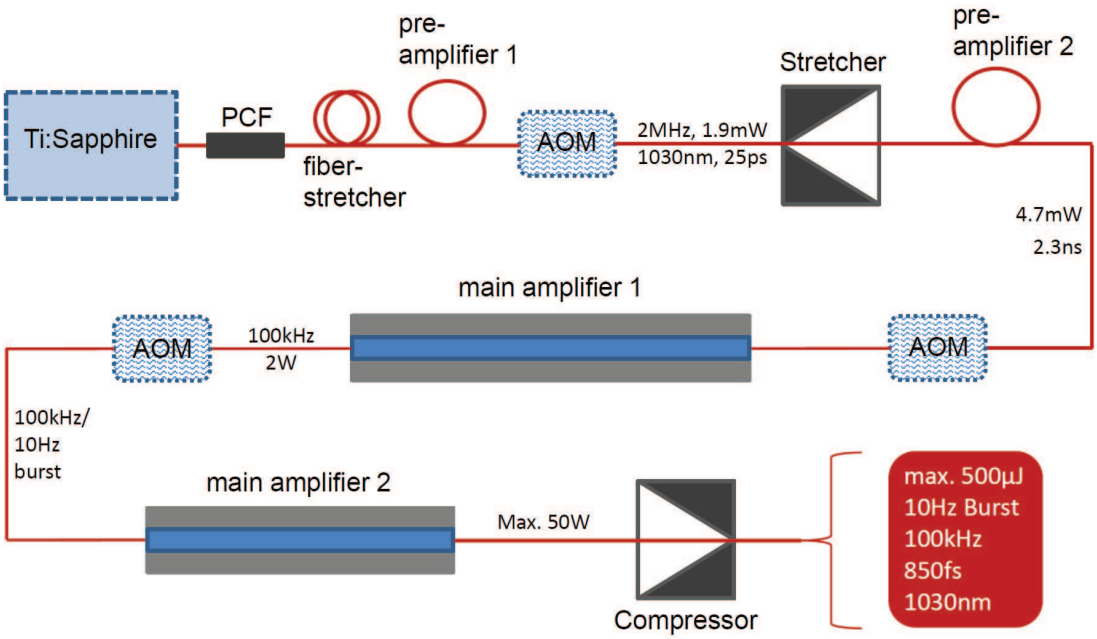

Figure 26: a) The fiber CPA amplifier system. The Ti:Sapphire seed experiences stretching and pre-amplification before an AOM selects 2 MHz out of 108 MHz repetition rate. After the main stretcher a second pre-amplification prepares the pulses for the first main amplifier, where an output of 2 W can be expected. The second main amplifier amplifies the pulses to the final 50 W average power, before a grating compressor can compress the pulses to sub-ps pulse duration.

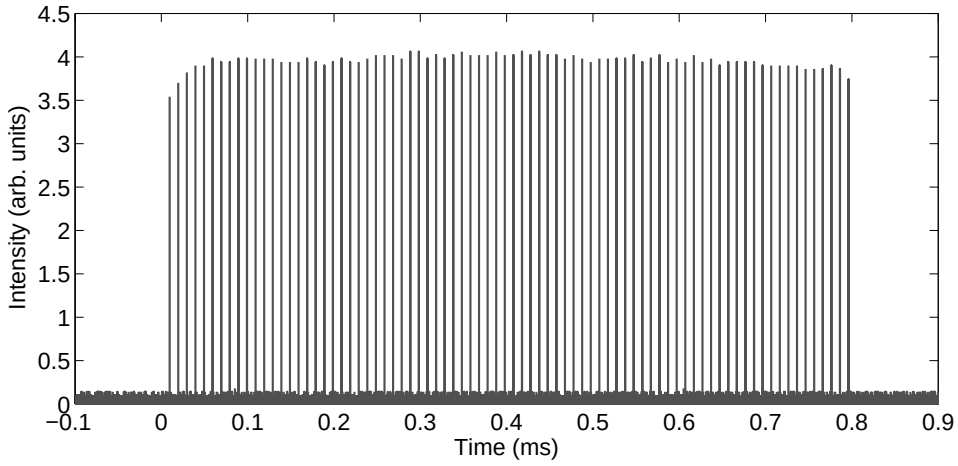

Figure 27: Typical burst of the pump amplifier system. One burst consists of 80 pulses with a repetition rate of 100 kHz. The burst repetition rate is 10 Hz.

The design pump energy of 20 mJ can only be achieved with a further booster amplifier following the fiber-CPA system. Two variations are currently under investigation. Firstly, a thin-disk amplifier as pump-booster in a multipass configuration can lead to sufficient energy [131]. Secondly, a Innoslab amplifier can be a more compact solution [129]. For further amplification in the booster amplifier, the pulses from the FCPA are left uncompressed. Thus, the pulses are fed into the booster, and after amplification, the pulses are coupled into the compressor of the fiber

system for final compression.
Preliminary tests were performed with both configurations and the investigations are still ongoing. A final decision whether a thin-disk or Innoslab amplifier will be used as a booster has not yet been made. A detailed discussion about the two opportunities is beyond the scope of this thesis but will be subject of a future PhD thesis by Michael Schulz[6].
The first successful tests in Jena and the implementation of the system at DESY demonstrate that the final OPCPA setup planned for FLASH2 is, in principle, feasible. The next steps in the laser development will be the implementation of the $>1.5\,\mathrm{kW}$ Innoslab amplifier and detailed investigations into the OPA setup. In parallel, methods to increase the overall stability of the OPCPA systems are under development. The objective is to develop an amplifier system which not only delivers the required specification concerning pulse duration, energy and repetition rate but also fulfill the high demands of a user facility like FLASH. The systems needs to be easily operated and stable for at east one user shift of 8 hours.

[6]Michael Schulz, DESY Hamburg, mi.schulz@desy.de

5 The novel XUV Source

To convert the infrared, femtosecond laser pulses of the OPCPA driver system to ultraviolet (UV) and extreme ultraviolet (XUV) pulses, the process of high harmonic generation (HHG) in noble gases is commonly considered to be an adequate solution especially in the case of FEL seeding [5]. However, the seeding process in a wavelength range from 10 to 40 nm is very demanding due to the direct influence of the seed pulse characteristics on the FEL process itself. The development of a HHG source is therefore a major concern for the seeding project at FLASH2. This development forms the main subject of this thesis. The first section deals with the general and special seeding requirements, which set basic demands on the HHG source used as a XUV seeding source. The new QPM concept developed within the PhD work is presented in the next section, followed by the results of several experiments performed with the novel dual-gas HHG scheme.

5.1 HHG for Seeding

HHG sources used for FEL seeding need to fulfill strict requirements concerning harmonic energy, bandwidth, divergence, pulse length, energy and pointing stability, as well as spatial and temporal pulse structure [115, 141]. In the following all these requirements, necessary in order to develop a new HHG scheme, are discussed.

Harmonic energy

The harmonic energy is directly connected to the harmonic conversion efficiency and is one of the major concerns of the source development. As discussed in chapter 3, the shot noise is the starting-process of SASE in a FEL (see Fig. 19). This spontaneous radiation is always present as soon as electrons experience deflection in the undulator. Therefore, the seed pulse energy needs to overcome the shot noise energy within the FEL starting-process for a good contrast between SASE and seeded radiation by at least two orders of magnitude within the interaction length. In general, the interaction length is given by the pulse duration of the seed pulses. However, the available diagnostics will not allow a temporally resolved analysis of the seeded FEL radiation and thus the measured intensity will always be the temporally integrated signal. Therefore, the shot noise energy over the complete bunch length needs to be taken into account. It can be determined using the shot noise power from Fig. 19 and assuming an effective bunch length of 200 fs (FWHM). Transmission losses due to mirrors included in the beam line need to be considered for a calculation of the required seed energy at the position of the source. In addition, the factor of 100 needs to be included in the calculation, as previously discussed in connection with a good contrast between spontaneous and stimulated FEL radiation. With these assumptions, the required energy at the position of the source can be determined directly from the shot noise power within the undulator (Fig. 28). This energy forms the lower limit for the harmonic source energy for seeding FLASH2.
Different approaches can be found in the literature to enhance the harmonic conversion efficiencies, thus overcoming the shot noise limit. In Fig. 28, the most common values of harmonic conversion efficiencies have been used to calculate the expected harmonic energies by assuming 2 mJ of laser energy from the OPCPA. It is obvious, that long jet or loose focusing geometries driven by 800 nm laser systems are only adequate for low, absorption limited harmonics as has

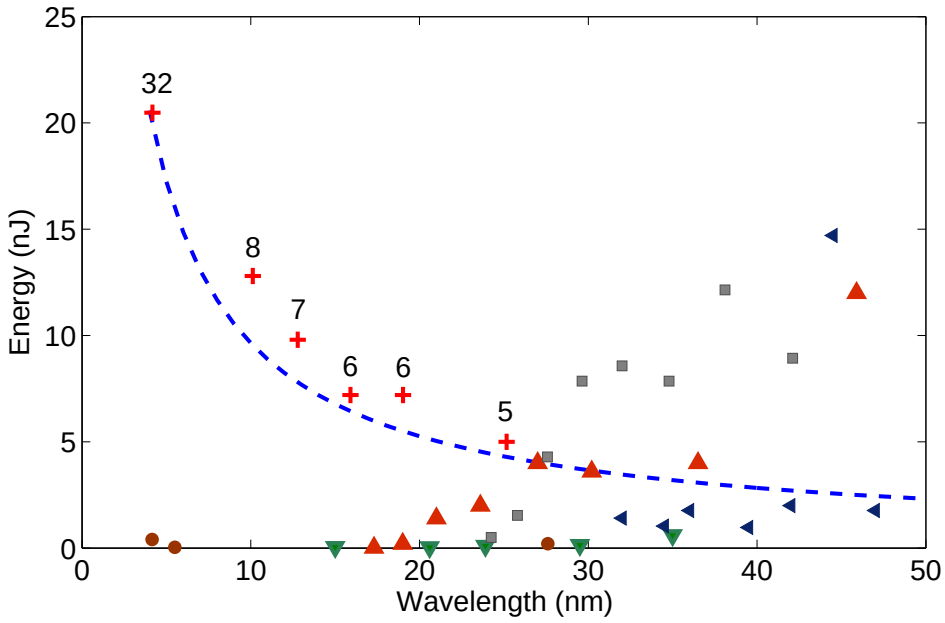

Figure 28: Energy requirement on the source and available HHG schemes with their corresponding highest reported conversion efficiencies applied to a driver laser pulse energy of 2 mJ. The required harmonic energy at the position of the source (dashed blue line) is calculated for the complete electron bunch (200 fs duration at FWHM). It becomes obvious that in the wavelength regime above 28 nm, conventional HHG sources using long jets, the second harmonic or two-colour mixing will lead to sufficient energy (grey squares: long jet/long pulse [141]; blue tilted triangles: two-colour mixing (800/400 nm) [142]; green (red) triangles: single jet 800 nm (400 nm) [144]; brown circles: multimode QPM [77, 78]). Below 28 nm the conversion efficiency of HHG with conventional sources decreases. QPM can exceed the required energy level by achieving full $(N_{QPM})^2$-enhancement (red crosses with numbers indicating the QPM periods).

been discussed in detail in a recent publication by Erny et al. [141]. Their results have been achieved with a jet interaction length of 20 mm using argon as a driver medium. This is exactly the same HHG scheme as used at sFLASH [53]. A further increase in harmonic energy can be achieved with a shorter driver wavelength (see also Fig. 28). A SHG conversion efficiency of 50% is assumed and sufficiently efficient HHG can be expected for wavelengths down to 27 nm. Additionally, it is possible to mix the fundamental with the second harmonic. As one can see in the plot, two-colour mixing leads to harmonic energies close to the limit of the required source energy in the range between 36 and 47 nm [142]. Very high efficiencies have been reported for orthogonally polarized two-colour laser fields with helium as a driver medium and for wavelengths between 21 and 24 nm [143]. However, the filter transmission stated in the publication relies on very thick oxide layers on the aluminum filters. This seems to result in a tremendous overestimation of the conversion efficiency. The resulting harmonic energies are about 150 nJ at 21.6 nm. Hence, this result is not included in Fig. 28.

In conclusion, for wavelengths in the low-order range (28-40 nm), conventional long jet geometries with a possible usage of the second harmonic as driver or even two-colour mixing could be an adequate solution for seeding FLASH2. However, higher efficiencies are needed

especially in the regime of phase-limited HHG below 20 nm. In this range, QPM with its N_{QPM}^2-dependence on the QPM period N_{QPM} is the most promising approach and estimations of achievable energies for certain numbers for N_{QPM} are plotted in Fig. 28. For wavelengths from 10 to 26 nm a modest conversion efficiency of 10^{-7} is achievable in conventional HHG schemes which can be further enhanced by the QPM effect. For the water window a conventional efficiency of 10^{-8} is assumed, leading to a theoretically required QPM enhancement of about 10^3 achievable with $N_{QPM} = 32$. Hence, only if it is possible to achieve quasi-quadratic signal growth by increasing the number of QPM periods, it becomes possible to improve the HHG performance at wavelengths, where the shot noise level of the FEL increases.

Harmonic bandwidth

The limits given by the FEL gain bandwidth have already been discussed in section 3.4, where with the upper limit of the bandwidth, a lower limit for the driver pulse length has been derived. For multi-cycle laser pulses, as expected from the FLASH2 OPCPA system, bursts of attosecond pulses result from the nonlinear HHG process. This results in a spectrum consisting of a comb of odd harmonics. In principle, the complete HHG spectrum can be sent into the FEL without any prior spectral filtering. Only the harmonic closest to the resonance wavelength of the FEL undulators contribute to the energy modulation of the electron bunches [141]. This is due to the difference in velocity of the electrons and the seed light in forward direction. By passing the undulator structure, the electrons undergo a horizontal oscillation which reduces their forward velocity. Electrons and seed radiation hence experience a slippage with respect to each other. This results in an additional modulation period in the micro-bunching structure after every further undulator period. In the time domain, the size of the energy modulation increases by $T_{mod} = \lambda_r/c$, which results in a spectral narrowing effect. If the resonance wavelength corresponds to the q$^{\text{th}}$order of the HHG spectrum, the attosecond pulses within the train, which forms the time domain representation of the harmonic radiation, begin to overlap after q/2 undulator periods. This leads to the selection of just one single harmonic for the micro-bunching process. The FEL acts therefore as a spectral filter with a maximum bandwidth defined by the FEL gain bandwidth. This is also the reason why only the harmonic energy and not the total XUV pulse energy is important for the FEL process. In general, harmonics with bandwidths lower than the FEL gain bandwidth are desirable. This leads to both a reduced spectral width of the outgoing FEL radiation and full energy content contributing to the micro-bunching process. This can be achieved by ensuring optimized phase matching for the short trajectory contributions. Long trajectory contributions will broaden the harmonic bandwidth and the energy within the spectral wings does not contribute to the seeding process. Under certain circumstances, in which special wavelengths need to be amplified within the FEL, broadening the odd harmonics of a conventional HHG spectrum can increase the tunability of the FEL [67]. A further tool to ensure the wavelength tunability is the application of two-colour mixing to break the symmetry of the harmonic process, which leads to even harmonics in the spectrum [143].
The dependence of the seed pulse length on the energy modulation has been theoretically investigated by Erny et al. [141]. They show that there is an optimum seed pulse length which leads to maximum energy transfer from the seed to the electrons and to a maximum modulation amplitude. For a Fourier-limited pulse it is always valid that a very short pulse must feature a broad spectrum. The shorter the pulse the higher the probability that the gain bandwidth of the FEL is exceeded. This implies again that not the complete energy can be used for modulation.

With increasing pulse length the energy transfer, as well as the modulation amplitude, increases until the pulse length becomes comparable with the slippage length. Further increase of the seed pulse duration will not lead to growth in energy transfer and will even cause a decrease in the energy modulation amplitude. The latter point is easy to understand, knowing that a longer pulse with the same energy content will automatically have a lower field amplitude responsible for the energy modulation. The value for optimum pulse length depends on the undulator parameters and pulse energy. However, the results of Erny et al. [141] show that the optimum pulse length is almost identical for the energy transfer and the modulation amplitude. Therefore, the lower limit derived from the FEL gain bandwidth should be an adequate benchmark.
The optimum pulse length also depends on the pulse length required to achieve sufficiently high intensity in the laser focus. Thus, it is important to balance the two requirements for efficient seeding. Note, that this is a requirement especially valid for FLASH2 seeding with limited driver energy. If the driver laser systems provides high energy pulses (like 15 mJ at sFLASH), the restriction of the pulse length is less crucial.

Harmonic divergence

Seeding do not have any restrictions to the divergence of the seed source as long as the divergence is well known. In that case, the optics can be set up in order to couple the seed beam to the electron beam. The divergence of the harmonic radiation is mainly determined by the source size and the contributions of the two main quantum paths. For optimum seeding conditions with periodic attosecond pulse trains, and therefore a dominant contribution from the short trajectories, a small and well-predictable divergence can be expected. The predictability is due to the quasi-Gaussian wavefront, which is preserved from the laser due to the weak phase dependence on intensity variations for the short trajectories. For long trajectory contributions the divergence is much higher and the strong intensity dependence of the phase will lead to M^2-values of up to 30 [73]. Hence, also in terms of divergence and beam quality, long trajectory contributions should be avoided.

Harmonic stability

The energy stability relies on the laser stability and on the degree of phase matching. Laser intensity variations do have less influence on the harmonics for good phase matched harmonics with a dominating short trajectory contributions. However, the driver laser energy needs to be as stable as possible in order to improve the FEL energy stability being presently 14% (RMS) with SASE operation at FLASH. Beam stabilization systems are under development to minimize pointing drifts in the laser system. Nevertheless, a certain pointing instability can be induced by plasma effects and laser intensity variations during the interaction. This can be reduced by optimizing the process at moderate pressures and interaction lengths.

Harmonic profile
The spatial and temporal structure of the harmonics rely on both contributions of long and short trajectories and on plasma induced effects like plasma defocusing. In general, a long jet will lead to an elongation of short, few-cycle pulses. Thus, HHG schemes which increase the harmonic efficiency without increasing the medium density become highly attractive especially for applications, where a short pulse is required.

From these requirements posed by the FEL seeding process, two main challenges remain for the XUV seed source development. For wavelengths below 28 nm QPM enhancements of up to a factor $8^2 = 64$ are necessary to achieve harmonic energies well above the shot noise energy emitted by the electron bunches. Furthermore, this enhancement process needs to be absolutely controllable and reproducible. Especially the latter demands are the most critical when evaluating the existing QPM schemes. A coherent control of the harmonic process will also guarantee a free choice of the quantum path contributions and therefore efficient control of important source characteristics needed for the seeding process.

5.2 The dual-gas HHG Concept

5.2.1 General Concept

An ideal QPM scheme with driving and matching zones should allow the HHG yield of the source to be limited only by absolute constraints of the medium itself (such as the absorption length and harmonic polarisability of a single atom or ion χ_q). First, the matching half period should be completely passive (no HHG signal should be produced), to allow tunable control of the phase between individual sources at the same time. These features would permit clean trajectory selection and rapid growth of the HHG signal. Second, the matching half period should negligibly absorb both harmonic and laser fields which would counteract the QPM enhancement effect. Furthermore, since the high intensities required for HHG can only be achieved in the Rayleigh length of a laser beam, it is desirable to have the QPM periods as closely spaced as possible, which enables a maximum number of QPM periods within the Rayleigh range. As already discussed in section 2.2.6, for ideal QPM a sharp and strong modulation is required and the effect of absorption and imperfect suppression for QPM schemes that have ideal periodicity of $2L_c$ have been presented in Fig. 11. The reduction in the signal growth due to nonideal modulation depth and absorption can be substantial.
Additionally, high peak power or high average power applications using state-of-the-art lasers, for example the newly developed OPCPA driver system for FLASH2, require an experimental setup free of damage threshold constraints. In general, this is also required under circumstances where the wall load is very high - such as multimode capillaries [78]. Particularly, for FEL seeding with FEL pulse repetition rates of up to 100 kHz, as planned at FLASH2, free-propagation QPM schemes are the only acceptable solution.
QPM can be achieved using for example modulated capillary diameters [75, 76] or the effect of multimode beating in a capillary [77, 78], as well as counterpropagating pulses [79], polarization gating [80], vacuum-shift-based multiple jets [82, 83] or a capillary discharge [84]. All these QPM schemes, while elegant advances in their own right (in particular the use of counterpropagating pulses [79]), fall short of the ideal scenario discussed here, either because the source in the matching half period is only weakly suppressed, the gas in the matching half period adds appreciable absorption and/or because the spacing of multiple jets require distances larger than common Rayleigh lengths. In addition, out of the basic concepts discussed above, free-propagating geometries appear to be the only solution which meets the requirements of high average power applications like seeding and therefore free jets appear to be the best suited as a seeding XUV source at FLASH2.
Multijet arrays have been theoretically investigated [145, 146] and first experiments have been performed using the Gouy phase shift as the matching parameter in vacuum intersections be-

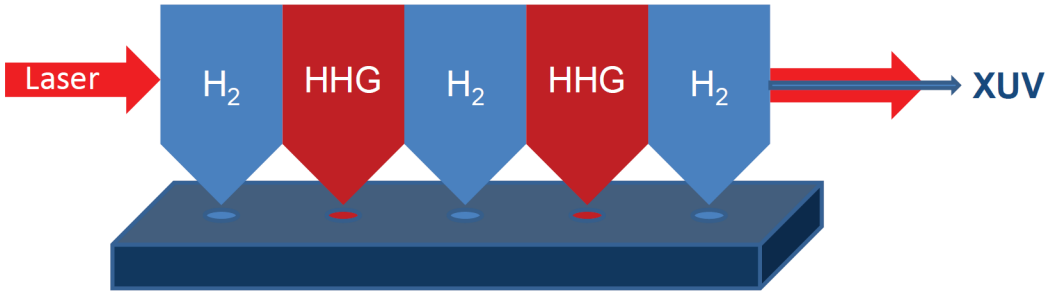

Figure 29: The dual-gas QPM concept with hydrogen acting as a passive phase matching medium and as an enclosing medium, in order to define sharp jet boundaries in the propagation direction.

tween multiple sources [82, 83]. In addition to the possibility of substantial signal gain, the 1D theory predicts a remarkable control of the relative weight of quantum path contributions on-axis. In practice the ionization induced defocussing not included in the original theory complicates the evolution of the relative phase from the idealized vacuum Guoy shift and results in jet separations which are substantial compared to a realistic Rayleigh range of the laser. This implies that it is difficult to use a large number of jets required for high degree of coherent control or substantial signal gain.
In order to meet all requirements stated above, a novel QPM multijet design has been developed within the framework of this PhD, in which a generation medium alternates with hydrogen as passive matching medium (see Fig. 29). The only restriction within dual-gas QPM is that the HHG medium must have a higher ionization potential than hydrogen (e.g. most of the common HHG media such as helium, neon, argon and their ions). If this condition is fulfilled, hydrogen will be fully ionized at the rising edge of the pulse. Since completely ionized hydrogen cannot emit further harmonic photons, the first condition for an ideal QPM scheme is perfectly fulfilled. Neutral and depleted hydrogen have minimal absorption for all wavelengths of interest compared to the HHG media available and therefore the hydrogen half period also fulfills the second condition and only adds a phase dominated by the free electron dispersion given by

$$\phi_q \propto q L_M n_e r_e \lambda, \tag{55}$$

where L_M is the length of the matching half period, n_e the electron density, r_e the classical electron radius and λ the fundamental wavelength. The hydrogen and generation jets are set very close to each other within the array, so that distinct zones with a sharp division are created. This leads to a deeply modulated density, key to ideal QPM enhancements.
In addition, hydrogen jets placed at the beginning and at the end of the jet array will have no effect on the phase matching. Due to the passive nature of fully ionized hydrogen it just acts as a sharp geometrical boundary for the spreading density of the generation medium. With sharply defined jets, an easier interpretation of achieved results becomes possible.
In conclusion, the novel dual-gas QPM scheme combines the theoretical advantages of QPM for achieving high signal levels with a free propagating geometry that is suitable for HHG driven by high power lasers. Dual-gas QPM is in principle compatible for the production of intense harmonic spectra at short wavelengths approaching the *water window* and beyond. Phase-matched operation at such short wavelengths has recently been demonstrated by Popmintchev et al. [32]

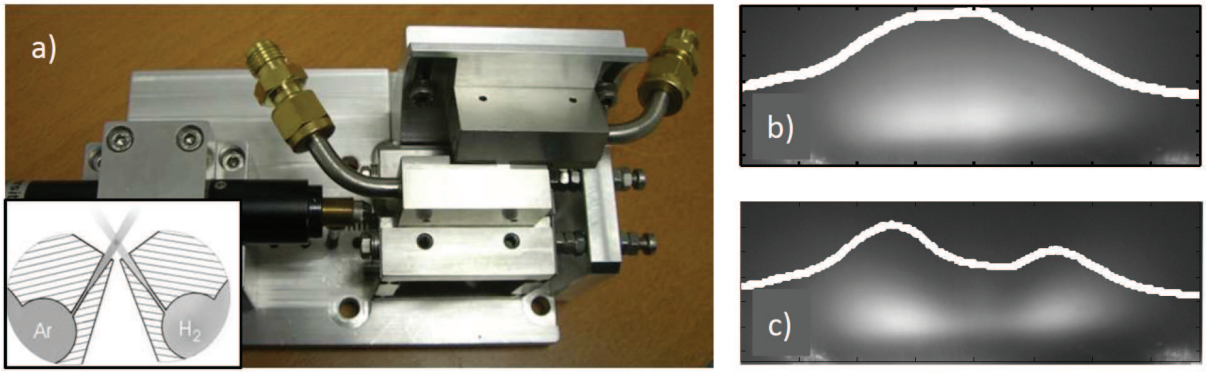

Figure 30: The prototype target. a) Picture (top view) and working principle of the target used at TEI Crete. b) Plasma side image for argon only and c) for argon with one hydrogen intersection.

using very long laser wavelengths where phase matching is easier to achieve at the cost of substantially reduced single atom response ($D_x \propto \lambda_L^{-5}$, see section 2.2). Compared to this approach dual-gas QPM operation has an intrinsic flexibility of being largely independent of the driver wavelength and the medium and may thus allow a strong harmonic response harnessing high power, shorter wavelength driver lasers. The phase introduced by each matching half period would need to be varied freely from one hydrogen zone to the next, in order to achieve ideal performance. This is important because it is very difficult to achieve perfectly uniform conditions over long lengths along a high power laser focus. Especially for very high harmonic orders (e.g. sub-10 nm wavelengths), the laser field will experience subcycle modifications due to nonadiabatic effects in the generation medium [145]. This implies that L_c is not a constant along the propagation path. Thus, the dual-gas QPM scheme should allow for fine tuneability of individual matching sections to ensure that the total phase added by each QPM period corresponds to 2π. This feature will be implemented in future versions of the dual-gas multijet array allowing more than 10 generation jets which can be optimized for the sub-10 nm wavelength range. This will, of course, put high demands on the vacuum pumping system, because in contrast to capillary-based HHG higher backing pressures are needed in a free-jet system for achieving an adequate up-conversion in the short wavelength regime.
Note, that for all wavelengths of interest it needs to be ensured that the absorption length of the HHG systems is larger than the total length of the generation medium within the dual-gas array. Only if this condition is fulfilled, will the QPM effect lead to higher signal gain and efficient control of the quantum path contributions.

5.2.2 The Prototype dual-gas Target

The first prototype jet design, a dual-gas multijet array is shown in Fig. 30a. The jets are formed by electro-eroded de Laval-shaped nozzles with a diameter of 200 μm at the nozzle exit. The separation of the nozzle centers is 430 μm from center to center. The de Laval shape was chosen in order to reduce the spread of the gas after exiting the nozzle and therefore minimize turbulence between neighbouring jets. The nozzle support is conceived in a way that the arrays of argon and hydrogen have a crossing angle of 15°, which leads to a crossing distance to the two nozzle entrances of about 150 μm. The argon array is placed on a solid spring for fine adjustment of the relative position of the two jet assemblies. The distance between driver and matching jet is as small as 230 μm center-to-center so that the QPM period has a total length

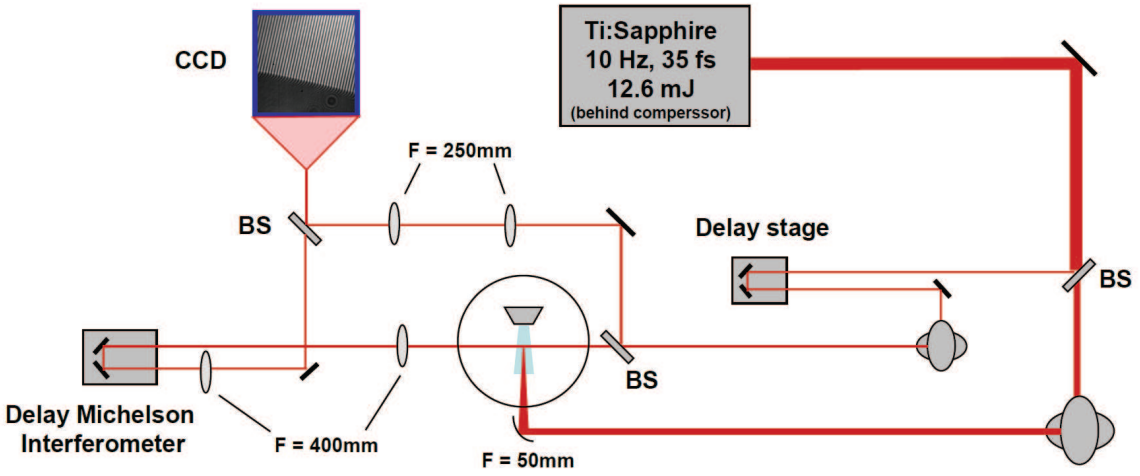

Figure 31: Gas density measurement setup using a Michelson interferometer to detect changes in the refractive index in the gas jet due to ionization (BS: beam splitter).

of 430 μm. The backing pressures in the two arrays are controlled separately with absolute electronic pressure controllers whereas all nozzles of the same array are operated with the same backing pressure. Arrays with either two HHG jets and one matching jet or four HHG jets interspersed with three matching jets are part of the proof-of-principle design.
As already discussed, hydrogen as matching medium does not only add a phase difference between the laser and XUV fields, it also acts as a spacer between the sources which ensures a high modulation amplitude leading to sharp edges of generation and matching zones. Fig. 30 b and c show plasma side images of an array with two generation and one matching zone. In Fig. 30b no hydrogen is used so that the generation jets (e.g. argon in this case) fill the complete interaction area. By adding the hydrogen (Fig. 30c) two distinct generation jets become visible with the weakly emitting hydrogen plasma in between.
In principle, our novel scheme allows the phase introduced by each matching half period to be varied freely from one hydrogen zone to the next. However, the prototype target can not be easily modified. An increased number of separate reservoirs are necessary to fulfill the requirement of individual density control. This is a very complicated task if the micro-nozzles are manufactured with electro-erosion.
During the experiment, only the backing pressure in the reservoir can be measured. This pressure can differ significantly from the actual pressure at the nozzle exit. Gas density measurements were performed in order to determine the real pressure in the interaction zone. For this experiment a single electro-eroded de Laval nozzle with a diameter of 200 μm was used. The density measurement principle relies on the determination of the electron plasma density using Michelson interferometry. Changes of the refractive index due to free electrons in an ionized gas jet are detected as fringe shifts in an interferogram. Further information on this technique can be found elsewhere [147, 148, 149].

For the plasma density determination, a pump probe setup was installed with a pump pulse as ionizer and a probe pulse for imaging the free electron density (see Fig. 31). A 12.6 mJ laser pulse with a pulse duration of 35 fs, a repetition rate of 10 Hz and a central wavelength of 800 nm was split into 8.7 mJ pump and 0.22 mJ probe pulses. The pump beam was focused

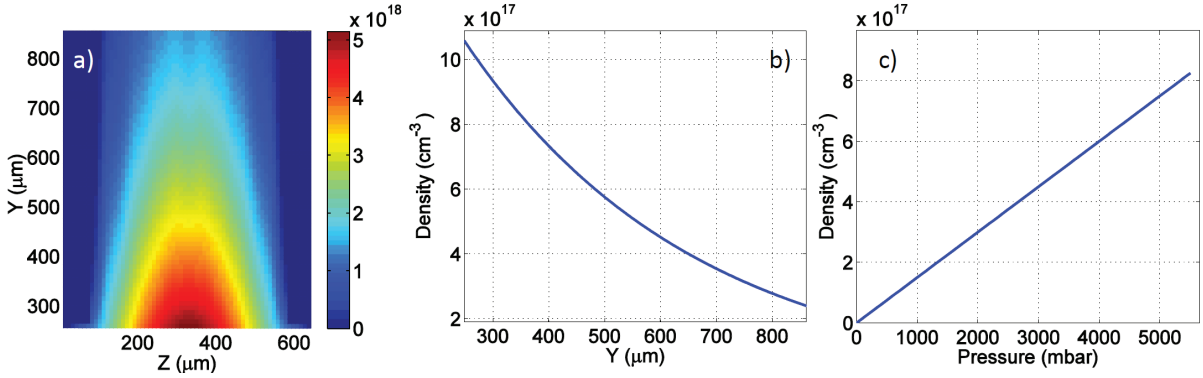

Figure 32: Results of the gas density measurement. a) Electron density map with Z, the longitudinal direction and Y the vertical distance to the nozzle entrance (colour scale in N/cm^{-3}). b) Evolution of the particle density in dependence of Y. The backing pressure is held constant at 6 bar. c) Particle density vs. backing pressure at a constant distance of 455 μm from the nozzle entrance.

with a f = 50 mm focal distance into the argon jet for electron plasma generation. The degree of ionization could be determined by ADK calculations. The probe beam, however, passed a delay stage to vary the temporal delay between the ionization and probing process before splitting into a 0.13 mJ and a 0.06 mJ fraction. One part of the probe beam passed the argon jet orthogonally to the pump beam. The second part bypassed the gas setup. Clear fringes with disturbances due to the plasma were visible on the CCD. The 2d-electron-density map can be deduced from fringe patterns with the scientific software *IDEA* [150]. The electron density map is shown for the single 200 μm nozzle in Fig. 32a. The jet can be characterized measuring the density for different distances from the nozzle exit (see Fig. 32b) and for different backing pressures at constant height (see Fig. 32c). Note, that for these scans the density is already corrected for the ionization fractions. From the pressure scan, the relation

$$N = 1.5 \cdot 10^{14} \cdot P \pm 1.4 \cdot 10^{17} \tag{56}$$

for the backing pressure (P in mbar) dependence on the particle density N in cm^{-3} can be obtained. The corresponding neutral density at the nozzle exit can be determined using the Y-dependence of N which can be obtained from the measurement shown in Fig. 32b, given by

$$N = 1.93 \cdot 10^{18} \cdot \exp\left(-0.0024 \cdot Y\right) \pm 2 \cdot 10^{17} \left[\mathrm{cm}^{-3}\right], \tag{57}$$

where Y is measured in units of μm. The actual pressure can be determined with the equation for ideal gases:

$$P_{real} = N_{SI} \cdot k_B \cdot T, \tag{58}$$

where N_{SI} is the particle density N in m^{-3}, k_B the Boltzmann constant and T the temperature in kelvin. P_{real} is therefore given in pascal. The nozzles used in the multijet experiment can be slightly different due to the electro-erosion process. In addition, the reservoir of the arrays differs compared to the one for the single nozzle. From experience with these nozzles, it is reasonable to assume that one particular nozzle within the multijet array has a slightly higher density. However, the deduced relations from this measurement are adequate and very useful to estimate the pressure range in the array of gas jets. This particularly interesting for HHG simulations, where a pressure is needed as input parameter.

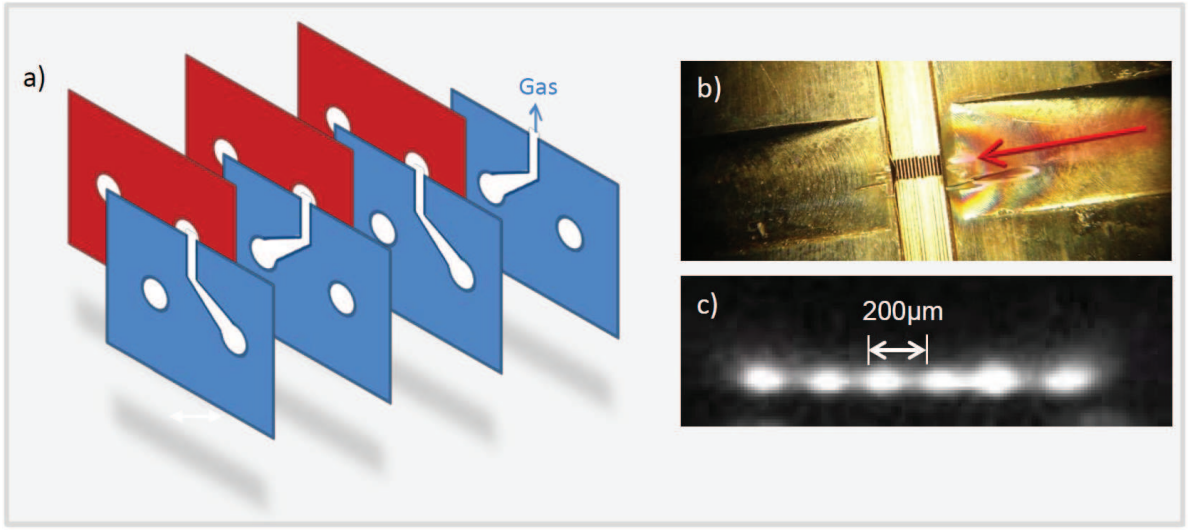

Figure 33: The foil target design. a) Stacked foils with two channels for the generation and matching gas. Thin sealing foils (20 μm, red) are placed between each channel foil (100 μm, blue). b) Top view of the foil target. Foils are compressed by a holder and the laser propagates from right to left. c) Plasma side image of six argon jets and five hydrogen intersections. The QPM period is 200 μm. In addition, two hydrogen jets are set at the front and end of the array to enclose the generation medium.

5.2.3 The Foil Target

The prototype target described in the previous section is suitable for first proof-of-principle experiments. However, it is not easily scalable to a higher number of jets, which is essential to increase the coherent signal build-up. The prototype target relies on a complicated procedure for producing electro-eroded de Laval-nozzles. Furthermore, the crossing angle between driver and matching medium jets may lead to a reduced efficiency due to turbulences.

To increase the flexibility concerning the number of sources (e.g. more than just two or four generation jets), an advanced target design of multiple stacked foils with a rectangular nozzle orifice of 100 μm length (x(200-1000) μm transverse size) has been developed (see Fig. 33). In this configuration, the jets do not have any angle with respect to each other. This avoids problems concerning turbulences. However, the most prominent feature of this advanced dual-gas QPM design is the great flexibility of the jet number and jet size which only depends on the number and geometry of the foils. Steel foils are used to avoid accidental damage, in the case that the laser focus hits the target. The channels for the gas are etched into the steel, which can be done with high precision. The foil design is such, that only one type of foil needs to be produced. This foil can just be flipped to provide two separate channels for the generation and the matching medium (see Fig. 33a). Sealing foils of 20 μm thickness are inserted in between the channel foils to separate the channels. The sealing foils have two holes for the main channels but no nozzle orifice. The stacked foils need to be heavily pressed onto each other to achieve sealing. This is done by a holder system which presses the foils into a dense array of stacked foils (see Fig. 33b). With this system, any kind of nozzle configuration can be implemented.
The backing pressures of the two gas-arrays are controlled separately, providing the same pressure within one channel of the same gas. The jet arrays can be operated in a pulsed mode in order to avoid a high gas load in the vacuum chamber. This is realized with Parker solenoid

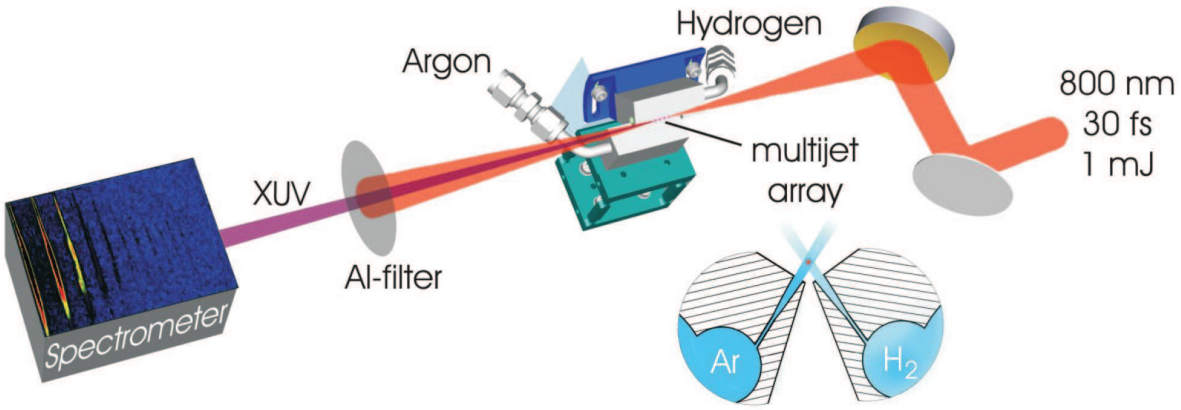

Figure 34: The experimental setup for proof-of-principle tests. A gas jet array consisting of two or four argon HHG jets interspersed with hydrogen phase matching jets allows full control of the relative phase between the source jets by varying the hydrogen pressure. The jet array is irradiated with 30 fs pulses with an energy of 1 mJ from a Ti:Sapphire laser system (800 nm) with a peak intensity in focus of $8 \cdot 10^{14}\,\mathrm{Wcm^{-2}}$. The fundamental laser light is filtered out by two 200 nm Al filters and the XUV pulses are detected by an angularly resolving flatfield spectrometer. Due to geometrical constraints, the highest observable harmonic order was 41.

valves (pulsed valve no. 9S1-A1-P1-9B06) attached directly to the target. It needs to be ensured that the volume between the valve and the nozzle exit is small to guarantee a sharp pulsing. Fig. 33c shows a plasma side image of the resulting gas jet structure. The configuration used for this image consists of six argon jets interspersed with five hydrogen plumes. Due to the high flexibility in the choice of the jet number, the foil target also allows the two enclosing hydrogen jets to be set at the two ends of the QPM array.
The dual-gas scheme realized with this foil target makes it also possible to introduce multiple zones of different backing pressures. This can be realized by adding more channels which are separately controlled. The feature of variable matching phase will be implemented in an advanced version of the foil target, which is currently under development.

5.3 Results and Discussion

The feasibility of the dual-gas QPM concept has been demonstrated in various experiments and the results are summarized in this section. Each experiment had its own focus of interest. In a proof-of principle experiment at the TEI Crete (Greece) using the prototype target, the primary intention was to show that the matching gas (e.g. hydrogen) solely tunes the phase between multiple sources resulting in an harmonic order-dependent QPM effect. Secondly, with the proof that only the phase is varied by the insertion of hydrogen, the effect on the contributions of short and long trajectories was investigated leading to an efficient control of their relative weight. The third intention of the initial dual-gas experiments meets the need of high conversion efficiencies for FEL seeding. The QPM scalability and its quadratic dependence on the QPM period has been investigated within a proof-of-principle experiment as well as in a second experiment at the Center for FEL Science (CFEL) at DESY using the advanced dual-gas

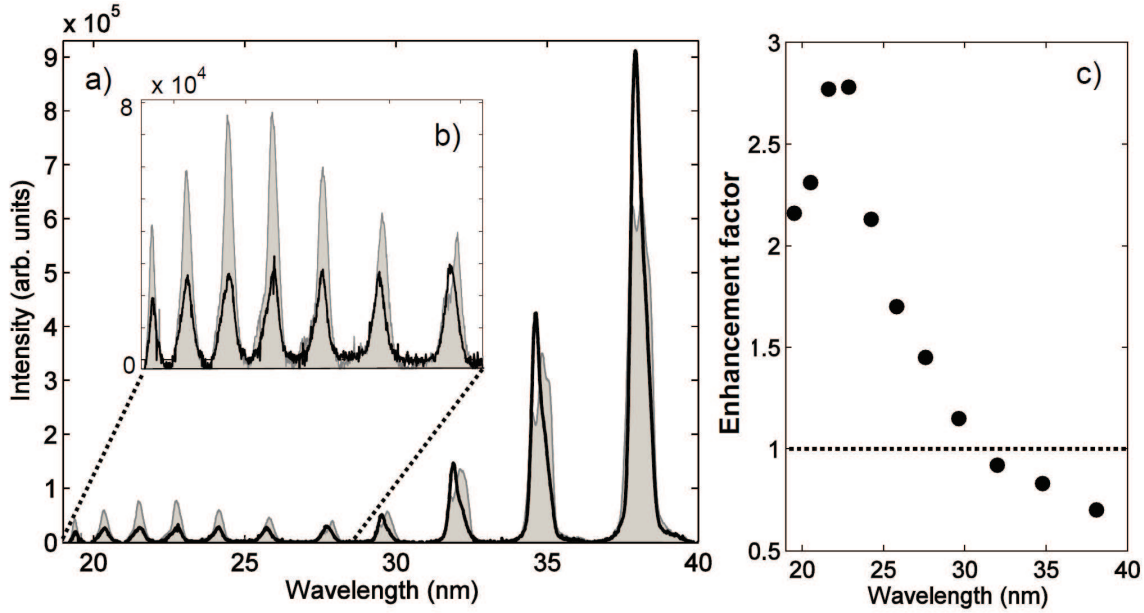

Figure 35: a) Selective enhancement due to QPM in the two nozzle array for two distinct values of hydrogen pressure (black solid: 0.9 bar of hydrogen, shaded gray: 2.35 bar). b) zoomed area of the harmonics 29-41. c) Order-dependent enhancement due to the phase added by hydrogen. The argon backing pressure is 2 bar for all curves.

target which consists of stacked foils. The last results presented in this section are from a third experiment (also at CFEL) aiming to exploit the effect of dual-gas QPM in the short wavelength regime (8-15 nm) with ultrashort laser pulses.

5.3.1 Phase Tuning and Quantum Path Control

The ability to coherently tune the phase between multiple sources and therefore the relative weight of short and long trajectory contributions with dual-gas QPM was tested in the geometry consisting of two argon jets for the HHG half periods and one hydrogen jet for the matching half period. The array within the prototype design was irradiated with 30 fs pulses from a Femtolasers Titanium-Sapphire laser with pulse energies of 1 mJ at a repetition rate of 1 kHz and a central wavelength of 800 nm (see Fig. 34). The laser was focused with a parabolic mirror and an effective focal length of f = 15 cm into the gas array leading to a measured focal diameter of 40 μm (FWHM). A peak intensity of $8{\cdot}10^{14}$ W/cm^2 was achieved with a transmission efficiency of 86% through the entrance window of the vacuum chamber. The XUV radiation was detected using a compact flatfield XUV spectrometer [120] coupled to an ANDOR CCD camera. The grating was mounted about 400 mm behind the interaction point, which results in an angular field-of-view of approximately 15 mrad. The Hitachi flatfield grating was calibrated at the Daresbury Synchrotron source to be able to extract absolute efficiencies from the measurement. Two 200 nm aluminum filters block the infrared radiation to protect the XUV-CCD. The multijet target was mounted on a motorized x-y-z-stage. After optimizing the transverse position with respect to the laser beam, the gas array was positioned 1 mm before the focal spot in order to increase the effect of the intrinsic phase [68]. In addition, the harmonics investigated were chosen to be well within the plateau region of the spectrum to ensure that long and short

trajectory tuning was well distinguishable.
To show the tuning effect of hydrogen as a matching medium in between two argon sources, the argon arrays were set to a constant backing pressure whereas only the hydrogen backing pressure was varied. Note, that no harmonic signal could be observed with hydrogen only. Figs. 35 a and b show the effect of hydrogen in an array of two argon jets separated by one hydrogen jet for two arbitrarily chosen spectra. The solid black curve represents the spectrum recorded with an argon backing pressure of 2 bar and a hydrogen pressure of 0.9 bar. Increasing the hydrogen backing pressure to 2.35 bar led to the shaded gray spectrum. It is obvious that hydrogen has a harmonic order-dependent effect on the spectrum such that harmonic orders beyond the 27$^{\text{th}}$ harmonic are enhanced whereas a decrease in harmonic yield was observed for orders lower than $q = 25$ by changing the hydrogen pressure from 0.9 bar to 2.35 bar (see also Fig. 35c). Such constructive/destructive interference between two sources is a signature of a QPM setup where an order dependent phase ϕ_q is added between two sources. Hence, hydrogen indeed solely adds a phase given by Eq. (55) and therefore fulfills the requirement as matching medium for dual-gas QPM.
The argon pressure of 2 bar is not an arbitrary pressure value. The 2 bar backing pressure for the argon jets was chosen such that the N^2 increase in the temporally, radially and spectrally integrated harmonic yield reached a maximum for all wavelengths visible in the spectrum due to a phase mismatch. Thus, any further increase of the backing pressure led to a decreased harmonic signal. From Eqs. (56) and (57) the real pressure expected at a distance to the nozzle exit of 150 μm and a backing pressure of 2000 mbar can be determined. By applying the ideal gas equation, the real pressure was calculated to be $P_{real} = (18 \pm 7)$ mbar. With this value an estimation of the absorption length was possible. This is important for any interpretation of the achieved results. The absorption length for the 27$^{\text{th}}$ (41$^{\text{st}}$) harmonic was about 11 mm (20 mm) for 18 mbar in argon and thus much longer than the maximum total generation zone of about 1 mm for all four sources. Hence, QPM effects should be observable while tuning the hydrogen backing pressure.
The effect of varying the hydrogen pressure between two argon generation jets for a wavelength range from 19 to 30 nm, corresponding to the 41$^{\text{st}}$ and 27$^{\text{th}}$harmonic of the 800 nm driver, can be seen in Fig. 36a. The argon backing pressure is kept constant at 2 bar. A clear effect of hydrogen can be observed. However, whereas the tuning effect of hydrogen is evident, the oscillation of the harmonic yield seems to be periodic but asymmetric. To investigate the physical effect behind this data, the 41$^{\text{st}}$ and 27$^{\text{th}}$ harmonics were analyzed in more detail. Fig. 36b shows an oscillation of the harmonic yield of the 41$^{\text{st}}$ harmonic with two peaks at 1 bar and around 2.5 bar hydrogen pressure. The spectrally integrated one-dimensional lineout reveals an asymmetric shape of the oscillation. Since changing the density of the fully ionized hydrogen only affects the relative phase between the two sources, such behaviour would not be expected for a well-defined relationship between laser and harmonic phase (i.e. where only one trajectory was present). Under such circumstances a periodic oscillation with hydrogen pressure should be observed. The asymmetry in the oscillation becomes even more obvious in Fig. 36c where the 27$^{\text{th}}$ harmonic was tuned with hydrogen. A spectral splitting in the colour plot was observed and the two spectral components appeared to be tuned separately by hydrogen. The spectrally integrated lineout shows an asymmetry which originates from the superposition of the two spectral features. A smooth oscillation can be observed for each of them by separating the two components (red and black curve in the lineout plot).
This behaviour can be understood in terms of the two distinct quantum trajectories. As discussed

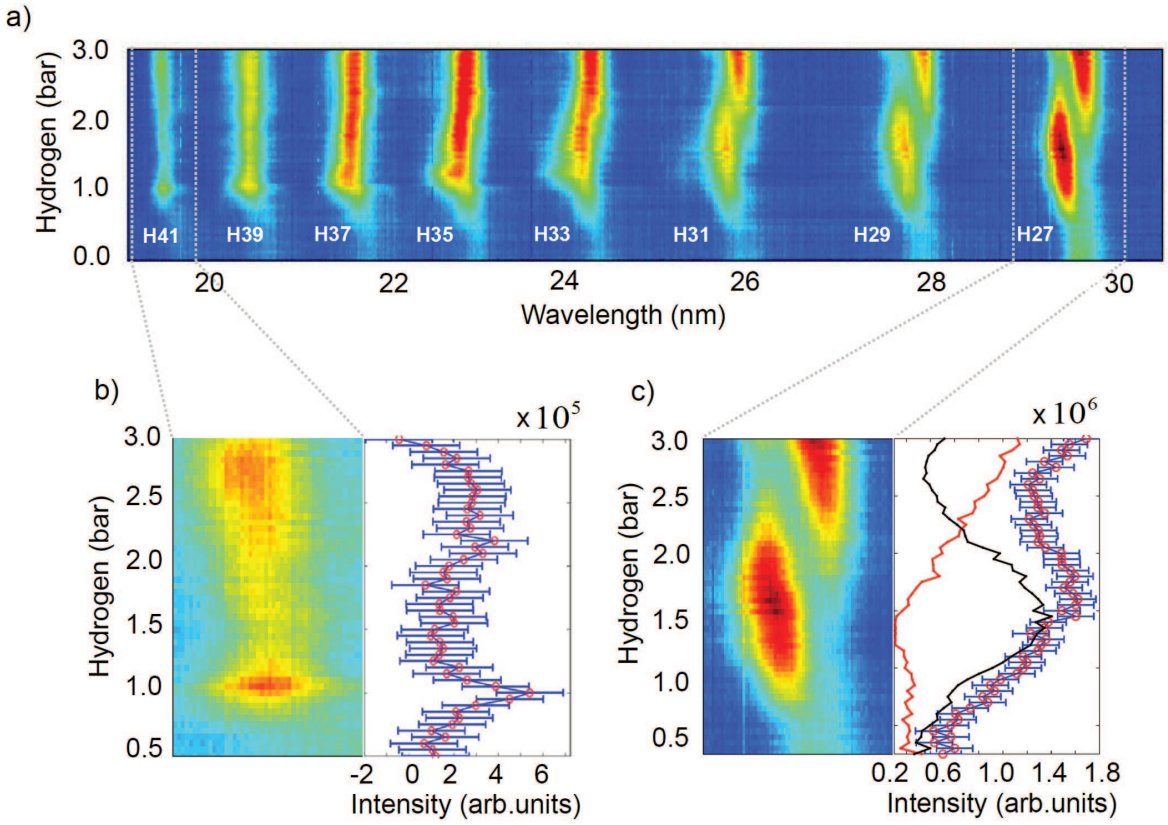

Figure 36: Coherent superposition of two HHG jets with a 2 bar argon pressure and varying hydrogen backing pressure in the matching jet. a) Hydrogen pressure scan from the 27th to the 41st harmonic. b) Enlarged view of the hydrogen scan for the 41st harmonic and c) for the 27th harmonic. One-dimensional lineouts show the spectrally integrated harmonic yield (red dots) and for the 27th, in addition, the contribution of the shorter (black line) and longer wavelength components (red line). The oscillation of the harmonic yield with hydrogen pressure is clearly visible. The error bars indicate the error due to background subtraction.

in section 2.2.5, these trajectories correspond to different ionization and recollision times, but should have the same electron kinetic energy upon return to the atom and consequently result in the emission of photons with approximately the same frequency. However, because of the effects of intercycle ionization and variation in the laser intensity, the exact emission frequency can be slightly different for the two quantum paths resulting in spectral splitting of each harmonic, which is clearly visible for the 27th harmonic in Fig. 36.

To distinguish the effects of the different trajectories from other effects on the harmonic spectral shape (for example ionization induced splitting [151]), 3D simulations were performed, considering each trajectory separately. The jet configuration for the simulation is the same as in the experiment. Two argon jets are interspersed with one hydrogen jet. The HHG simulation was done with a 3D-code based on the saddle-point analysis of the Lewenstein model for the single-atom dipole response as discussed in section 2.2.3 [26, 152]. This approach allows the inclusion of arbitrary quasi-static ionization rates determined with ADK and atom-specific recombination matrix elements. In addition, the code provides a tool to study the contributions of the long and short trajectories separately which is important for our purpose. The detailed

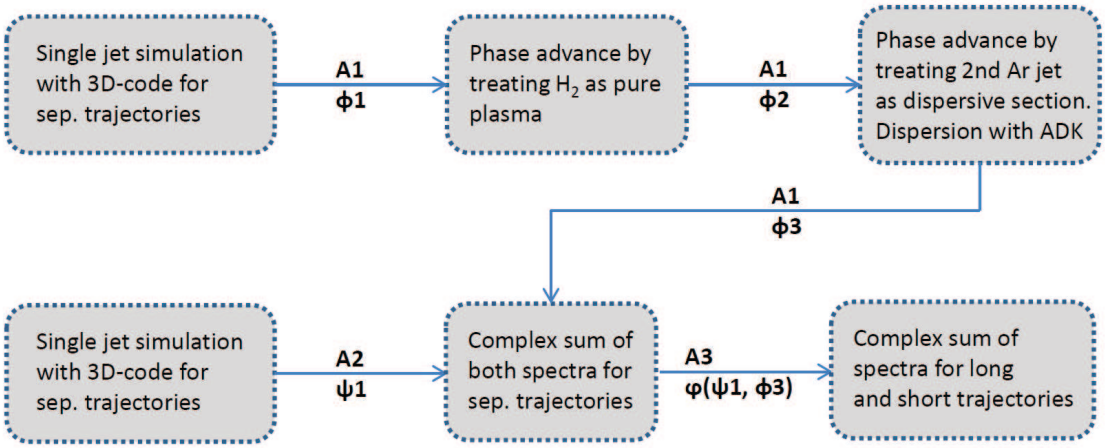

Figure 37: Scheme of 3D dual gas simulations. The first argon jet was simulated with the 3D-code resulting in amplitude A1 and phase $\Phi 1$. The hydrogen matching jet was treated as pure plasma adding a phase to $\Phi 1$, which results in $\Phi 2$. The last argon jet added another phase to the harmonic radiation generated in the first jet, resulting in $\Phi 3$. The second jet generated harmonics with amplitude A2 and phase $\psi 1$. The result of the multijet was the complex sum of both contributions. The final spectrum can be achieved with the complex sum of long and short trajectory contributions.

theoretical method behind the simulation is described in several publications [153, 154, 155]. The code was modified to simulate a multijet array with one hydrogen matching zone. As can be seen in the simulation scheme in Fig. 37, the contributions of the short and long trajectories are accounted by simulating the complex spectrum for both short and long trajectories for the entire pulse and generation length. The spectrum of the first argon jet results in an amplitude A1 and a phase $\Phi 1$ and for the second jet in A2 and $\psi 1$. The matching hydrogen zone in between the argon jets were taken into account by treating them as a purely dispersive medium where the plasma dispersion is the dominant phase term. This additional phase was added to the phase of the spectrum of the first jet resulting in a new phase $\Phi 2$, which depends on the hydrogen pressure. For the harmonic radiation generated in the first jet the second jet was just a dispersive section. The phase advance could be calculated with ADK ionization rates. The resulting spectrum was then added to the spectrum of the second jet, which was calculated separately. In order to compare the real spectral tuning plot with simulations, the long and short trajectory spectra were summed up leading to a complex mixing of both contributions. Note, that the code calculates an electric field $E = E(t,z,\rho)$ with t being the time, z the longitudinal coordinate in the generation volume and ρ the radial coordinate. The third dimension was therefore included assuming axial symmetry, which was fulfilled in our experiment. In Fig. 38a (e) the radially integrated experimental data is presented with respect to the variation in phase due to hydrogen for the 27^{th} (41^{st}) harmonic (as already shown in Fig. 36). The simulated spectrally resolved tuning curves in Fig. 38b (f) show excellent agreement with the experimental data in terms of the spectral dependence on the phase introduced by the hydrogen matching jet. Same as in the experimental plot, the two trajectory contributions were summed up, resulting in a complex and asymmetric structure. As mentioned before, our simulation code allows the contribution of the short and long trajectories to be evaluated separately, and Fig. 38c shows the short-trajectory

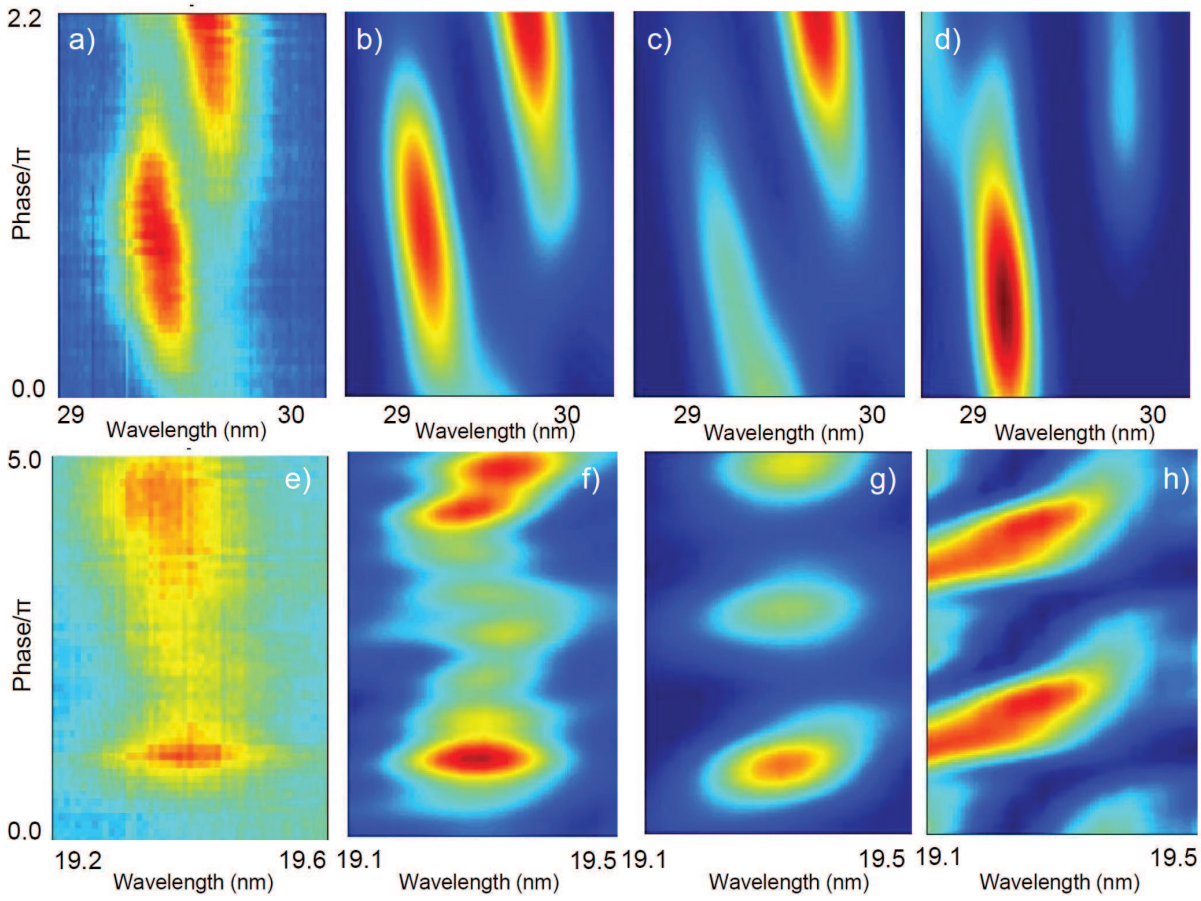

Figure 38: Comparison of the simulated hydrogen pressure scan for the b) 27th and f) 41st harmonic, to the corresponding experimentally obtained spectra in a) and e). The y-axis is labeled with the relative phase advance (normalized to π) due to the hydrogen matching jets. The agreement between experimental and simulated spectra is excellent. The effect of the hydrogen section on each of the two trajectory contributions is shown separately for the 27th [c) short trajectory, d) long trajectory] and the 41st harmonic [g) short, h) long]. Note, that the colour maps of the long trajectory contributions have been enhanced [d) x100 compared to b) and c); h) x10 compared to f) and g)].

contribution to the 27th, whereas Fig. 38d shows the long-trajectory contribution. The results indicate clearly that the long trajectory is dominant in the blue shifted branch and the short trajectory at longer wavelengths. This is an amazing result, because it implies the possibility to choose one path over the other. Especially the selection of only the long trajectory contributions is usually not an easy task. A closer look at Fig. 38c demonstrates that a small fraction of the short trajectory contribution is also present in the blue shifted branch. This spectral splitting within the short trajectory contribution indicates that the laser spectrum is slightly varied due to the high intensity and therefore high plasma density [151]. However, for the long trajectories (Fig. 38d), the splitting is most likely due to interference of the different bursts generated by the long trajectory within each cycle. As one can see in Fig. 10 there are weak additional branches surrounding the dominant long trajectory for the reciprocal intensity. These are also long trajectories but mostly higher order recombinations. This leads to different effects on the intrinsic phase and therefore on the phase matching conditions. As a result, a complex interference pattern can already occur in the tuning plot considering only the long trajectories. This effect is even more pronounced for the 41st harmonic. Again, the measured tuning plot was identified to be the complex sum of the two trajectory contributions. In Fig. 38g, periodic and symmetric oscillations can be seen with increasing hydrogen backing pressure for the short trajectories. In contrast to that, the long-trajectory contributions led to a smeared out structure. However, two maxima are clearly visible showing a wavelength dependent hydrogen pressure value.
In conclusion, the path-dependent intrinsic phase ϕ^{j}_{QP} leads to a difference in the tuning effect of the passive medium hydrogen for the long and short trajectories. Thus, strong suppression of the unwanted quantum paths can be achieved by setting the relative phase between individual jets such that only the desired trajectory contribution is allowed to build up coherently over many QPM periods.

Note, that the 41st harmonic shows a larger phase range than for the 27th. This is well within expectations, because the matching phase introduced by the hydrogen gas is larger for higher harmonic orders (see Eq. (55)) leading to a shorter coherence length for the shorter wavelengths. The excellent agreement of the 3D-simulations with the measurement demonstrates that the interference between short and long trajectories can be controlled effectively by inserting phase matching zones consisting of fully ionized hydrogen leading to a high flexibility in the choice of the quantum paths. For FEL seeding, the QPM tuneability allows a substantial control over the FEL pulse characteristics in terms of pulse shape and spectral properties by achieving full spatial and spectral coherence in a single harmonic by selecting the short quantum paths. Clearly the long trajectory contributions can also be phase matched on axis, adding additional flexibility to the range of wavelengths than can be produced efficiently. This flexibility is of particular interest to increase the tunability of the FEL wavelength [67] - albeit potentially at the cost of reduced coherence as discussed in section 2.2.5.
A further measurement was performed to test the ability of quantum path control also for a multijet with more than two sources. For this purpose an array consisting of four source and three matching jets were used. The energy was slightly reduced compared to the previous measurement whereas all other parameters were the same. In Fig. 39, the 35thto 39thharmonic order is presented with 100 mbar and 1900 mbar hydrogen matching pressure at a constant argon pressure of 2 bar. Same as for the two source array, one can clearly see spectral splitting due to quantum path interference, where quantum path dependent phase matching was clearly present. For the lower backing pressure of 100 mbar the shorter trajectory was preferentially selected for all three harmonic orders shown in the plot. The variation of the phase ϕ_q with harmonic

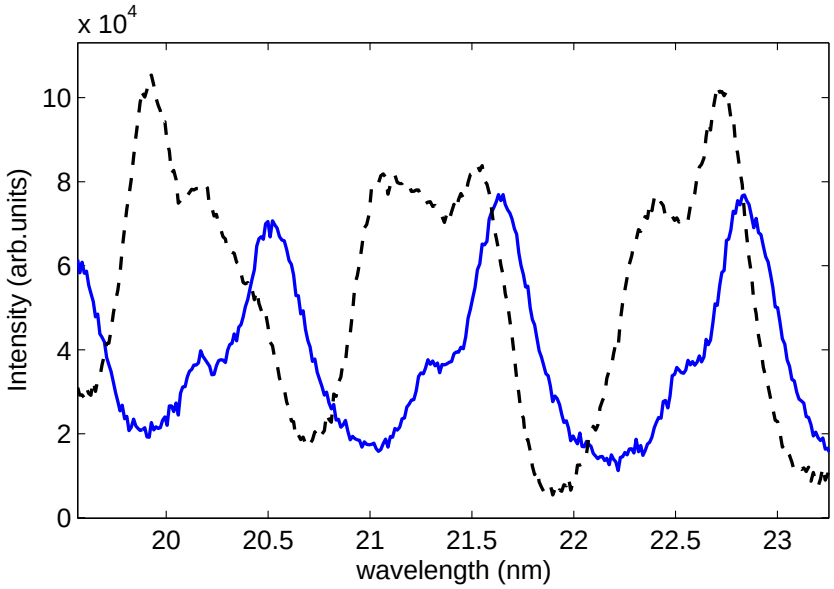

Figure 39: With a multijet configuration consisting of four source and three matching jets, the relative weight of the quantum paths is also controllable. Comparing the orders 35-39 at 100 mbar (blue solid) and 1.9 bar (black dashed) hydrogen backing pressure demonstrates the order dependent control of the relative weight of the short and long trajectory contributions. The argon backing pressure is 2 bar.

order is linearly dependent on the pressure. This implies that for 1900 mbar hydrogen pressure the tuning effect determined by ϕ_q was 19 times larger than that at 100 mbar pressure. As a result for 1900 mbar backing pressure, the relative weight of the different spectral contributions changed with the order number such that for the 35^{th} (39^{th}) harmonic the short (long) trajectory contribution was dominant, whereas for the 37^{th} harmonic the contributions were of equal strength. Therefore, the efficient control of quantum paths was not limited to any specific number of jets. With the reproduction of the results achieved with two sources it was demonstrated that the effect was solely a result of the hydrogen matching pressure.
In conclusion, by effectively controlling the relative weight of the two quantum paths, the temporal and spatial profile as well as coherence properties can be tuned to fit the best requirements for the FEL seeding process. This control is particularly interesting when high densities are necessary for high harmonic yield. In this case, the influence of the long trajectories can be significant, which can be counteracted by varying the hydrogen pressure.

5.3.2 The QPM Scaling

With the highly efficient control of the transverse and longitudinal coherence and profile an important requirement for seeding has been fulfilled. However, the main problem of the seeding process remains: the harmonic pulse energies need to dominate the shot noise in the FEL undulators (see Fig. 28). To achieve such high energy values, the number of periods in the QPM scheme needs to increase. Theoretically, the increase in energy scales with N_{QPM}^2. The scalability was tested in two different ways using the prototype target as well as the advanced foil-based design. Note, that the aim of these first experiments was not to achieve new records in conversion efficiencies. In fact, the main objective was to show that the principle QPM scaling

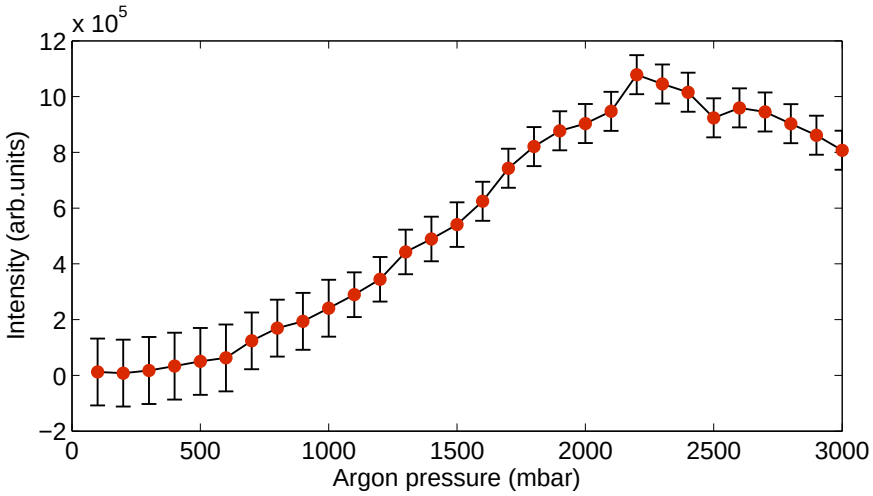

Figure 40: Harmonic intensity in dependence on the argon backing pressure (no hydrogen present). The saturation is clearly visible at 2 bar backing pressure.

dependence on the quadratic number of QPM periods holds even for source numbers exceeding two or four. If this coherent build-up can be shown, the generation of high harmonic energies only relies on the interplay between the optimized source position, the jet number, generating gas type and vacuum conditions.

A two or a four source array can be implemented using the dual-gas prototype. This opens the possibility to compare the enhancement of best phase-matched yield using twice the source number of a reference array. Comparing the two-source array with the four source array and three matching jets, an enhancement factor of $(4-2)^2 = 4$ is expected for perfect coherent build-up of the harmonic yield. The argon backing pressure was kept constant at 2 bar, where the harmonic signal from the argon emitters without any hydrogen showed the first maximum (see Fig. 40). This is important because it needs to be clear that any enhancement occurring with increasing hydrogen pressure is due to the phase variation in the matching jets and not due to increasing argon density. For the comparison the 41^{st} harmonic (19.5 nm) as the highest order observable in the spectrum was chosen to ensure minimal absorption in the interaction area. The experimental condition were the same as for the quantum path control measurements.

Hydrogen pressure scans were performed for both the two- and the four-sources array. Fig. 41a shows the hydrogen tuning curve for the 41^{st} harmonic and a maximum harmonic yield was found at about 1 bar hydrogen pressure. In the prototype target design, only the values at best phase matching can be compared, because in this state it was ensured that both configurations showed a phase advance of π in each matching zone. Hence, comparing the maxima in Fig. 41a, an enhancement factor of 3.9 ± 0.2 between 2 to 4 sources is clearly visible. A peak-to-peak comparison of the spectrum at the 41^{st} harmonic should also lead to an enhancement factor of 4 with 1 bar hydrogen and 2 bar argon. In Fig. 41b) a peak-to-peak factor of 3.7 ± 0.2 can be observed, well within theoretical expectations. Thus, a factor of ≈ 4 is present in the spectrum and in the integrated signal at this harmonic. This relative enhancement showed that the QPM scaling was clearly observable in this configuration. The splitting and blueshift in Fig. 41b) was due to the longer path length for the four-source array and was caused by ionization blue shifting and quantum path interference as discussed in the previous section.

As a consequence, the four-jet array was expected to give 16x the yield of a single jet under the

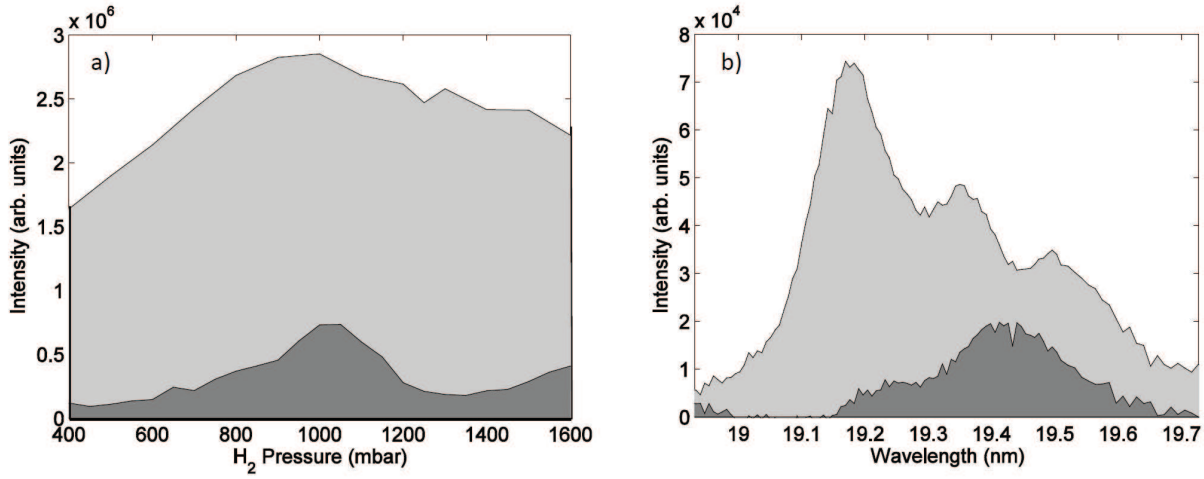

Figure 41: Relative QPM enhancement of the 41st harmonic (19.5 nm) between two sources (shaded dark grey) and four sources (shaded light grey). a) Dependence of the spectrally and radially integrated harmonic yield on the hydrogen backing pressure at a fixed argon pressure of 2 bar. b) Peak-to-peak comparison between the radially integrated spectrum at 1 bar hydrogen and 2 bar argon pressure.

same conditions. Unfortunately it was not possible to show these absolute enhancements with the prototype target. Therefore, a follow-up experiment incorporating the foil-based dual-gas target was performed. The objective was to demonstrate enhancements solely due to QPM. An elegant and simple method for directly observing the full enhancement factor only due to QPM in multijet configurations was introduced by Seres et al. [82]. The theory connected to this method makes the key simplification that the single-atom emission amplitude is the same for all atomic emitters. In addition, a dispersion dominated by free electrons is assumed, leading to a linear dependence of the phase mismatch on the particle density of free electrons. The harmonic yield is then given by

$$I_q \approx \frac{1-(-1)^{N_{QPM}}\cos(\pi N_n)}{1+\cos\left(\pi/N_{QPM}\cdot N_n\right)}\cdot\sin^2\left(\frac{\pi N_n}{2N_{QPM}}\right), \tag{59}$$

where $N_{max,q}$ is the largest particle density for the single jet case ($N_{QPM}=1$) for which the intensity of the q^{th} harmonic monotonically grows (e.g. increasing the density any further would lead to destructive interference) and $N_n = N/N_{max,q}$ is the normalized atomic density (with the atomic density N). In this sense the normalized density is the point at which the length of the single or merged jet L_M is equal to one coherence length L_c.

The best phase matching for a series of source jets (i.e. $N_{QPM}>1$) with an individual length of L_M/N_{QPM} is obtained by adjusting the generating pressure to a higher density of $N_{QPM}\cdot N_{max,q}$, such that each individual jet in the array corresponds to one coherence length. This allows the quality of the QPM to be evaluated by comparing a configuration with $N_{QPM}=1$ (i.e. a single jet without QPM) to a configuration with $N_{QPM}>1$ while keeping the total length of the source gas (and therefore the geometry of the individual jets) constant. This is a very elegant method to demonstrate the QPM effect.

An experiment with six QPM periods was performed in order to demonstrate the QPM scaling with the method of Seres et al. [82]. The advanced foil target was used in this experiment.

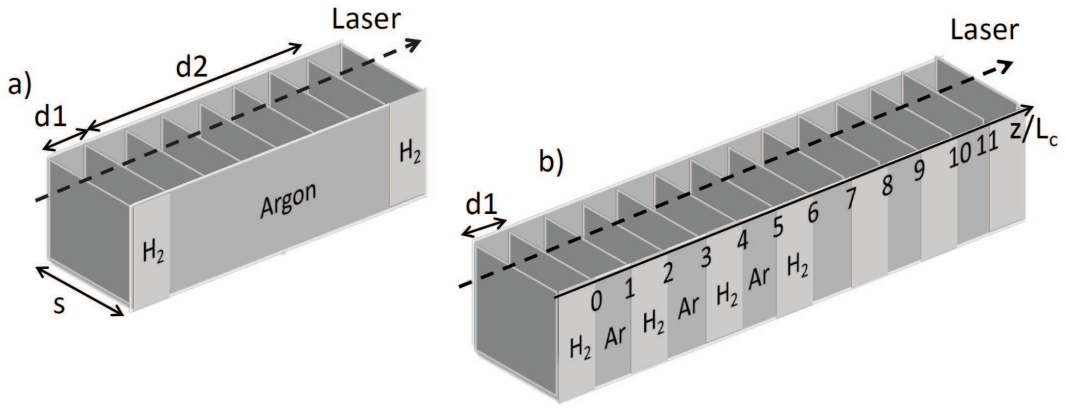

Figure 42: Foil configurations for the QPM scaling experiment. a) The merged-jet array consists of two enclosing hydrogen and six argon jets. Jet size is $d1 = 100\,\mu$m, and with the sealing foils the total merged jet has a length of $d2 = 700\,\mu$m. b) The QPM configuration consists of six argon source jets interspersed with five matching jets and two enclosing hydrogen jets.

Thus, it was possible to use up to six driving jets and 5 matching zones. The reference target necessary for comparison was a merged argon jet of a total size of 700 μm (see Fig. 42a). The QPM configuration, as shown in Fig. 42b, had six argon jets interspersed with hydrogen jets leading to six QPM periods. With the enclosing hydrogen jets the total number of gas jets is 13.

A schematic of the experiment is shown in Fig. 43. A Ti:Sapphire laser amplifier system (Red Dragon, KM-Labs) with 35 fs pulses and up to 15 mJ pulse energy at a repetition rate of 1 kHz was used as driver laser. The central wavelength of the system was 800 nm. The laser radiation was focused by a lens with an effective focal length of f = 1000 mm leading to a measured focal diameter of 70 μm full width at half maximum. The peak intensity derived from focal measurements was $9 \cdot 10^{14}$ W/cm^2 and $6 \cdot 10^{14}$ W/cm^2 at pulse energies of 4 mJ and 2.8 mJ, respectively. The jet array was positioned within the Rayleigh range of the focused laser beam. Similar to the first experiment, the backing pressures in the two arrays were controlled separately providing the same pressure within an array. The infrared radiation was filtered out with a 300 nm thin aluminum foil. The harmonic beam was detected with the flatfield spectrometer already used for the first experiment. However, within this experiment, it was necessary to increase the distance between source and spectrometer due to the larger focal length. The distance between source and CCD was increased to 2.76 m. In addition, a remotely controlled high precision slit was installed to enable knife edge measurements to determine the divergence and source size of the harmonic beam. This is of special interest for the seeding source.

In a first step, the reference target (Fig. 42a) was used to determine the dependence of the harmonic yield on the generating argon density. The enclosing hydrogen jets were set to a constant backing pressure of 100 mbar. For each argon pressure a spectrum was recorded. Note, that also in this case no harmonic signal was present with hydrogen gas only. In a second step the target was extended by five hydrogen jets separating the argon zones, whereas the total generation length was kept constant (Fig. 42b). For two sets of data the harmonic intensity was plotted vs. argon backing pressure in Fig. 44a. At first, the merged argon jet of length 700 μm showed the characteristic phase oscillations with increasing argon pressure (see also Fig. 44b). The data points, corresponding to the case $N_{QPM} = 1$ were fitted using Eq. (59)

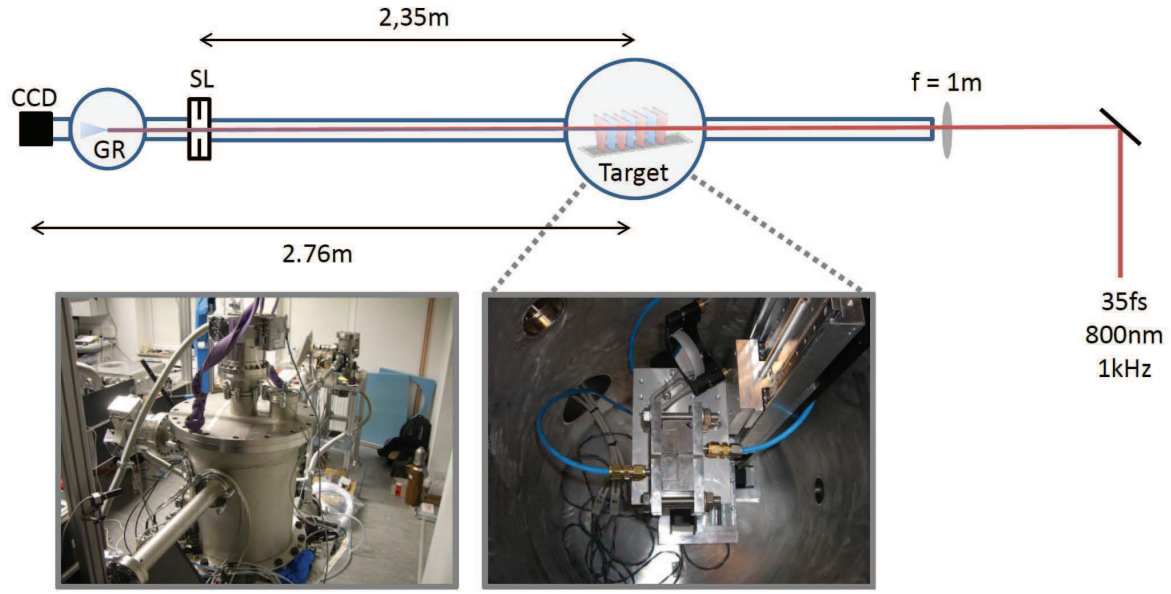

Figure 43: Scaling experiment using a 800 nm driver laser with 35 fs pulse duration and a repetition rate of 1 kHz. The maximum energy per pulse is 4 mJ. The beam is focused into the QPM target with a $f = 1$ m lens. The spectrometer is equipped with a slit (SL), a flatfield grating (GR) and an ANDOR CCD. The distance between slit and target is 2 m, and between CCD and target 2,5 m.

(green curve). Correspondingly, $N_{max,q}$ was estimated to be 87.5 mbar. In contrast to the theory, the experimental data exhibited no zero signal minima with increasing backing pressure. In addition, the maxima of the harmonic oscillations slightly increased. This is due to off-axis phase matching [156], which starts to play a role at higher densities. Off-axis effects are not included in the simple theory and thus not considered in Eq. (59).

The QPM effect with hydrogen was demonstrated in the dataset with the $N_{QPM} = 6$ multijet array. By keeping the interaction length with argon constant, any enhancement occurring will be an effect of pure QPM. The hydrogen pressure was chosen to maximize the output at an argon backing pressure of $p = 6 \times 87.5 = 525$ mbar (corresponding to a density of $N_{QPM} \cdot N_{max,q}$). Afterwards the argon pressure scan was repeated within this configuration. The measured data fit well to the theoretical expectation for $N_{QPM} = 6$ (Fig. 44a). This is the first demonstration of an enhancement factor of 36 for a multijet array consisting of six sources compared to a single source of the same size. This result confirms the QPM scalability with dual-gas QPM.

The primary aim of this study was to show the sole QPM scaling effect with dual-gas QPM and not to demonstrate optimized conversion efficiencies. However, for the further development it is interesting to calculate the efficiency from this dataset. The efficiency was calculated using the transmission curve for the aluminum filter, the grating efficiency and the detector response curve. For an intensity of $9 \cdot 10^{14}$ W/cm^2, the best conversion efficiencies achieved with the $N_{QPM} = 6$ array were $1.2 \cdot 10^{-5}$, $9 \cdot 10^{-6}$ and $3 \cdot 10^{-6}$ for the 19th, 23rd and 27th harmonic order, respectively. This is already close to highest values reported for a 800 nm driver in the literature to date [144, 157, 158]. However, further optimization is necessary to achieve adequate harmonic energies for all wavelengths of interest. This can be done by optimizing both the number of QPM periods, the thickness of the jets and of course the choice of the

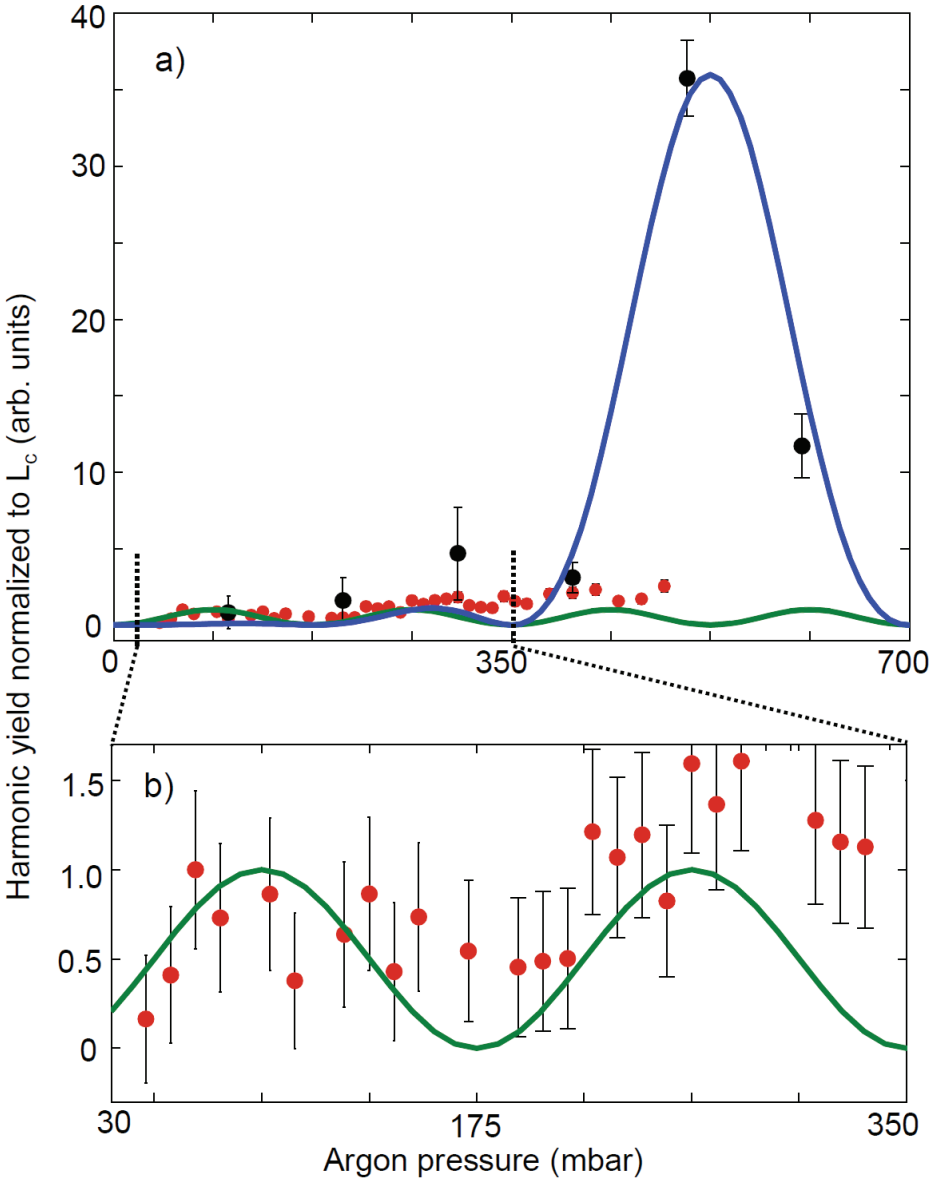

Figure 44: a) Comparison of the harmonic energy vs. argon pressure for the 27th harmonic using a 700 μm merged argon jet (red dots) and a dual-gas multijet with 5 hydrogen intersections by maintaining the total length of the argon nozzles (black dots). For comparison, the theoretical curves were included for $N_{QPM} = 1$ and $N_{QPM} = 6$. b) Enlarged plot of the phase oscillations measured with the merged argon jet corresponding to $N_{QPM} = 1$. All uncertainties were due to shot-to-shot fluctuations during the measurement and due to background subtraction.

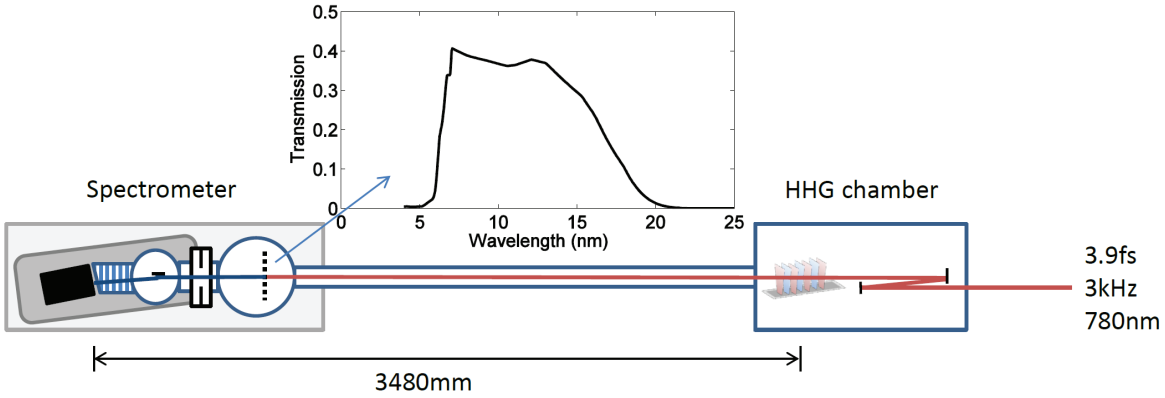

Figure 45: Schematic of the short-wavelength experiment. 3.9 fs pulses were focused with a spherical mirror ($f = 75\,cm$) into the dual-gas target. The generated radiation was diagnosed by the newly designed XUV-spectrometer at a total distance of 3480 mm. Inset: Transmission curve for 300 nm zirconium.

generating gas type.

5.3.3 Dual-gas QPM at short Wavelengths

The aim of all these studies is the efficient generation of a seed beam by upconversion of the driver to wavelengths ranging from 10 to 40 nm. In experiments previously described, the principle of quantum path control and QPM scaling were demonstrated. The shortest wavelength observed during these investigations was 19.6 nm, the 41st harmonic of the 800 nm driver laser system. A third experiment, recently performed at CFEL was set up to show the effect of dual-gas QPM in the short wavelength regime. For all studies the focus was on wavelengths within the zirconium transmission window (see inset of Fig. 45). In addition, the effect of carrier-envelope phase (CEP) for the stabilization of the ultrashort infrared pulses as driver for dual-gas QPM was investigated.
A schematic of the experimental setup is shown in Fig. 45. A Ti:Sapphire laser amplifier system (FemtoPower) delivered 3.9 fs pulses at a repetition rate of 3 kHz and a central wavelength of 780 nm. The pulse energy was about 430 μJ. The measured focal spot size with a focal length of 750 mm was 60 μm (FWHM). An intensity of $2.3 \cdot 10^{15}$ W/cm^2 was used for the HHG process. The focusing was achieved with a spherical mirror inside the HHG chamber to avoid dispersion caused by a lens and to avoid damage on the entrance window in the case of out-of-vacuum focusing. The generated XUV radiation was diagnosed by the XUV spectrometer specially developed for FLASH2 (see section 3.3.4). Thus, this experiment was also a first test for the new diagnostics. The spectrometer was equipped with several 200 to 500 nm zirconium filters blocking the infrared radiation.
First measurements were done without any CEP stabilization. With random CEP, distinct harmonics can be expected even for few-cycle pulses in the short wavelength regime. An example spectrum recorded with neon during the experimental run is given in Fig. 46a. The harmonics in the spectrum were clear and distinct, an indication that no trajectory mixing occurred. The radially integrated lineout gives the characteristic shape of spectra measured within the zirconium window. Especially the signal decrease towards longer wavelength was due to the filter

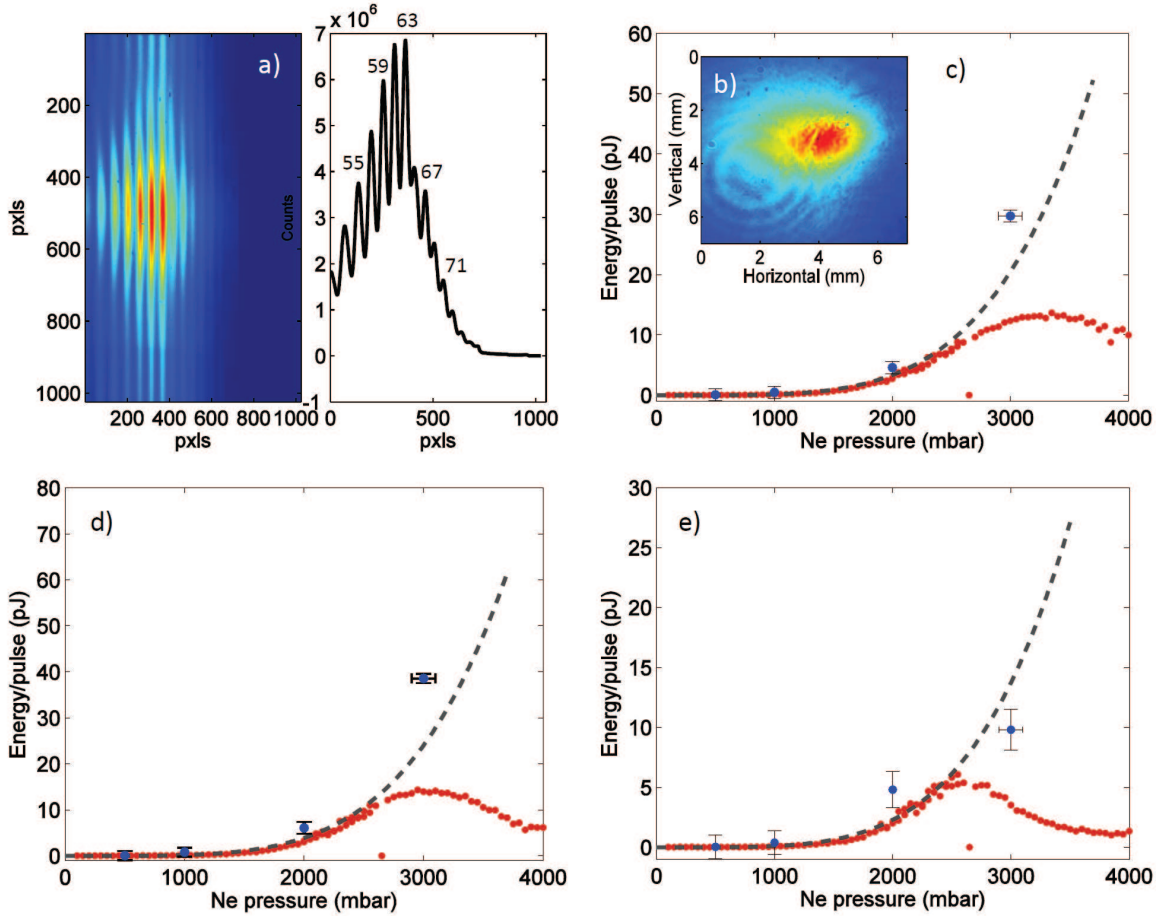

Figure 46: a) Spectrum recorded with 3.9 fs pulses with neon as the generating medium. The radially integrated lineout is shown in the second half of the figure. The harmonic numbers are indicated in the lineout plot. b) Transverse size of the harmonic beam within the Zr window. c) QPM effect as a result of hydrogen tuned to maximum harmonic yield for the 53rd, d) 63rd and e) 71st harmonic. The neon pressure scan without any hydrogen (red circles) show quasi-quadratic enhancement until the phase advance reaches π. The ideal curve without phase mismatch was plotted as grey dashed line. The QPM data points (blue circles) basically follow this line. Note, that the errors were due to uncertainties in the actual pressure.

transmission curve. The abrupt dip at 12.3 nm occurred due to absorption in a silicon layer of the XUV CCD. It can be calculated that this dip causes an intensity drop of about 30%, corresponding to 18 nm silicon. The silicon dip was used to calibrate the spectrum. The signal decreased beyond that dip towards shorter wavelengths due to the macroscopic cutoff. The highest harmonic order observable in the spectrum was $q = 79$ which corresponds to 9.9 nm (125.4 eV). With the new spectrometer it was possible to measure the direct XUV beam as well as the spectrum. The direct beam within the bandwidth of the zirconium filter is given in Fig.46b. The beam was slightly asymmetric with a transverse size of $d_x = 3.1$ mm (FWHM) and $d_y = 2.2$ mm (FWHM).

The main aim of this experiment was the enhancement of the high harmonic signal beyond driving densities corresponding to one coherence length. In general, in the phase matching regime of the HHG process (e.g. at generation densities corresponding to $\leq L_c$), the insertion of hydrogen would cause a signal decrease. Performing hydrogen scans in this phase matching regime of the neon pressure curve, the highest value achievable was the value measured without hydrogen. However, as soon as best phase matching can no longer be achieved with the merged generating jet, inserted hydrogen jets can correct for the mismatch leading to a quasi-quadratic signal growth even beyond the signal saturation with neon only. This was experimentally confirmed and the harmonic yield is plotted in Figs. 46c-e for the 53^{rd} (14.7 nm), 63^{rd} (12.4 nm) and 71^{st} harmonic (11 nm). The pure neon pressure scans exhibited the characteristic signal maximum. It is obvious, that the phase mismatch set in earlier at shorter wavelengths. This indicates an order dependent phase matching effect. It excludes other effects like absorption as the origin for the signal decrease. Each QPM data point was measured by performing a hydrogen scan at a constant neon pressure value. Note, that the maximum of only the first three hydrogen oscillations were shown in the plot. This ensures that no other effects like ionization induced intensity changes cause the enhancement. The measured harmonic yield follows the quasi-quadratic curve, corresponding to the theoretically possible yield without any phase effects (grey dashed lines), within the errors. This demonstrates an excellent QPM scaling. Note, that in this analysis, absolute numbers for the harmonic energies were calculated and shown in the plots. From Fig. 46, 29.7 pJ, 38,6 pJ and 10,0 pJ were observed as maximum energy values for the 53^{rd}, 63^{rd}, and 71^{st} harmonic, respectively. This corresponds to the respective conversion efficiencies of $8 \cdot 10^{-8}$, $1 \cdot 10^{-7}$ and $3 \cdot 10^{-8}$. Although these values were very promising, more effort is necessary to increase the harmonic output. However, in this experimental configuration, especially for harmonics close to the cutoff, no further optimization was possible due to two main limitation. First, the gas pressure was limited in the vacuum chamber. In order to reach the maximum harmonic generation with a dual-gas free-jet configuration, the density needed to achieve the phase advance of π leading to a first signal oscillation corresponds to high backing pressures. This leads to high demands on the vacuum pumping system. Second, a few-cycle pulse limits the gas density due to dispersion effects, which changes the temporal and spatial characteristics of the driver pulse. In general, for few-cycle laser pulses, long jet configurations as well as high densities need to be avoided if a preservation of the temporal and spatial pulse properties is required. Hence, dual-gas QPM has the potential to enhance the signal by maintaining a low gas density-length product.

A continuous spectrum is required for attosecond pulse production which can be achieved by stabilizing the CEP of the driver pulses [32]. The stabilization has the effect that the cycles within the envelope do not vary in time from shot to shot. The constant phase relation between successive pulses leads to the generation of short pulse lengths and therefore broad spectra. In

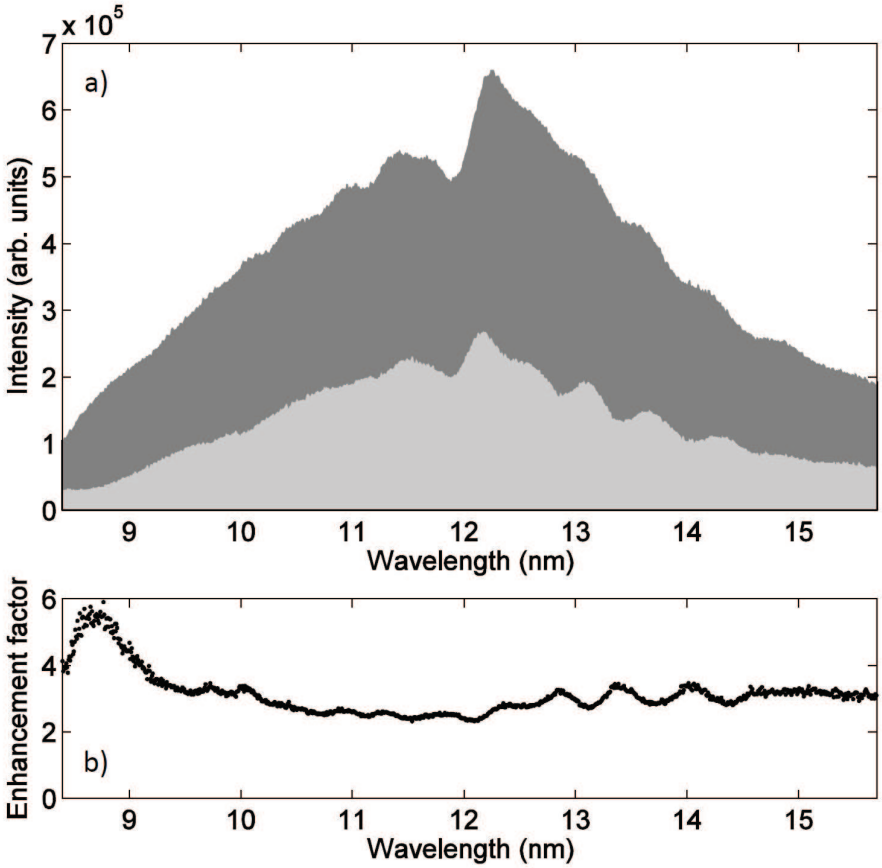

Figure 47: a) Harmonic spectrum recorded with ultrashort, CEP stabilized laser pulses. The spectrum without any hydrogen (lightly shaded) and the enhancement due to the insertion of hydrogen (darkly shaded, 625 mbar hydrogen backing pressure) is displayed. b) Enhancement factor vs. wavelength.

Fig. 47a the continuous shape of the spectrum is shown. The pulse length was 4 fs and the CEP was stabilized. The neon backing pressure was set to 2.5 bar. The dual-gas configuration with six source jets interspersed with matching jets was used as QPM target. The lightly shaded spectrum was recorded without hydrogen. This spectrum served as reference spectrum. The spectrum recorded with 625 mbar hydrogen backing pressure is plotted in Fig. 47a in order to demonstrate the effect of the hydrogen matching zones (dark shaded area). An enhancement of the complete spectral range could be observed. This is a very interesting result in terms of enhancing the yield of attosecond pulses. By enhancing the complete continuum, the whole attosecond pulse experiences enhancement without any change in the spectrum or pulse length. Note, that the spectra shown in Fig. 47 include the effect of the 300 nm zircon filter leading to the characteristic intensity decrease towards longer wavelengths. The dip in the center is again due to the silicon absorption within the CCD.
Although the complete spectrum experienced enhancement, the enhancement factor was not a constant. The factor of enhancement in dependence of the wavelength is given in Fig. 47b. Whereas wavelengths above 10 nm showed a relatively constant enhancements of about a factor 3, the wavelengths approaching the macroscopic cutoff experienced enhancement up to a factor 6. Therefore, the very short wavelengths within the macroscopic cutoff experienced the most

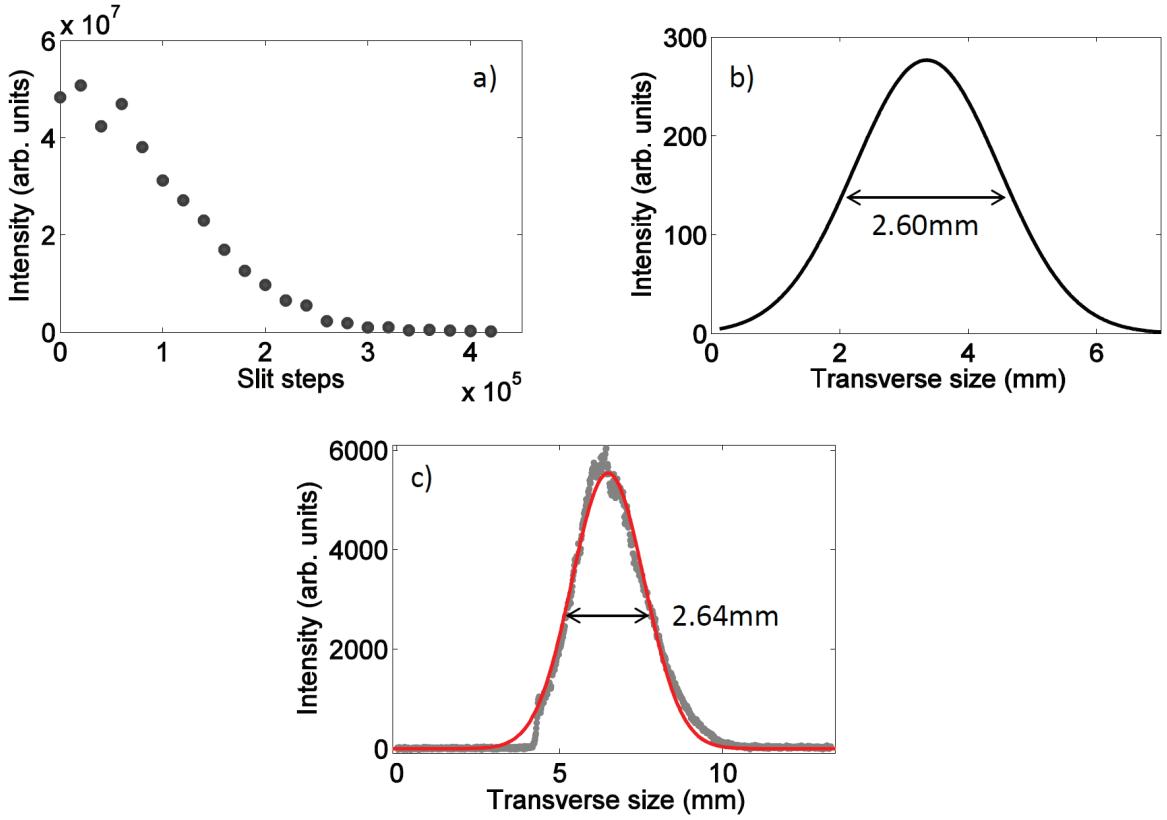

Figure 48: a) Knife edge measurement for the 27thharmonic. The slit was moved across the beam and caused a reduction of intensity. b) Derivation of the knife edge curve led to the actual transverse beam size. c) Beam size measurement with the CCD. The pixel size is 13x13 μm.

enhancement. This led to an effective extension of the macroscopic cutoff.
Simulations are currently in preparation in order to confirm the observed behaviour. If these measurements can be confirmed, dual-gas QPM becomes highly attractive for attosecond pulse generation.

5.3.4 Source Size Measurements

First divergence measurements were performed during the QPM scaling experiment at CFEL. During the measurement the argon and hydrogen backing pressure was set to 600 mbar and 100 mbar, respectively. The divergence could be determined by either using a motorized slit which was implemented in the setup (see Fig. 43), or by the XUV CCD itself. The flatfield spectrometer has the convenient feature that the spatial shape is preserved in one dimension. Therefore, it is possible to slowly insert the slit by measuring spectra for each step. The slit was calibrated beforehand so that the beam size could be derived from the knife edge measurement. Furthermore, the detector pixel size is well known giving the beam size at a second position. The slit was positioned 2.35 ± 0.05 m behind the target whereas the detector had a distance of 2.76 ± 0.05 m to the source.
The slit moved 64103 steps per mm. A knife edge scan was performed with a resolution of 20000 steps. The radially and spectrally integrated intensity in dependence on the slit move-

ment for the 27thharmonic is given in Fig. 48a. The higher the slit step number, the more the beam was cut. The derivative of the resulting curve shows the real transverse dimension of the beam. The transversal beam profile determined with this method is shown in Fig. 48b. From this plot a transverse size of $d = 2.6 \pm 0.1$ mm (FWHM) can be obtained, corresponding to $d_w = 4.37 \pm 0.3$ mm (2w; contains 95% of the beam energy).
The divergence can be estimated with the expression

$$\tan\Theta = \frac{1}{2} \cdot \frac{d_w}{D}. \tag{60}$$

For the position D of the slit, measured from the source, the divergence can be estimated to be $\Theta = 0.9 \pm 0.1$ mrad. An estimation of the corresponding source size can be achieved by assuming a Gaussian shape for the XUV radiation. With this assumption the source size can be estimated by calculating the beam waist

$$w_0 = \frac{\lambda}{\pi \tan\Theta}. \tag{61}$$

For example, the 27thharmonic, corresponding to $\lambda_{27} = 29.6\,nm$ for a 800 nm driver, gave a source size of $21 \pm 1\,\mu$m (2w) corresponding to $12.5 \pm 0.6\,\mu$m (FWHM). As stated before, the measured focal spot size was $70\,\mu$m (FWHM) during the QPM scaling experiment. Thus, the source size was about 20% of the initial laser focus. Due to the assumption that the beam had a Gaussian shape, the determined source size was just a lower limit.
To confirm the source size, the same calculation was done at the position of the CCD. On the detector, the 27thharmonic had a beam size corresponding to $d = 2.64 \pm 0.1$ mm (FWHM) or $d_w = 4.43 \pm 0.2$ mm (2w; see Fig. 48c). With Eq. (60) the divergence can be estimated to be 0.8 ± 0.04 mrad. The corresponding source size was $23.5 \pm 0.6\,\mu$m (2w) corresponding to $14 \pm 0.4\,\mu$m (FWHM). This agrees well to the values determined with the knife edge measurement.
The usage of the new spectrometer in the third experiment enabled a beam profile analysis also for the last experimental configuration. The feature of direct beam measurement led to the possibility to measure the horizontal and vertical transverse size independently. From Fig. 46b the spot size at a distance of $D = 3480 \pm 50$ mm was estimated to be 5.2 ± 0.2 mm ($2w_x$) and 3.7 ± 0.2 mm ($2w_y$). Therefore, the divergences were given by $\Theta_x = 0.7 \pm 0.03$ mrad and $\Theta_y = 0.5 \pm 0.03$ mrad. By assuming a Gaussian shape, a lower limit for the source size can be estimated. With the calculated divergences the source size amounted to $s_x = 11 \pm 0.2\,\mu$m and $s_y = 15 \pm 0.2\,\mu$m for 12 nm. The focal measurement of the laser pulse showed a spot size of $100.8\,\mu$m (2w). The source size therefore appeared to be very small. However, note, that the Gaussian limit always led to a lower limit for the source size. A Gaussian shape is only an approximation. The real source size is therefore larger than the calculated value.
These source parameters are very important for the FEL seeding setup. Detailed studies on the source size and divergence will be performed with the dual-gas target and the novel OPCPA driver system in order to determine the required optics for the seed injection scheme. An interesting subject will be the influence of varying hydrogen pressure on the source parameters.

6 Conclusion and Outlook

A novel seeding source has been developed in order to meet the requirements of the FEL FLASH2. The conversion from infrared to XUV radiation is realized with high harmonic generation in gases. We have shown, for the first time for a multijet HHG configuration, coherent control of the two main quantum paths by controlling the relative phase of the sources with matching zones consisting of completely ionized hydrogen gas inserted between the HHG zones. This result was fully supported by 3D-simulations which demonstrated quantum path interference to be the origin of the complicated spectral shape measured during the proof-of-principle experiment. The efficient control of quantum path contributions allowed a direct influence on the XUV beam coherence and on the spatial and temporal pulse profile. This is important for an adequate coupling between seed and electron beam within the FEL, as well as for the FEL beam quality.

The novel dual-gas QPM scheme allowed not only for coherence control but also for a significant enhancement of the harmonic yield following the scaling law $I_q \propto (N_{QPM})^2$ with the QPM period N_{QPM}. This was demonstrated experimentally for QPM periods of up to $N_{QPM} = 6$. This new approach, not limited to any specific number of nozzles, represents a relatively simple tool for increasing the conversion efficiency to its theoretical limit. For short harmonic wavelengths ($< 25\,\text{nm}$), where current HHG efficiencies are substantially smaller than those required by the FEL seeding process, this method is particularly attractive. The low self-absorption at shorter wavelengths implies that jet arrays with $N_{QPM} > 10$ are possible with a decreased nozzle opening. It should be noted, that all results achieved during the reported experiments were well reproducible. The combination between coherence control and the enhancement of the harmonic yield makes it highly attractive for FEL seeding at FLASH2.

In principle, our scheme can be extended to almost any medium as long as the ionization potential of the HHG medium exceeds that of hydrogen. Therefore, it will also be possible to exploit the high ionization potential media offered by ion species while controlling the phase matching conditions at the same time. Furthermore, it should be emphasized that this method is in principle also applicable to capillary waveguides, both with and without a discharge, which makes absorption limited HHG using this method applicable to smaller-scale laser systems.

Dual-gas QPM has the potential to achieve highest harmonic energies even at wavelength ranges close to the water window. However, multiple, separately controlled pressure zones needs to be implemented in order to approach the theoretical limit. This is particularly challenging from a technical point of view. A new target design is currently under development including 6 separate pressure control zones. The number of jets per control section can be varied. With such a configuration, changes in the driver pulse intensity distribution can be balanced by varying the driving and matching densities from one pressure section to the next. This will lead to higher harmonic energies essential for an efficient seeding process.

Ultimately from the current perspective, the limit of the dual-gas QPM scheme is only given by absorption effects and focusing geometry. To overcome the latter limit, laser systems with higher pulse energies can be used, resulting in a focusing geometry with much larger confocal parameters, while maintaining the appropriate intensity for HHG. In the case of FLASH2, the driving pulse energy is fixed at about 2 mJ at 760 nm central wavelength. Thus, a further optimization of the HHG process can only be achieved by applying schemes such as shaped focal spots with flat top beam profiles. The reduction of absorption effects, however, can be achieved with an efficient pumping system. For this purpose a chimney concept was developed,

which guarantees direct pumping of the major part of the gas jet before it can spread into the vacuum system. The chimney is installed right above the array exit. Recent tests showed an improvement of the chamber vacuum by one order of magnitude during operation. The aim is to maintain a pressure of 10^{-4} mbar in the HHG target chamber.
The OPCPA laser system required for seeding FLASH2 has exceptional parameters with 2 mJ pulse energy at a central wavelength of 760 nm, 10-15 fs pulse duration and a 100 kHz repetition rate in 10 Hz bursts. A prototype version of the OPCPA setup was tested and very promising results could be achieved at 60 and 96 kHz repetition rates. The current design of the fiber pump amplifier installed at DESY shows excellent performance in the required burst mode. Further investigations are necessary in order to decide whether a thin-disk or Innoslab amplifier will be used as booster amplifier in the pump setup. These experiments are ongoing and the two stage OPA is already prepared in order to achieve all design parameters as soon as the design pump pulse energy of 20 mJ can be generated. For a stable operation of the seed source, energy fluctuations as well as pointing variations need to be minimized. Thus, the laser development includes also various techniques to stabilize the laser output which is directly imprinted into the HHG radiation.
The injection scheme has been discussed and first suggestions of how the source can be included in the beam line have been made. For a further, detailed discussion about the concrete injection mirror configuration, start-to-end simulations with Genesis are necessary as well as a full characterization of the harmonic beam generated with dual-gas QPM. The latter issue is subject of detailed measurements planned at DESY as soon as the OPCPA system delivers the design parameters.

In conclusion, the achievements of both the new OPCPA amplifier and the novel dual-gas QPM HHG scheme form the basis to enable seeding at FLASH2. Each part represents a major advance in its field. Thus, the laser amplifier as well as the HHG target are of high interest for other applications besides FEL seeding. The success of enhancing a complete continuous spectrum with hydrogen, as presented in the last chapter, demonstrates the high potential of the dual-gas scheme for attosecond science. However, detailed simulations need to support the findings and 3D-simulations are currently in preparation.
Whether direct seeding is feasible at FLASH2 will depend on various developments. Even if the source finally delivers harmonic energies exceeding the FEL shot noise, especially for wavelengths around 10 nm, an adaptive injection mirror and a longitudinal and transverse characterization of the electron beam are necessary in order to realize externally initiated micro-bunching. The degree of longitudinal and transverse coupling between electrons and seed radiation will be the bottle neck of the project. With an adequate contrast between shot noise and seed ($\approx$x100), the seeded FEL radiation can be expected to dominate the FEL spectrum. Additionally, by ensuring that the short trajectory is phase-matched on axis within the HHG process, especially the longitudinal coherence can be expected to be highly improved compared to the SASE radiation. Dual-gas QPM can help to combine a good coherence with an harmonic energy yield ensuring a good contrast between SASE and seeded FEL radiation.
The seed source is important and the progress achieved in this work holds promise for the seeding project. However, it is just one part of a complicated seeding setup and many challenges needs to be met before first seeded light will be observed at the new FLASH2 FEL.

References

[1] R. Wideröe. Über ein neues prinzip zur herstellung hoher spannungen. *Arch. f. Elektrot.*, 21:387, 1928.

[2] E.O. Lawrence and D. Sloan. The production of heavy high speed ions without the use of high voltages. *Phys. Rev.*, 38:2022, 1931.

[3] F. R. Elder, A. M. Gurewitsch, R. V. Langmuir, and H. C. Pollock. Radiation from electrons in a synchrotron. *Phys. Rev.*, 71:829–830, 1947.

[4] J.M.J. Madey. Stimulated emission of bremsstrahlung in a periodic magnetic field. *J. Appl. Phys.*, 42:1906, 1971.

[5] G. Lambert et al. Injection of harmonics generated in gas in a free-electron laser providing intense and coherent extreme-ultraviolet light. *Nature Physics*, 4:296–300, 2008.

[6] A. McPherson et al. Studies of multiphoton production of vacuum-ultraviolet radiation in the rare gases. *JOSA B*, 4:595, 1987.

[7] X.F. Li, A. L'Huillier, M. Ferray, L.A. Lompre, and G. Mainfray. Multiple-harmonic generation in rare gases at high laser intensity. *Phys. Rev. A*, 39:5751, 1989.

[8] P. Schmüser, M. Dohlus, and J. Rossbach. *Ultraviolet and Soft X-Ray Free-Electron Lasers*. Springer Verlag, 2008.

[9] J.D. Cockcroft and E.T.S. Walton. Experiments with high velocity ions. In *Proceedings of Royal Society Series A*, number 136, pages 619–630, 1932.

[10] S. Reiche. Genesis 1.3: a fully 3d time-dependent fel simulation code. *Nucl. Instrum. Meth. Phys. Res. A*, 429:243, 1999.

[11] K. J. Kim. An analysis of self-amplified spontaneous emission. *Nucl. Instrum. Meth. Phys. Res. A*, 250:396, 1986.

[12] F. Löhl. Measurements of the transverse emittance at the vuv-fel. *TESLA-FEL Report*, 2005-03, 2005.

[13] Homepage of the european xfel: http://www.xfel.eu.

[14] J. A. Armstrong, N. Bloembergen, J. Ducuing, and P. S. Pershan. Interactions between light waves in a nonlinear dielectric. *Phys. Rev.*, 127:1918, 1962.

[15] W. Joosen, H. J. Bakker, L. D. Noordam, H. G. Muller, and H. B. van Linden van den Heuvell. Parametric generation in b barium borate of intense femtosecond pulses near 800 nm. *J. Opt. Soc. Am. B*, 8:2087, 1991.

[16] D. Strickland and G. Mourou. Compression of amplified chirped optical pulses. *Optics Comm.*, 56:219, 1985.

[17] A. Dubietis, R. Butkus, and A. Piskarskas. Trends in chirped pulse optical parametric amplifiers. *IEEE J. Sel. Topics QE*, 12:163–172, 2006.

[18] G. A. Reider. *Photonik*. Springer Verlag, 1997.

[19] Y.-R. Shen. *The Principles of Nonlinear Optics*. John Wiley and sons, 1984.

[20] F. Tavella, A. Marcinkevicius, and F. Krausz. Inverstigation of the superfluorescence generation in a multiterawatt opcpa. *New J. Phys.*, 8:219, 2006.

[21] E. G. Lariontsev and V. N. Serkin. Influence of self-focusing on structure of ultrashort light pulses in laser with clarifying filter. *Radiophys. Quan. Electron.*, 19:251–255, 1975.

[22] A. Penzkofer, M. Wittmann, W. Bäumler, and V. Petrov. Theoretical analysis of contributions of self-phase modulation and group-velocity dispersion to femtosecond pulse generation in passive mode-locked dye lasers. *Appl. Opt.*, 31:7067, 1992.

[23] G. E. Cook. Pulse compression-key to more efficient radar transmission. *IEEE Proc. IRE*, 48:310, 1960.

[24] A. Dubietis, G. Jonusauskas, and A. Piskarskas. Powerful femtosecond pulse generation by chirped and stretched pulse parametric amplification in bbo crystal. *Optics Comm.*, 88:437–440, 1992.

[25] P. B. Corkum. Plasma perspective on strong-field multiphoton ionization. *Phys. Rev. Lett.*, 71:1994, 1993.

[26] M. Lewenstein, P. Balcou, M. Y. Ivanov, A. L'Huillier, and P. B. Corkum. Theory of high-harmonic generation by low-frequency laser fields. *Phys. Rev. A*, 49:2117, 1994.

[27] K. C. Kulander, K. J. Schäfer, and J. L. Krause. Dynamics of short-pulse excitation, ionization and harmonic conversion. In *Proceedings of Workshop SILAP III*, volume 316, page 95, New York (USA), 1993.

[28] J. L. Krause, K. J. Schäfer, and K. C. Kulander. Hohg from atoms and ions in the high intensity regime. *Phys. Rev. Lett.*, 68:3535, 1992.

[29] E. J. Takahashi, T. Kanai, K. L. Ishikawa, Yasuo Nabekawa, and K. Midorikawa. Coherent water window x ray by phase-matched high-order harmonic generation in neutral media. *Phys. Rev. Lett.*, 101:253901, 2008.

[30] J. Seres et al. Laser technology: Source of coherent kiloelectronvolt x-rays. *Nature*, 433:596, 2005.

[31] A. Gordon and F. X. Kärtner. Scaling of kev hhg photon yield with drive wavelength. *Optics Express*, 13:2941, 2005.

[32] T. Popmintchev et al. Bright coherent attosecond-to-zeptosecond kiloelectronvolt x-ray supercontinuum. In *Proceedings of CLEO 2011*, number PDPC12, Baltimore (USA), 2011.

[33] E. L. Falcao-Filho et al. Scaling of high-order harmonic efficiencies with visible wavelength drivers: A route to efficient extreme ultraviolet sources. *Appl. Phys. Lett.*, 97:061107, 2010.

[34] L. V. Keldysh. Ionization in the field of a strong electromagnetic wave. *Sov. Phys. JETP*, 20:1307–1314, 1965.

[35] C. Spielmann et al. Near-kev coherent x-ray generation with sub-10-fs lasers. *IEEE J. ST QE*, 4:249–265, 1998.

[36] A. M. Perelomov, V. S. Popov, and M. V. Terent'ev. Ionization of atoms in an alternating electric field. *Sov. Phys. JETP*, 23:924–934, 1966.

[37] M. V. Ammosov, N. B. Delone, and V. P. Krainov. Tunnel ionization of complex atoms and of atomic ions in an alternating electromagnetic field. *Sov. Phys. JETP*, 64:1191–1194, 1986.

[38] A. M. Perelomov and V. S. Popov. Ionization of atoms in an alternating electric field. ii. *Sov. Phys. JETP*, 24:207, 1967.

[39] A. M. Perelomov and V. S. Popov. Ionization of atoms in an alternating electric field. iii. *Sov. Phys. JETP*, 25:336, 1967.

[40] Q.-Z. Yu, Y.-T. Li, J. Zhang, J. Zheng, H.-M. Li, X.-Y. Peng, and K. Li. Characterization of density profile of cylindrical pulsed gas jets. *Chin. Phys. Lett.*, 21:874, 2004.

[41] S. Augst, D. D. Meyerhofer, D. Strickland, and S. L. Chin. Laser ionization of noble gases by coulomb-barrier suppression. *J. Opt. Soc. Am. B*, 8:858–867, 1991.

[42] P. B. Corkum, N. H. Burnett, and F. Brunel. Above-threshold ionization in the long-wavelength limit. *Phys. Rev. Lett.*, 62:1259, 1989.

[43] C. M. Kim and C. H. Nam. Selection of an electron path of high-order harmonic generation in a two-color femtosecond laser field. *J. Phys. B*, 39:3199, 2006.

[44] Y. Mairesse et al. Attosecond synchronization of high-harmonic soft x-rays. *Science*, 302:1540–1543, 2003.

[45] S. Kazamias and Ph. Balcou. Intrinsic chirp of attosecond pulses: Single-atom model versus experiment. *Phys. Rev. A*, 69:063416, 2004.

[46] A. Morlens, P. Balcou, P. Zeitoun, C. Valentin, V. Laude, and S. Kazamias. Compression of attosecond harmonic pulses by extreme-ultraviolet chirped mirrors. *Optics Letters*, 30:1554–1556, 2005.

[47] K. T. Kim, C. M. Kim, M. Baik, G. Umesh, and C. H. Nam. Single sub-50-attosecond pulse generation from chirp-compensated harmonic radiation using material dispersion. *Phys. Rev. A*, 69:051805(R), 2004.

[48] M. Lewenstein, P. Balcou, M. Y. Ivanov, and A. L'Huillier. Phase of the atomic polarization in high-order harmonic generation. *Phys. Rev. A*, 52:4747, 1995.

[49] K. Schiessl, K. L. Ishikawa, E. Persson, and J. Burgdörfer. Quantum path interference in thewavelength dependence of high-harmonic generation. *Phys. Rev. Lett.*, 99:253903, 2007.

[50] Pascal Salières, Anne L'Huillier, and Maciej Lewenstein. Coherence control of high-order harmonics. *Phys. Rev. Lett.*, 74:3776–3779, 1995.

[51] A. Rundquist, C. G. Durfee III, Z. Chang, C. Herne, S. Backus, M. M. Murnane, and H. C. Kapteyn. Phase-matched generation of coherent soft x-rays. *Science*, 280:1412, 1998.

[52] P. Balcou, P. Salieres, A. L'Huillier, and M. Lewenstein. Generalized phase-matching conditions for high harmonics: the role of field-gradient forces. *Phys. Rev. A*, 55:3204–3210, 1997.

[53] J. Boedewadt et al. sflash - first results of direct seeding at flash. In *Proceedings of FEL 2010*, number WEOAI2, page 330, Malmö (Sweden), 2010.

[54] E. Constant, D. Garzella, P. Breger, E. Mével, Ch. Dorrer, C. Le Blanc, F. Salin, and P. Agostini. Optimizing high harmonic generation in absorbing gases: Model and experiment. *Phys. Rev. Lett.*, 82:1668–1671, Feb 1999.

[55] E. Constant, D. Garzella, P. Breger, E. Mevel, C. Dorrer, C. Le Blanc, F. Salin, and P. Agostini. Optimizing high harmonic generation in absorbing gases: Model and experiment. *Phys. Rev. Lett.*, 82:1668, 1999.

[56] M. Schnürer, Z. Cheng, M. Hentschel, G. Tempea, P. Kalman, T. Brabec, and F. Krausz. Absorption-limited generation of coherent ultrashort soft-x-ray pulses. *Phys. Rev. Lett.*, 83:722, 1999.

[57] P. Balcou, P. Salieres, and A. L'Huillier. Phase-matching effects in strong-field harmonic generation. *Phys. Rev. A*, 47:1447, 1993.

[58] Cheng Jin, Anh-Thu Le, and C. D. Lin. Medium propagation effects in high-order harmonic generation of ar and n_2. *Phys. Rev. A*, 83:023411, 2011.

[59] Ch.-J. Lai and F. X. Kärtner. The influence of plasma defocussing in high harmonic generation. *Optics Express*, 19:22377, 2011.

[60] P. Balcou, A. S. Dederichs, M. B. Gaarde, and A. L'Huillier. Quantum-path analysis and phase matching of high-order harmonic generation and high-order frequency mixing processes in strong laser fields. *J. Phys. B*, 32:2973, 1999.

[61] M. Bellini, C. Lynga, A. Tozzi, M. B. Gaarde, T. W. Häsch, A. L'Huillier, and C.-G. Wahlström. Temporal coherence of ultrashort high-order harmonic pulses. *Phys. Rev. Lett.*, 81:297, 1998.

[62] M. B. Gaarde, F. Salin, E. Constant, P. Balcou, K. J. Schäfer, K. C. Kulander, and A. L'Huillier. Spatio-temporal separation of high-harmonic radition into two quantum path components. *Phys. Rev. A*, 59:1367, 1999.

[63] P. Salieres et al. Feynmans path-integral approach for intense-laser-atom interactions. *Science*, 292:902, 2001.

[64] Mette B. Gaarde and Kenneth J. Schafer. Quantum path distributions for high-order harmonics in rare gas atoms. *Phys. Rev. A*, 65:031406, Mar 2002.

[65] P. Antoine, A. L'Huillier, and M. Lewenstein. Attosecond pulse trains using high-order harmonics. *Phys. Rev. Lett.*, 77:1234–1237, 1996.

[66] P. Antoine, D. B. Milosevic, A. L'Huillier, M. B. Gaarde, P. Salière, and M. Lewenstein. Generation of attosecond pulses in macroscopic media. *Phys. Rev. A*, 56:4960–4969, 1997.

[67] X. He et al. Spatial and spectral properties of the high-order harmonic emission in argon for seeding applications. *Phys. Rev. A*, 79:063829, 2009.

[68] T. Auguste, B. Carré, and P. Salière. Quasi-phase-matching of high-order harmonics using a modulated atomic density. *Phys. Rev. A*, 76:011802(R), 2007.

[69] C. Lynga, M. B. Gaarde, C. Delfin, M. Bellini, T. W. Hänsch, A. L'Huillier, and C.-G. Wahlström. Temporal coherence of high-order harmonics. *Phys. Rev. A*, 60:4823–4830, 1999.

[70] T. Auguste, P. Saliere, A. S. Wyatt, A. Monmayrant, I. A. Walmsley, and E. Cormier. Theoretical and experimental analysis of quantum path interference in high-order harmonic generation. *Phys. Rev. A*, 80:033817, 2009.

[71] E. Benedetti, J.-P. Caumes, G. Sansone, S. Stagira, C. Vozzi, and M. Nisoli. Frequency chirp of long electron quantum paths in high-order harmonic generation. *Optics Express*, 14:2242, 2006.

[72] P. Saliers, A. L'Huillier, P. Antoine, and M. Lewenstein. Study of the spatial and temporal coherence of high order harmonics. *Adv. At. Mol. Opt. Phys.*, 41:83, 1998.

[73] L. Le Détroff, P. Salière, and B. Carré. Beam-quality measurement of a focused high-order harmonic beam. *Optics Letters*, 23:1544, 1998.

[74] Y. Mairesse et al. Optimization of attosecond pulse generation. *Phys. Rev. Lett.*, 93:163901, 2004.

[75] A. Paul, R. A. Bartels, R. Tobey, H. Green, S. Weiman I. P. Christov, M. M. Murnane, H. Kapteyn, and S. Backus. Quasi-phase-matched generation of coherent extreme ultraviolet light. *Nature*, 42:51–54, 2003.

[76] I.P. Christov, H. C. Kapteyn, and M. M. Murnane. Dispersion-controlled hollow core fiber for phase matched harmonic generation. *Optics Express*, 3:360, 1998.

[77] M. Zepf, B. Dromey, M. Landreman, P. Foster, and S. M. Hooker. Bright quasi-phase-matched soft-x-ray harmonic radiation from argon ions. *Phys. Rev. Lett.*, 99:143901, 2007.

[78] B. Dromey, M. Zepf, M. Landreman, and S. M. Hooker. Quasi-phase-matching of harmonic generation via multimode beating in waveguides. *Optics Express*, 15:7894–7900, 2007.

[79] A.L. Lytle, X. Zhang, P. Arpin, O. Cohen, M. M. Murnane, and H. C. Kapteyn. Quasi-phase matching of high-order harmonic generation at high photon energies using counterpropagating pulses. *Optics Letters*, 33:174–176, 2008.

[80] P.B. Corkum, N.H. Burnett, and M.Y. Ivanov. Subfemtosecond pulses. *Optics Letters*, 19:1870, 1994.

[81] P.L. Shkolnikov, A. Lago, and A.E. Kaplan. Optimal quasi-phase-matching for high-order harmonic generation in gases and plasma. *Phys. Rev. A*, 50:R4461, 1994.

[82] J. Seres, V. S. Yakovlev, E. Seres, Ch. Streli, P. Wobrauschek, Ch. Spielmann, and F. Krausz. Coherent superposition of laser-driven soft-x-ray harmonics from successive sources. *Nature Physics*, 3:878–883, 2007.

[83] A. Pirri, C. Corsi, and M. Bellini. Enhancing the yield of high-order harmonics with an array of gas jet. *Phys. Rev. A*, 78:011801(R), 2008.

[84] D.M. Gaudiosi, B. Reagan, T. Popmintchev, M. Grisham, M. Berrill, O. Cohen, B. C. Walker, M. M. Murnane, H. C. Kapteyn, and J. J. Rocca. High-order harmonic generation from ions in a capillary discharge. *Phys. Rev. Lett.*, 96:203001, 2006.

[85] X. Zhang, A. L. Lytle, T. Popmintchev, X. Zhou, H. C. Kapteyn, M. M. Murnane, and O. Cohen. Quasi-phase-matching and quantum-path control of high-harmonic generation using counterpropagating light. *Nature Physics*, 3:270, 2007.

[86] M. Hentschel et al. Attosecond metrology. *Nature*, 414:509, 2001.

[87] P. M. Paul, E. S. Toma, P. Breger, G. Mullot, F. Auge, P. Balcou, H. G. Muller, and P. Agostini. Observation of a train of attosecond pulses from high harmonic generation. *Science*, 292:1689, 2001.

[88] M. B. Gaarde, J. L. Tate, and K. J. Schafer. Macroscopic aspects of attosecond pulse generation. *J. Phys. B*, 41:132001, 2008.

[89] G. Sansone et al. Isolated single-cycle attosecond pulses. *Science*, 314:443, 2006.

[90] C. Zhang, P. Wei, Y. Huang, Y. Leng, Y.Zheng, Z. Zeng, R. Li, and Z. Xu. Tunable phase-stabilized infrared optical parametric amplifier for high-order harmonic generation. *Optics Letters*, 34:2730–2732, 2009.

[91] V. Ayvazyan et al. First operation of a free-electron laser generating gw power radiation at 32 nm wavelength. *Eur. Phys. Journ. D*, 37:297, 2006.

[92] M. Beye, F. Sorgenfrei, W. F. Schlotter, W. Wurth, and A. Föhlisch. The liquid-liquid phase transition in silicon revealed by snapshots of valence electrons. *Proc. Natl. Acad. Sci.*, 39:16772, 2010.

[93] S. Hellmann et al. Ultrafast melting of a charge-density wave in the mott insulator 1t-tas2. *Phys. Rev. Lett.*, 105:187401, 2010.

[94] A. Meents, S. Gutmann, A. Wagner, and C. Schulze-Briese. Origin and temperature dependence of radiation damage in biological samples at cryogenic temperatures. *PNAS*, 107:1094, 2010.

[95] K. Honkavaara, B. Faatz, J. Feldhaus, J. Rossbach, S. Schreiber, and R. Treusch. Flash upgrade. In *Proceedings of iPAC 2010*, number TUOARA01, page 1290, Kyoto (Japan), 2010.

[96] S. Schreiber et al. First lasing in the water window with 4.1 nm at flash. In *Proceedings of FEL 2011*, number TUOBI2, Shanghai (China), 2011.

[97] M. Geitz, A. Kabel, G. Schmidt, and H.Weise. Bunch compressor ii at the tesla test facility. In *Proceedings of PAC 1999*, page 2507, New York (USA), 1999.

[98] E. Vogel et al. Status of the 3rd harmonic systems for flash and xfel in summer 2008. In *Proceedings of LINAC 2008*, number TUP034, page 471, Viktoria BC (Canada), 2008.

[99] M. Röhrs. Investigation of the phase space distribution of electron bunches at the flash-linac using a transverse deflecting structure. *DESY Report*, 2008-012, 2008.

[100] L. Fröhlich. Machine protection for flash and the european xfel. *TESLA-FEL Report*, 2009-03, 2009.

[101] K. J. Kim. An analysis of self-amplified spontaneous emission. *Nucl. Instrum. Meth. Phys. Res. A*, 250:396, 1986.

[102] A. L. Cavalieri et al. Clocking femtosecond x rays. *Phys. Rev. Lett.*, 94:114801, 2005.

[103] A. Azima et al. Time-resolved pump-probe experiments beyond the jitter limitations at flash. *Appl. Phys. Lett.*, 94:144102, 2009.

[104] J. Kim, J. Chen, Z. Zhang, F. N. C. Wong, F. X. Kärtner, F. Löhl, and H. Schlarb. Long-term femtosecond timing link stabilization using a single-crystal balanced cross correlator. *Optics Letters*, 32:1044, 2007.

[105] S. Schulz et al. All-optical synchronization of distributed laser systems at flash. In *Proceedings of PAC 2009*, number TH6REP091, page 4174, Vancouver (Canada), 2009.

[106] H. Delsim-Hashemi et al. Status of sflash, the seeding experiment at flash. In *Proceedings of iPAC 2010*, number TUPE009, page 2161, Kyoto (Japan), 2010.

[107] B. Faatz et al. Flash ii: Perspectives and challenges. *Nucl. Instrum. Meth. Phys. Res. A*, 635:S2–S5, 2011.

[108] L. Giannessi et al. Fel experiments at sparc: Operation in seeded and chirped mode. In *Proceedings of FEL 2010*, number MOOAI4, page 4, Malmö (Sweden), 2010.

[109] T. Togashi et al. First observation of the 61.5 nm seeded fel at the scss test accelerator. In *Proceedings of FEL 2010*, number MOOAI7, page 13, Malmö (Sweden), 2010.

[110] V. Miltchev et al. sflash - present status and commissioning results. In *Proceedings of iPAC 2011*, number TUZA02, San Sebastian (Spain), 2011.

[111] N. Baboi et al. Beam position monitor calibration at the flash linac at desy. In *Proceedings of PAC 2007*, number FRPMN017, page 3937, Albuquerque (USA), 2007.

[112] K. Honkavaara et al. Design of otr beam profilemonitors for the tesla test facility. In *Proceedings of PAC 2003*, number WPPB028, page 2467, Portland (USA), 2003.

[113] R. Tarkeshian et al. Femtosecond resolved determination of electron beam and xuv seed pulse temporal overlap in sflash. In *Proceedings of PAC 2011*, number WEOCN6, page 1452, New York (USA), 2011.

[114] G. Angelova et al. Observation of two-dimensional longitudinal-transverse correlations in an electron beam by laser-electron interactions. *Phys. Rev. ST AB*, 11:070702, 2008.

[115] A. Azima et al. Tolerance studies on the high harmonic laser seeding at flash. In *Proceedings of FEL 2008*, number TUPPH003, page 235, Gyeongju (Korea), 2008.

[116] L. H. Yu et al. Generation of intense uv radiation by subharmonically seeded single-pass free-electron lasers. *Phys. Rev. A*, 44:5178–5193, 1991.

[117] G. Stupakov et al. Using the beam-echo effect for generation of short-wavelength radiation. *Phys. Rev. Lett.*, 102:074801, 2009.

[118] D. Xiang et al. Demonstration of the echo-enabled harmonic generation technique for short-wavelength seeded free electron lasers. *Phys. Rev. Lett.*, 105:114801, 2010.

[119] B. Steeg, L. Juha, J. Feldhaus, S. Jacobi, R. Sobierajski, C. Michaelsen, A. Andrejczuk, and J. Krzywinski. Total reflection amorphous carbon mirrors for vacuum ultraviolet free electron lasers. *Appl. Phys. Lett.*, 84:657–659, 2004.

[120] T. Kita, T. Harada, N. Nakano, and H. Kuroda. Mechanically ruled aberration-corrected concave gratings for a flat field grazing incidence spetrograph. *Appl. Optics*, 22:512–513, 1983.

[121] N. Nakano, H. Kuroda, T. Kita, and T. Harada. Development of a flat-field grazing-incidence xuv spectrometer and its application in picosec. xuv spectroscopy. *Appl. Optics*, 23:2386–2392, 1984.

[122] M. Xie. Exact and variational solutions of 3d eigenmodes in high gain fels. *Nucl. Instrum. Meth. Phys. Res. A*, 445:59–66, 2000.

[123] Z. Huang and K.-J. Kim. Solution to the initial value problem for a high-gain fel via van kampen's method. *Nucl. Instrum. Meth. Phys. Res. A*, 475:59, 2001.

[124] C. Y. Teisset, N. Ishii, T. Fuji, T. Metzger, S. Köhler, R. Holzwarth, A. Baltuska, A. M. Zheltikov, and F. Krausz. Soliton-based pumpseed synchronization for few-cycle opcpa. *Optics Express*, 13:6550–6557, 2005.

[125] S. Hädrich, J. Rothhardt, F. Röser, T. Gottschall, J. Limpert, and A. Tünnermann. Degenerate optical parametric amplifier delivering sub 30 fs pulses with 2 gw peak power. *Optics Express*, 16:19812, 2008.

[126] J. Rothhardt, S. Hädrich, F. Röser, J. Limpert, and A. Tünnermann. 500 mw peak power degenerated optical parametric amplifier delivering 52 fs pulses at 97 khz repetition rate. *Optics Express*, 16:8981–8988, 2008.

[127] F. Röser, T. Eidam, J. Rothhardt, O. Schmidt, D. N. Schimpf, J. Limpert, and A. Tünnermann. Millijoule pulse energy high repetition rate femtosecond fiber chirped-pulse amplification system. *Optics Letters*, 32:3495–3497, 2007.

[128] A. A. Kaminski. *Laser Crystals, Their Physics and Properties*. Springer Verlag, 2 edition, 1990.

[129] P. Rußbueldt, T. Mans, G. Rotarius, J. Weitenberg, H.D. Hoffmann, and R. Poprawe. 400 w yb:yag innoslab fs-amplifier. *Optics Express*, 17:12230, 2009.

[130] P. Russbueldt, T. Mans, J. Weitenberg, H. D. Hoffmann, and R. Poprawe. Compact diode-pumped 1.1 kw yb:yag innoslab femtosecond amplifier. *Optics Letters*, 35:4169, 2010.

[131] E. Innerhofer et al. 60 w average power in 810 fs pulses from a thin-disk yb:yag laser. *Optics Letters*, 28:367–369, 2003.

[132] J. Neuhaus, J. Kleinbauer, A. Killi, S. Weiler, D. H. Sutter, and T. Dekorsy. Passively mode-locked yb:yag thin-disk laser with pulse energies exceeding 13 μj by use of an active multipass geometry. *Optics Letters*, 33:726, 2008.

[133] J. Speiser. Scaling of thin-disk lasers: influence of amplified spontaneous emission. *J. Opt. Soc. Am. B*, 26:26–35, 2009.

[134] T. Binhammer, E. Rittweger, R. Ell, F. X. Kärtner, and U. Morgner. Prism-based pulse shaper for octave spanning spectra. *IEEE J. Sel. To. Quantum Electr.*, 41:1552–1557, 2005.

[135] Gunnar Arisholm, Rüdiger Paschotta, and Thomas Südmeyer. Limits to the power scalability of high-gain optical parametric amplifiers. *J. Opt. Soc. Am. B*, 21:578–590, 2004.

[136] T. R. Schibli, J. Kim, O. Kuzucu, J. T. Gopinath, S. N. Tandon, G. S. Petrich, L. A. Kolodziejski, J. G. Fujimoto, E. P. Ippen, and F. X. Kaertner. Attosecond active synchronization of passively mode-locked lasers by balanced cross correlation. *Optics Letters*, 28:947, 2003.

[137] S. Witte, R. T. Zinkstok, W. Hogervorst, and K. S. E. Eikema. Numerical simulations for performance optimization of a few-cycle tera-watt nopcpa system. *Appl. Phys. B*, 87:677–684, 2007.

[138] C. Iaconis, V. Wong, and I. A. Walmsley. Direct interferometric techniques for characterizing ultrashort optical pulses. *IEEE J. Sel. Top. Quantum Electron.*, 4:285–294, 1998.

[139] C. Iaconis and I. A. Walmsley. Spectral phase interferometry for direct electric-field reconstruction of ultrashort optical pulses. *Optics Letters*, 23:792–794, 1998.

[140] S. Hädrich, S. Demmler, J. Rothhardt, C. Jocher, J. Limpert, and Andreas Tünnermann. High-repetition-rate sub-5-fs pulses with 12 gw peak power from fiber-amplifier-pumped optical parametric chirped-pulse amplification. *Optics Letters*, 36:313–315, 2011.

[141] C. Erny et al. Metrology of high-order harmonics for free-electron laser seeding. *New J. Phys.*, 13:073035, 2011.

[142] G. Lambert et al. An optimized khz two-colour high harmonic source for seeding free-electron lasers and plasma-based soft x-ray lasers. *New J. Phys.*, 11:083033, 2009.

[143] I. Kim, C. M. Kim, H.T. Kim, G. H. Lee, Y.S. Lee, J.Y. Park, D. J. Cho, and C. H. Nam. Highly efficient high-harmonic generation in an orthogonally polarized two-color laser field. *Phys. Rev. Lett.*, 94:243901, 2005.

[144] C.-J. Lai, K.-H. Hong, V.-M. Gkortsas, S.-W. Huang, L.-J. Chen, and F. X. Kärtner. Scaling of high-order harmonic efficiencies with visible wavelength drivers: A route to efficient extreme ultraviolet sources. *Appl. Phys. Lett.*, 97:061107, 2010.

[145] M. Geissler, G. Tempea, and T. Brabec. Phase-matched high-order harmonic generation in the nonadiabatic limit. *Phys. Rev. A*, 62:033817, 2000.

[146] V. Tosa, V. S. Yakovlev, and F. Krausz. Generation of tunable isolated attosecond pulses in multi-jet systems. *New J. Phys.*, 10:025016, 2008.

[147] R. Benattar, C. Popovics, and R. Sigel. Polarized light interferometer for laser fusion studies. *Rev. Scien. Instr.*, 50:12, 1979.

[148] T. Ditmire and R.A. Smith. Short-pulse laser interferometric measurement of absolute gas densities from a cooled gas jet. *Optics Letters*, 23:618–620, 1998.

[149] Q.-Z. Yu, Y.-T. Li, J. Zhang, J. Zheng, H.-M. Li, X.-Y. Peng, and K. Li. Characterization of density profile of cylindrical pulsed gas jets. *Chin. Phys. Lett.*, 21:874–876, 2004.

[150] M.Hipp, J.Woisetschlaeger, P.Reiterer, and T.Neger. Digital evaluation of interferograms. *Measurement*, 36:53–66, 2004.

[151] J.-H. Kim and Ch.H. Nam. Plasma-induced frequency chirp of intense femtosecond lasers and its role in shaping high-order harmonic spectral lines. *Phys. Rev. A*, 65:033801, 2002.

[152] M. Yu. Ivanov, T. Brabec, and N. Burnett. Coulomb corrections and polarization effects in high field high harmonic emission. *Phys. Rev. A*, 54:742–745, 1996.

[153] N. Milosevic, A. Scrinzi, and T. Brabec. Numerical characterization of high harmonic attosecond pulses. *Phys. Rev. Lett.*, 88:093905, 2002.

[154] V. S. Yakovlev, M. Ivanov, and F. Krausz. Enhanced phase-matching for generation of soft x-ray harmonics and attosecond pulses in atomic gases. *Optics Express*, 15:15351, 2007.

[155] G. Cerullo et al. Nonadiabatic three-dimensional model of high-order harmonic generation in the few-optical-cycle regime. *Phys. Rev. A*, 61:063801, 2000.

[156] Philippe Balcou, Pascal Salières, Anne L'Huillier, and Maciej Lewenstein. Generalized phase-matching conditions for high harmonics: The role of field-gradient forces. *Phys. Rev. A*, 55:3204–3210, 1997.

[157] E. Constant, D. Garzella, P. Breger, E. Mevel, Ch. Dorrer, C. Le Blanc, F. Salin, and P. Agostini. Optimizing high harmonic generation in absorbing gases: Model and experiment. *Phys. Rev. Lett.*, 82:1668–1671, 1999.

[158] J.-F. Hergott, M. Kovacev, H. Merdji, C. Hubert, Y. Mairesse, E. Jean, P. Breger, P. Agostini, B. Carré, , and P. Salières. Extreme-ultraviolet high-order harmonic pulses in the microjoule range. *Phys. Rev. A*, 66:021801(R), 2002.

Acknowledgment

I would like to thank Prof. Dr. Jörg Rossbach for the opportunity to participate in a high impact research field. Even though the topic was slightly beyond the usual research focus within the university group, he supported my ideas and work whenever necessary. I would like to thank also my second referee, Prof. Dr. Markus Drescher, for his readiness to review my thesis. I highly appreciate the review by my third referee Prof. Dr. Jens Biegert from the Institute of Photonic Sciences in Barcelona. In addition, many thanks to Dr. Jens Osterhoff for being my second referee at my PhD defense.
Dr. Franz Tavella was the driving force during my PhD and I am grateful for his patience at the beginning and his team spirit during the whole time. His knowledge, his energetic motivation and his high demands were the basis for a successful work, which resulted in several high quality publications. It was a pleasure to discuss and realize new ideas with him. Despite a lot of work on his desk, his door was always open and questions were welcome at any time.
Of course, no such work can be realized without an awesome team. I would like to thank Dr. Mark Pandolini for his perfect review of my English in my thesis. I am grateful for the wonderful team work with Robert Riedel and Michael Schulz. Many thanks also to my diploma student Arvid Hage, who did his work in a very professional and altruistic way. Thanks to Dr. Juliane Rönsch-Schulenburg and Dr. Velizar Miltchev for helpful discussions.
At DESY there are two people who made all crazy ideas possible concerning the technical realization: Josef Gonschior and Otto Peters. With their high motivation and amazing knowledge in engineering they created wonderful setups for our experiments. I could easily fill two pages of acknowledgement only for these two guys.
The team spirit was not limited to our small group. Our fantastic collaboration with Queens University Belfast made it possible to discuss problems with experts in HHG like Dr. Brendan Dromey and Prof. Dr. Matthew Zepf. Special thanks to Mark Yeung for the fun times on Crete. I would like to thank also my colleagues from TEI Crete for being such nice hosts. In addition, I would like to thank Dr. Jan Rothhardt and Steffen Hädrich from IAP Jena for their team mentality during our measurements with the prototype OPCPA system.
I really appreciate the professionalism of the DESY and University workshops. Of course, I would like to thank Dr. Bart Faatz, project leader of FLASH II, who gave me the possibility to do research within the great project.

Finally, I would like to thank my dear girlfriend, Gun Röttgers, for her patience and support especially during the last months of my PhD. She was able to turn bad moments into good ones and she sometimes simply forced me to take a break. Many thanks to my parents, Irmgard Willner and Ulrich Schäler for their interest in my work and their unconditioned support. Thanks to Roland and Kerstin Willner and all my close friends for an equalized life-work balance.